der Bundeswehr
Universität München

Autonomous LiDAR-free Navigation and AI-assisted Landing on Small Celestial Bodies

M.Sc. Edoardo Caroselli

Vollständiger Abdruck der von der Fakultät für Luft- und Raumfahrttechnik der Universität der Bundeswehr München zur Erlangung des akademischen Grades eines

Doktor-Ingenieurs (Dr.-Ing.)

angenommenen Dissertation.

Gutachter/Gutachterin:

1. : Prof. Dr.-Ing. Roger Förstner
2. : Prof. Dr.-Ing. Fabio Curti

Diese Dissertation wurde am 29.01.2024 bei der Universität der Bundeswehr München eingereicht und durch die Fakultät für Luft- und Raumfahrttechnik am 24.05.2024 angenommen. Die mündliche Prüfung fand am 09.07.2024 statt.

A Priscilla, Paola, Alessandro e Giulia che mi accompagnate in questo Viaggio.

La strada si scopre soltanto percorrendola.
Guai a rimanere bloccati di fronte ad un crocicchio di vie
e non decidersi mai a tentarne una.
La rivelazione della strada avviene lungo la strada.
Non prima.
La strada giusta la si scopre soltanto dopo che si è deciso,
coraggiosamente, di uscire all'aperto
e di partire in esplorazione.
Certo si corrono dei rischi.
Ma il rischio maggiore è quello di non correre rischi.
E quando avremo percorso un bel tratto
ci volteremo indietro,
ma solo per un attimo: per valutare il tragitto,
gli ostacoli superati, le cadute, le forze rimaste...
Scopriremo di avere un panorama di fronte a noi,
ma ci accorgeremo che solo proseguendo il cammino
potremo giungere alla meta
ancora nascosta ai nostri occhi.
A. Lowen.

Kurzfassung

Die Erforschung kleiner Körper in unserem Sonnensystem, wie Asteroiden und Kometen, ist zu einem wichtigen Schwerpunkt in den Planetenwissenschaften geworden, da sie Aufschluss über die Entstehung des Sonnensystems und die Möglichkeiten der Ressourcennutzung geben können und die Notwendigkeit besteht, die Risiken für die Planetenverteidigung zu bewerten und zu mindern. In-situ-Explorations- und Probenrückführungsmissionen zu diesen kleinen Körpern liefern wertvolle Informationen über deren physikalische und chemische Eigenschaften, Zusammensetzung und Umweltbedingungen. Autonomie ist von entscheidender Bedeutung, wenn es darum geht, die Grenzen von Missionen zu kleinen Sonnensystemkörpern (SSSB) zu erweitern, indem Raumfahrzeuge in die Lage versetzt werden, Aufgaben auszuführen und eigenständig Entscheidungen zu treffen.
Diese Arbeit zielt darauf ab, einen Beitrag zur Weiterentwicklung der Autonomie bei SSSB-Missionen zu leisten, wobei der Schwerpunkt auf der präzisen Landung von Mikro-Raumfahrzeugen liegt.
Die Forschung untersucht kritische Aspekte der autonomen Navigation und konzentriert sich dabei auf die Wahrnehmung der Umgebung und die Entscheidungsfindung. LiDAR-freie visuelle Navigation und KI-gestützte Landetechniken werden für die Fern- und Nahbereichsnavigation untersucht. Die Dissertation enthält die folgenden Hauptbeiträge:
Erstens wird ein autonomes visuelles relatives Navigationssystem entworfen, implementiert und getestet. Dieses System ermöglicht die Navigation von Raumfahrzeugen in Oberflächennähe durch relative Messungen. Es verwendet einen neuartigen monokularen, simultanen Lokalisierungs- und Kartierungsfilter (SLAM), der durch Höhenmessungen unterstützt wird und eine punktgenaue Landung am Ziellandeplatz ermöglicht.
Zweitens wird eine KI-gestützte autonome Technologie zur Auswahl eines sicheren Landeplatzes entwickelt, implementiert und getestet. Diese Technologie vereint Bildverarbeitungs- und maschinelle Lernmethoden, erfordert minimale Benutzereingaben und bezieht die Landeanforderungen direkt in den Algorithmus ein. Für die Validierung werden authentische Missionsbilder verwendet.
Diese Forschungsarbeit bietet Einblicke in die Herausforderungen und Möglichkeiten bei der Verwirklichung von Autonomie in SSSB-Missionen. Die Arbeit schließt mit einer Zusammenfassung der wichtigsten Beiträge, der Diskussion von Einschränkungen und Vorschlägen für zukünftige Forschungsrichtungen, um die Navigationsfähigkeiten von Raumfahrzeugen bei der Erforschung kleiner Körper in unserem Sonnensystem weiter zu verbessern.

Abstract

Exploring small bodies in our solar system, such as asteroids and comets, has become a significant focus in planetary sciences due to their potential insights into the Solar System's formation, resource utilization prospects, and the need to assess and mitigate planetary defense risks. In situ exploration and sample return missions to these small bodies provide valuable information about their physical and chemical properties, composition, and environmental conditions. Autonomy is crucial in advancing the boundaries of small solar system body (SSSB) missions, enabling spacecraft to perform tasks and make decisions independently.

This thesis aims to contribute to the advancement of autonomy in SSSB missions, focusing on the precise landing of micro-spacecraft. The research investigates critical aspects of autonomous navigation, focusing on environment perception and decision-making. LiDAR-free vision-based navigation and AI-assisted landing techniques are explored for far-range and close-range navigation. The thesis presents the following main contributions:

Firstly, an autonomous vision-based relative navigation system is designed, implemented, and tested. This system allows spacecraft to navigate in the proximity of the surface using relative measurements. It employs a novel monocular simultaneous localization and mapping (SLAM)-based filter assisted by altimeter measurements, enabling pinpoint landing at the target landing site.

Secondly, an AI-assisted autonomous safe landing site selection technology is designed, implemented, and tested. This technology fuses image processing and machine learning methods, requiring minimal user input and incorporating landing requirements directly into the algorithm. Authentic mission images are used for validation.

This research provides insights into the challenges and opportunities in achieving autonomy in SSSB missions. The thesis concludes by summarizing the main contributions, discussing limitations, and suggesting future research directions to further enhance spacecraft navigation capabilities in exploring small bodies in our solar system.

Keywords: Autonomy, Autonomous Navigation, Asteroid Landing, Microlander, Machine Learning, Hazard Detection, Vision-based Navigation, AI-based Safe Landing Site Assessment, GNC, Space Exploration.

Contents

List of Figures

List of Tables

Nomenclature

List of Acronyms

AI Artificial Intelligence

AOCS Attitude and Orbital Control System

CNN Convolutional Neural Network

CoM Centre of Mass

DoF Degree of Freedom

DSN Deep Space Network

EKF Extended Kalman Filter

ESA European Space Agency

FCN Fully Connected Network

FOV Field of View

FPGA Field Programmable Gate Array

GNC Guidance, Navigation and Control

HAP High Altitude Phase

HAPNAV High Altitude Phase Navigation

HDA Hazard Detection and Avoidance

IMU Inertial Measurement Unit

IP Image Processing

IR Infrared

ISL Inter-Satellite Link

JPL Jet Propulsion Laboratory

KAZE Japanese for "wind"

KLT Kanade Lucas Tomasi Tracker

LAP Low Altitude Phase

LAPNAV Low Altitude Phase Navigation

LFR Low Frequency Radar

LiDAR Light Detection and Ranging

LOS Line of Sight

LRF Laser Range Finder

LUT Look Up Table

ML Machine Learning

MOI Moment of Inertia

NEO Near Earth Orbit

NEO-MAPP Near Earth Orbit Modelling and Payloads for Protection

PANGU Planet and Asteroid Natural Scene Generation Utility

RCS Reaction Control System

RW Reaction Wheel

SLAM Simulataneous Localization and Mapping

SLSS Safe Landing Site Selection

SRP Solar Radiation Pressure

SSSB Small Solar System Body

STR Star Tracker

TAG Touch And Go

VBN Vision-based Navigation

List of Symbols

General

ϕ	Sun phase angle[rad]
c	Speed of light[m/s]
h_{cam}	Pixel angular size[rad/px]
h_{px}	Pixel metric width[m/px]
l	Length [m]
R	Mean radius of asteroid[m]

r Generic spacecraft position norm in asteroid-fixed reference frame[m]

Navigation

$\boldsymbol{\epsilon}_{cob}$ Lightning conditions correction factor[pixel]

$\hat{\mathbf{p}}_{cof}$ Estimated center of figure pixel coordinates[pixel]

ρ Density

ρ Assumed surface reflectivity[$-$]

$\mathbf{p}_{cob}$ Centre of brightness pixel coordinates[pixel]

$\mathbf{u}_{det}$ Unit vector of Sun direction in camera sensor plane[m]

$A_{\perp}$ Surface area of the spacecraft project in the Sun direction[m^2]

E Intensity of solar radiation[W/m^2]

p_0 Solar radiation pressure at 1 AU[N/m^2]

$r_{\otimes}$ Mean radius of Earth's orbit[km]

Other Symbols

k_{∞} Infinity constant

Chapter 1

Introduction

This chapter serves as the introduction, setting the stage for the research by highlighting the background and motivation behind the study. It outlines the challenges faced by Small Solar System Bodies' missions and identifies the need for innovative autonomy solutions. The objectives and scope of the thesis are clearly defined to give the reader a clear understanding of what will be covered.

1.1 The Small Bodies Frontiers

The in situ exploration of Small Solar System Body, mostly asteroids and comets, is currently at the forefront of planetary sciences. These bodies provide a window into the past of the Solar System [11]. Asteroids, in particular, are remnant debris from planetary formation. They contain, at various stages, the history of the birth of the Solar System. They can provide details of the core formation process or the composition of the protoplanetary disk [12, 13]. Moreover, they can also provide mechanisms for the formation of inner planets. Motivation for the exploration of Small Solar System Body (SSSB) is well-grounded and strong; it has encouraged a large portion of the planetary science community over the last years [14]. The main mission drivers are the following top-level scientific objectives:

1. **Science Research**: The asteroids are key science targets, thought to be pristine objects of the early formation of the Solar System. Significantly, organic molecules surveyed on the surface could profoundly impact our understanding of the origin of life [15, 16].

2. **Future resource**: As resources on Earth become increasingly scarce, asteroids could represent a strong potential for minerals and precious metals mining. They are the closest substantial resources due to the Solar System's formation, and the critical experience gained with the next asteroid missions will represent a necessary improvement for mapping and analyzing these unknown environments for resource exploitation [17, 18].

3. **Planetary Defence**: The risk assessment for the impact of asteroids has been considered for almost two decades. Small bodies are continually colliding with Earth, and although the chances of a significant asteroid impact are low in the near future, a constant evaluation of the risk is necessary. Many planetary defense strategies have been developed, such as a kinetic impactor to alter the target trajectory, and asteroids are the focus of the research on the latter strategies [19–21].

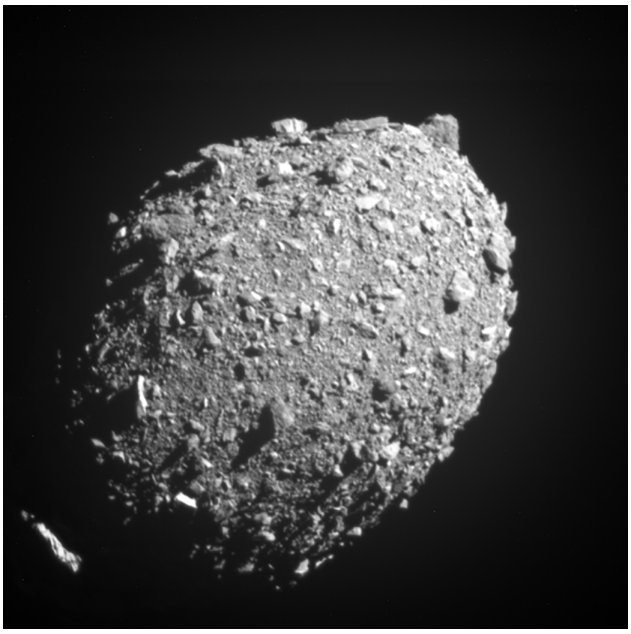

Figure 1.1: DART's last complete image of the Dimorphos asteroid before impact. (NASA/APL)

1.1.1 Landing on SSSB

In situ studying and sample return missions allow for characterizing the environment, investigating the surface's physical and chemical properties, and understanding the composition and aggregation of the target body. Spacecraft missions to the asteroids are the only solution to get in situ measurements, and there are several ways to achieve these measurements.

One of the first mission strategies is to fly by the body to gather precious information [22] and collect particles around it [23]. The orbiting missions allow more time around the asteroid and, consequently, a more extensive survey of the unknown environment. The Touch And Go (TAG) approach only temporarily touches the surface [24], and the sample is obtained via a horn-like fast mechanism. The mission concept is less complex than a traditional landing, and currently, no landing has been attempted for large spacecraft. Landing has been accomplished only for smaller spacecraft (CubeSat or microprobes [25]) to mitigate the risk of losing the mothership without excessively altering the mission returns of surface measurements. These methods will be thoroughly described in Section 2.2.4 and applied in several missions, which will be discussed in Section 1.2.1.

1.1.2 Autonomy: Key Enabling Technology for Precise Landing

Autonomy represents the leading research driver for this research as it has been identified as the primary key enabling technology for future explorations [26–28]; in this section, the research is motivated by stating the clear need for autonomous systems and deriving the principal key-enabling technologies for autonomous precise landing.

Autonomy as a future mission enabler. Advancements in exploring celestial bodies are focused on achieving autonomy in mission operations. Autonomy pertains to a spacecraft's capability to perform tasks and make decisions independently, without requiring constant human intervention [29]. The development of autonomy plays a crucial role in enabling spacecraft to navigate, land,

and conduct scientific investigations on SSSBs, as evident in past and current missions [30].

Why more autonomy is needed? Advancing the boundaries of autonomy in upcoming missions is crucial as we are reaching the limit of human intervention or ground in the loop for SSSB missions. The need for autonomy becomes paramount to ensure higher performance, mainly when operating at large distances where communication delays pose significant challenges. As missions become more complex, either due to an increase in the number of probes or the exploration of multiple targets, the importance of autonomy is further underscored [31]. Scenarios, where multiple spacecraft can independently land and explore asteroid fields with minimal human intervention, are envisioned.

To meet these demands, further development of the mentioned technologies is imperative [32]. This includes advancing more sophisticated machine learning algorithms enabling spacecraft to learn and adapt in real-time, improving their decision-making capabilities. Improved sensor capabilities are also vital, allowing spacecraft to gather accurate and reliable data to inform their autonomous operations. This encompasses advancements in optical, infrared, and Light Detection and Ranging (LiDAR) sensors and integrating new sensing technologies.

Distant flight time. The main asteroid belt lies around 2.5 AU, between Mars and Jupiter, and it holds small solar system bodies of different compositions [33]. Therefore, this is next to Near-Earth Asteroids, a very relevant site to find a scientifically interesting asteroid for close proximity operations. Communication time at that distance would take approximately 25 minutes. The ground station can command the spacecraft remotely; however, the time delay implies a high risk for close-range operations. In addition, in case of unforeseen circumstances, the spacecraft is compromised without autonomy, and the time delay for active control could endanger the safety of the mission. Autonomy is principal as a consequence of long signal flight time.

One potential solution is to execute a gradual descent, ensuring a crash-free trajectory despite the presence of Earth-in-the-loop navigation, albeit at the expense of increased fuel consumption. Another approach involves leveraging autonomous navigation techniques based on the data acquired during the mission's characterization phase. By eliminating Earth's involvement from the observation-state estimation, guidance decision-making, and actuator command loop, autonomous navigation permits significantly closer operations while ensuring the spacecraft's safety. This autonomous approach has proven to be the preferred method in previous asteroid missions.

Decrease time-to-surface. Typically, prior to the landing phase, a prolonged surveying and characterization period is requisite, during which the target is meticulously examined, facilitating the acquisition of a comprehensive map. The characterization phase is a protracted process that consumes substantial time and fuel resources. In situations where an asteroid mission involves a mothership and smaller spacecraft, it is conceivable that the smaller spacecraft may possess a more limited array of sensors. Consequently, there exists a need to expedite the mission timeline and accommodate cost-effective and compact spacecraft by cultivating alternative autonomous methodologies.

Nevertheless, for the purpose of maximizing mission duration and mission yield, it is imperative for the spacecraft to promptly land subsequent to the rendezvous with the asteroid, allowing for expeditious transfer of the payload to the surface for direct interaction.

Consequently, some strategies can be identified to enhance initial operation phases. Firstly, local mapping could be enough for relative navigation and to allow a safe landing. If the Guidance, Navigation and Control (GNC) algorithms are capable of adapting to an unknown environment, little a priori information is needed from the orbiter or ground.

Robustness and adaptivity Additionally, robust decision-making and adaptive autonomy are crucial for navigating the challenges posed by SSSB missions. These aspects involve developing algorithms and strategies to handle unexpected events, adapt to changing environments, and make intelligent decisions in complex and uncertain situations. By incorporating robustness and adaptability into the autonomy framework, spacecraft can better handle mission complexities and ensure the success of their operations.

Robust design is a high priority due to the unknown environment in which the spacecraft navigates. The main sources of uncertainties are:

- Gravity field: as a consequence of the diverging spherical harmonics approximation, new representations techniques need to be analyzed (Mascons, Polyhedron). Especially during proximity operations, the gravity field is strongly perturbed, and the GNC systems should compensate for unexpected environmental forces. The gravity fields of SSSB are highly perturbed and non-central due to their irregular shape or differentiated composition, and they are relatively weak. As a result, stable closed orbits could turn into crashing or escape orbits in days [34]. They are significantly subject to perturbations by nearby object approaches and Solar Radiation Pressure (SRP), which may increase even more the irregularities in the gravity field due to mass distribution. Also, several asteroids are subject to fast rotation periods; as a consequence, the difference between gravity acceleration and effective gravity (i.e., taking into account apparent forces) is large. As a target for a mission, they have the most perturbed environment, and hence the dynamics around them can be unpredictable.

- Surface: terrain information is not always accurate, and the lander should be able to cope with various conditions. Hazard Detection and Avoidance (HDA) functionalities combined with the assessment of the landing site allow a reduction in the landing footprint; the latter greatly enhances the robustness and science return of the mission [35]. Safer operations are run as a consequence of real-time assessment of the hazards. Moreover, the scientific return is increased by selecting a more interesting landing site due to the increased on-site surface knowledge. Only local mapping could be required for proximity operations, and the target body's global characterization could be less detailed.

- Long flight time: degradation is another central point linked to robustness; in fact, failure of units after long flight duration could lead to the definition of flexible strategies for GNC or algorithms which require few and diverse information (e.g., camera and LiDAR or only camera or LiDAR according to the availability). Flexible algorithms also allow the application to different missions, from large-size landers to small CubeSat and vice versa, independently from avionics.

Perception and decision-making The assessment of previous missions (as in Section 1.2.1) reveals the utilization of various key enabling technologies for autonomy. Autonomous environment

perception (e.g., vision-based navigation) has played a crucial role, allowing spacecraft to determine their position and orientation relative to the target body using visual information. Additionally, *decision-making* autonomous systems incorporating machine learning and image processing (Image Processing (IP)) have been employed for hazard detection, slope estimation, and safe landing site selection [36].

Partial progress towards autonomous systems. This has been achieved by optical relative navigation and radiometric absolute navigation. Radiometric tracking enables precise absolute tracking of the spacecraft trajectory with respect to Earth [37]. Landmark-based navigation has utilized identifiable features on the SSSB's surface to aid in spacecraft localization and orientation. Although these technologies led to successful missions, they rely on continuous human monitoring and processing. The landmark-based navigation requires extensive modeling effort on the ground, radiometric measurements are not always available, and the landing site is carefully chosen by extensive surface mapping. In contrast, a fully autonomous spacecraft would land on the surface and afterward explore the whole surface independently. By extending the exploration range in this way, the overall scientific return of the mission would increase significantly.

Leverage computing advancements. In the last decades, computing power has largely increased, resulting in a paradigm shift towards computational real-time GNC, with limited human-in-the-loop [38]. To address the limitation of human-in-the-loop, more recent missions progressively included technologies that pushed the autonomy frontier even further. Hayabusa-2 [39], showcased upgraded navigation instruments and extensive characterization techniques, including radiometric tracking and autonomous descent. OSIRIS-REx [40], employed, in addition to radiometric tracking, vision-based navigation for close-range operations, advanced exposure techniques, and landmark tracking. Finally, DART [21], achieved kinetic impact deflection with the help of fully autonomous navigation systems and avionics.

Tooling artificial intelligence. Moreover, image processing is shifting towards a machine learning-oriented approach [41]. Even if the space sector is considered conservative, major technological steps have been made toward Artificial Intelligence (AI) and Deep Learning [42]. With the rise of the practical usability of architectures such as support vector machines or artificial neural networks, machine learning and AI have become ever more attractive and now provide practical solutions for a wide range of problems. AI has achieved impressive results over the past few years, but often the learned solution is difficult to understand and examine by humans. Additionally, the robustness and reproducibility of AI results are usually evaluated by statistical testing, and there is no systematic method to guarantee that a solution synthesized using AI techniques meets the expectations of the designer. This becomes a pressing issue when applying AI methods to safety-critical tasks such as GNC, where expectations are rigid verification requirements.

1.2 State-of-the-Art

The first asteroid flyby was in 1991 by the spacecraft Galileo across the asteroids Gaspra and Ida on its way to Jupiter. Since then, there have been several missions, which have been dedicated

to not just flybys, but landing on and studying asteroids [22, 43]. There has been an increased interest in them in recent years due to the objectives discussed in Section 1.1.2. Only orbiters and landers are presented; in particular, no flyby missions are included to focus on close proximity operations, descent, and landing architectures. In Table 1.1, the missions are resumed, and their GNC architecture is briefly described.

Name	Mission Type	Target Diameter [km]	GNC Suite	Mass [kg]
NEAR (NASA)	Orbiter landed on Eros	16.8	4x 21N hydrazine thrusters 7x 3.5 N hydrazine thrusters 4x Reaction Wheel (RW)s 5x Sun Sensors 1x Star Tracker (STR) 1x Inertial Measurement Unit (IMU)	800
Hayabusa (JAXA)	Sample return TAG on Itokawa	0.3	12x 20 N Reaction Control System (RCS) 3x RW 1x Sun Sensor 1x STR 2x IMU 1x Accelerometer 1x Narrow Angle Camera 1x Wide Camera 1x LiDAR 1x Laser Range Finder (LRF)	510
Rosetta (European Space Agency (ESA))	Comet orbiter with lander on 67P	4	(Phylae) 1x Upward Facing Thruster 1x Flywheel (Phylae)	100
Dawn (NASA)	Orbiter around Vesta and Ceres	525-546	12x 0.9 N hydrazine thrusters 4x RWs 16x Sun Sensors 2x STR 3x IMU (spinning gyros) 2x Cameras	1217

Name	Mission Type	Target Diameter [km]	GNC Suite	Mass [kg]
Hayabusa-2 (JAxA)	Sample return TAG on Ryugu	1.1	12x 20 N Hydrazine Thrusters 4x RWs 4x Sun Sensors 2x STR 2x IMU 4x Accelerometers 3x Cameras 1x LiDAR 1x LRF	9.6 (Mascot)
OSIRIS-Rex (NASA)	Sample return TAG on Bennu	0.525	28x RCS 4x RWs Sun Sensors 2x STR 2x IMUs 1x Camera suite 1x LiDAR 1x Laser Altimeter	2110
DART (NASA)	Impactor on Dimorphos	0.75-0.16	5x sun sensors STR Camera	500
Hera (ESA)	Probes on Didymos and Dimorphos	0.75-0.16	RCS 4x RWs 12x Sun Sensors 2x STR 2x IMU 2x Cameras 1x Altimeter	870
NEA-Scout (NASA)	Technology demonstrator on Apollo NEA	0.1	N/A	14
Psyche (NASA)	Orbiter around Psyche	225	N/A	2608
Janus (NASA)	Orbiter on binary asteroids	1.6-0.4	N/A	38
MMX (JAXA)	Sample return lander on Phobos	27	N/A	150

Table 1.1: Asteroid Mission Summary

1.2.1 Past and Current Missions

NEAR Shoemaker

On February 12, 2001, NEAR-Shoemaker was the first spacecraft to land on the surface of Eros. It was not designed for landing, but after 5 open loop maneuvers, it succeeded in touching down. The NEAR navigation team used optical navigation during the terminal approach; the main challenges were to estimate the center of mass given the irregularly shaped body and high surface brightness, which made it impossible to expose correctly both stars and asteroids.

The goal of the mission was to increase the knowledge of asteroids in general by returning data to Earth. NEAR started orbiting its target asteroid (433) Eros in February 2000. An image of the asteroid is shown in Figure 1.2 NASA's Deep Space Network (DSN) was used to perform radiometric tracking of the spacecraft to navigate it towards Eros. Cameras were used to create a database of landmarks, after which these landmarks were tracked for navigation purposes, as well as rotational state estimation, shape, mass, and gravity estimation. The landmark tracking and matching were done by hand by operators on Earth. A LRF was also used to get altitude measurements whenever the distance to the surface was in the hundreds of kilometers range. The LRF measurement was used in the orbit determination filter. The LRF was also used to solve for an accurate shape model, which was then used to obtain a-priori gravity estimates by assuming a constant density. The LRF was never used for real navigation purposes, but merely as a consistency check on the radiometric tracking and landmark-based navigation. By comparing the estimated gravity to the real gravity that the spacecraft experienced, it was concluded that the internal structure of the asteroid was mainly uniform.

The landing trajectory was dependent on the accurate characterization of Eros's dynamical and physical properties (i.e., mass, gravity distribution, spin, pole, shape). The characterization phase took approximately 2 years. They have used for the first time other gravity modeling techniques as a consequence of the diverging spherical harmonics representation. In addition, robustness was granted through Monte Carlo simulation of the open-loop trajectories, and constant ground coverage was available [44].

Figure 1.2: NEAR Over Eros' horizon. (NASA)

Hayabusa-1

Launched in 2003, Hayabusa represents the first asteroid sample return mission. The target chosen by JAXA is the asteroid Itokawa. Two touchdowns were accomplished following the touch-and-go procedure (see Section 2.2.4 for details); during the first one, the spacecraft collected some material from the asteroid's surface, and however the second attempt faced operational problems. The samples collected were successfully returned to Earth. The failures included two RWs failures and an accidental landing [45]. Hayabusa included a multi-band imaging camera to image the entire surface of the asteroid. It had an autonomous onboard guidance and navigation system to touch down on the target since the precise shape, size, and surface conditions of the asteroid were unknown. The onboard GNC system included a two axes Sun sensor, STR and an IMU for attitude determination, an accelerometer, and a reaction control system with thrusters and reaction wheels for attitude and translational control.

Navigation was carried out using narrow-angle and wide-angle cameras. The latter allowed mapping and regional safety monitoring of surface obstacles. High altitude and low altitude measurements were done by a LiDAR and a laser ranger, respectively. The Attitude and Orbital Control System (AOCS) used the inputs from the cameras, LiDAR, laser ranger, and an extended Kalman filter for state estimation. The programmed function included image processing designed to detect an artificial target marker location to approach and cancel the surface relative velocity [46].

One of the primary goals of the mission was to return a sample of the surface of the target asteroid (25143) Itokawa back to Earth. A hybrid navigation solution was employed that combines optical navigation with radiometric tracking [47]. Images were processed on the ground to calculate the direction vector from the spacecraft to the asteroid. A nonlinear least-squares estimator was used to obtain the spacecraft position and velocity in an inertial frame. In the final part of the descent, between 20 km and 3 km altitude, a more autonomous approach was envisioned. However, due to a hardware failure, the crew decided to fly the spacecraft by hand. The intention was to use the altitude measurement from the LiDAR together with the ' center address', which is calculated from images of the onboard navigation cameras. This center address is found by extracting groups of adjoining pixels whose brightness is beyond a specified threshold. The group that has the highest number of pixels is assumed to be the one representing the asteroid, after which the center of this group in the frame (pixel coordinates) is used in a Kalman filter to estimate three-dimensional relative position and velocity [48].

Noteworthy is the target marker approach that was used for the final descent. A bright object was released from the spacecraft and fell onto the surface of the asteroid. The navigation system then used this target marker as a point of reference in the frame.

The Minerva micro-lander experienced a deployment failure; it was supposed to test inter-satellite communication and hopping relocation via an internal flywheel.

Rosetta

Launched in 2004 to the Comet 67P/Churyumov-Gerasimenko, it orbited around it before sending the lander, Philae to its surface. After being in space for more than 12 years, Rosetta's mission concluded with it descending on the surface of the comet in September 2016 [49]. During the approach, from circa 44000 km to 122 km, radiometric and optical information were used as primary

Figure 1.3: Hayabusa-1 at Itokawa. (JAXA)

measurements for the navigation. Single image frames contain both the asteroid and the star field behind them, giving valuable information for the state estimation. After 3500 km, the star field was no longer useful because the centroiding errors were so large that they were more significant than any pointing error that could be deduced from the measurements.

Upon arrival, an early characterization phase was carried out, during which the rotational state, shape, landmarks identification, and a first estimate of the gravity field were determined [50]. Since then, and throughout the rest of the mission phases, Rosetta navigated using landmark observations which were obtained on-ground by processing NAVCAM images. As the mission progressed, automatic feature detection methods were phased in to track the landmarks. 3D high-resolution maps (maplets) of landmarks are created from these observations. Combined with an albedo map and photometric model, the visual appearance of the landmark can be predicted for every observation condition. Matching the landmarks to a library of known landmarks gives a measurement for the navigation filter.

Rosetta's GNC system included two pairs of coarse Sun sensors, two star trackers, three IMUs with three gyros and accelerometers each, and two navigation cameras (NAVCAM) for navigation and control two sets of twelve thrusters of 10 N each, a bi-propellant system, four-momentum wheels, 1-Degree of Freedom (DoF) solar array pointing mechanisms and a 2-DoF antenna pointing mechanism. The kinematical and dynamical state of the comet was unknown a prior, and hence in situ measurements were used to refine the knowledge of these properties. Relative navigation performance required the relative state to be measured, as a consequence of the low accuracy of the ground tracking [51].

OSIRIS-NAC and NAVCAMS provided optical images to detect the asteroid of interest and deduce the relative trajectory from Rosetta to the center of the asteroid of interest or a recognizable feature on its surface. For the comet, there were four observational phases to achieve navigation accuracy for the lander delivery phase. The lander body contained a flywheel for attitude stabilization during descent as well as cold gas hold-down thrusters to support touch-down. Anchoring harpoons are additional devices to stay on the surface. The lander descends ballistically toward

the selected landing site. Phylae landed on the surface but due to system failures, it bounced three times and reached a landing site far from the nominal one [52].

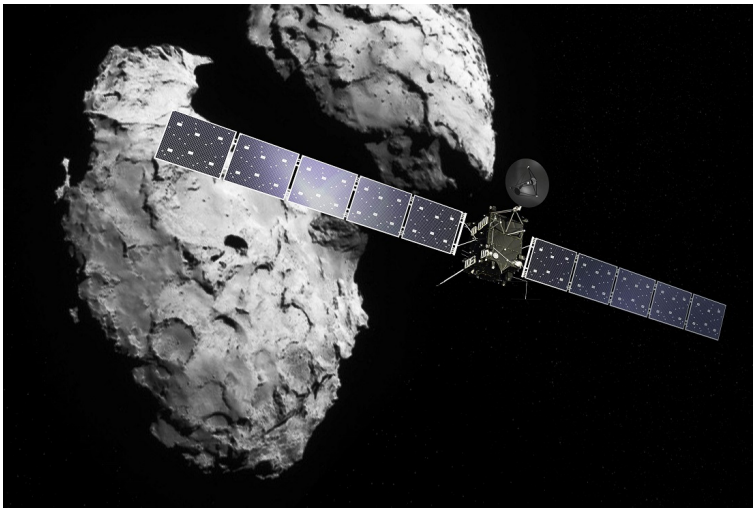

Figure 1.4: 67P/Churyumov–Gerasimenko and Rosetta spacecraft. (ESA/Rosetta/MPS)

Dawn

Launched in 2007, Dawn is a multi-target orbiter. It completed a 14 months survey mission of Vesta, one of the largest asteroid belt objects, and then it entered the orbit around Ceres, the largest object of the main asteroid belt. The GNC subsystem included two STR, three two-axis IMU, 16 sun sensors, four reaction wheel assemblies, and a set of 12 0.9 N hydrazine thrusters. The two scientific framing cameras were also used for navigation and target relative estimation as part of the ground processing. When in orbit around the asteroid, a combination of optical navigation and radiometric navigation was used. A topographic map is developed for navigation purposes with 10 m accuracy on the surface. The heritage of Dawn cameras is being implemented on the Hera mission [53].

Hayabusa-2

Hayabusa 2 is an extension of Hayabusa and was launched in December 2014 to the asteroid Ryugu. It surveyed the asteroid for a year and a half, and then it returned with samples in December 2020 [39]. The design of the GNC system of Hayabusa 2 is significantly similar to Hayabusa. The navigation instruments are just upgraded versions as those of Hayabusa: 4 RWs and RCS, navigation cameras, LiDAR, LRF, flashlight, and target marker. The main lesson learned from Hayabusa regarded an additional reaction wheel for redundancy and more secure propellant plumbing. An advanced solar sail mode is implemented to save fuel during longer mission phases [54].

For the navigation, an extensive characterization phase is carried out. In this phase, the axis of rotation, period, shape model, and gravity field is determined. The characterization phase uses a home position at 20 km altitude, and various descents to around 1 km were carried out. During these descents, LiDAR was used to estimate the vertical velocity [55]. Radiometric tracking once again plays a vital role in the navigation of the spacecraft, allowing the precise determination of the orbit.

During the final descent, a target marker is once again deployed, just as with Hayabusa-1. It is released at 100 m, and then from 30 m, the spacecraft is fully autonomous in its descent. Four rovers are included in the mission; one of them failed during deployment. They all use hopping mobility after the uncontrolled ballistic descent [56].

OSIRIS-REx

Launched in 2016, OSIRIS-Rex is the first NASA sample return mission. A robotic shock-absorbing arm on the main spacecraft acquired the sample, and the operations required close proximity navigation on the surface of asteroid Bennu. During the encounter with the target, optical navigation, using images taken by the two camera suites, was the primary means of navigation for proximity operations. LiDAR and altimeter measurements were available for the generation of topographic maps. They were input for autonomous guidance and fault detection algorithms during the Touch & Go event [57]. Optical navigation relies on advanced bracketing techniques to correctly expose both the asteroid and the background sky portion. At the same time, for landmark tracking features, a subset of features is chosen to increase the responsiveness of orbit determination and allow the same accuracy for the body and spacecraft positioning. The GNC subsystem includes 2 STR, 2 ring laser gyros, sun sensors, RCS, and 4 RWs. The landing procedure is Touch & Go as for Hayabusa, and several rehearsals have been made before sample collection [24].

For its navigation, OSIRIS-REx uses a combination of radiometric tracking and optical navigation. The uncertainties in Bennu's ephemeris, size, shape, spin-state, and composition were too large to rely on radiometric tracking alone, creating a need for optical navigation [24]. To solve for the camera pointing error, separate images at different exposure times were taken to image both the star field as well as the asteroid from the same position. A centroiding algorithm is used to determine the inertial attitude of the camera at the image epoch. Once the center of the asteroid is found in the frame, the Centre of Mass (CoM) location is determined using an appropriate algorithm. The camera attitude and the residual between the predicted and observed target centroid are then used to estimate a solution for the body-relative spacecraft state [58].

For close operations and navigation to the touch-and-go zone, landmark tracking is used. A transition period from centroid-based navigation to landmark-based navigation occurred once the digital terrain maps of the surface had been generated. Besides the terrain map, albedo maps and photometric curves were available for these landmarks, making it possible to render the landmark image and compare it to the real camera image. Images of a collection of landmarks are rendered simultaneously on-board and then matched to the visual information, yielding position and attitude information. Besides these measurements, LiDAR sensors were also used to provide additional measurements to the navigation system.

DART

The DART spacecraft achieved the kinetic impact deflection by deliberately crashing itself into the moonlet of the Didymos binary system. The spacecraft was launched on 24th November 2021, and it did not contain a scientific payload other than the needed avionics to support autonomous navigation to impact Dimorphos: sun sensors, a star tracker, and a framing camera are the only sensors. The Small-body Manoeuvring Autonomous Rendezvous and Targeting Navigation is FPGA-based

avionics, and it guides the spacecraft on the target. The framing camera determined the impact point with 1 m accuracy and characterized the Didymos and Dimorphos surface with < 50 $cm/pixel$ [21].

A secondary spacecraft LICIACube piggybacked with DART and acquired an image of the impact through the two optical cameras. The images are downlinked directly to Earth, and the mission will include a flyby of Didymos after the impact [59]. The majority of the flight is navigated using radiometric tracking provided by the DSN [60]. However, the asteroid encounter cannot rely on radiometric. The impact speed will be around 6.6 km/s. With the 70 seconds round-trip-time, this means that it is impossible to use ground-in-the-loop GNC techniques.

Figure 1.5: Image captured by the Italian Space Agency's LICIACube a few minutes after the intentional collision of NASA's Double Asteroid Redirection Test (DART) mission with its target asteroid, Dimorphos, captured on Sept. 26, 2022. (ASI/NASA)

Therefore, an autonomous navigation solution is used. Optical navigation relies on a centroiding algorithm that functions in three steps. First, all pixels in the image that are above a certain brightness threshold are selected. Then, groups of pixels that satisfy this threshold requirement are grouped.

Then the final step calculates a set of statistics associated with each group, such as the size of the group, average brightness, and centroid location. This list of statistics for each group is then used to determine which one of the groups is the asteroid. The largest/brightest group is the default setting. The result of this calculation is the line of sight measurement. Combined with accurate attitude information, the line of sight measurement is transformed into inertial coordinates. Proportional navigation principles are then used in an extended Kalman filter to predict the miss distance at the closest approach.

1.2.2 Planned Missions

Psyche

Psyche is a planned 2023 orbiter mission; the spacecraft mass is 2608 kg; it will use solar electric propulsion and full electric attitude control. It will study the metallic asteroid Psyche, which is considered a proto-planet body [61].

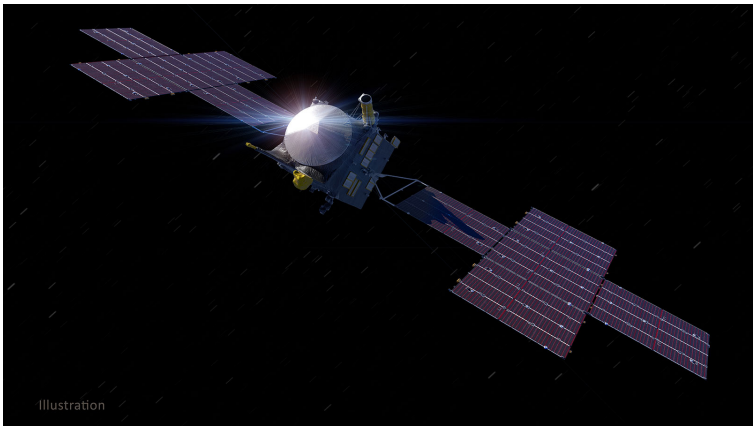

Figure 1.6: An illustration, created in March 2021, of NASA's Psyche spacecraft. (NASA/JPL-Caltech/ASU)

Janus

Janus mission is composed of two 38 kg satellites launching in 2023 together with the Psyche mission. The mission is aimed at investigating how binary asteroids are formed and evolved based on visible and infrared cameras [62].

Hera

Hera will be launched in 2024 to validate the kinetic impact of DART as a planetary defense technique. The mission will prove several guidance, navigation, and control (GNC) technologies. Visual-based navigation will be tested thoroughly during close approach operations. Two different image-processing techniques are used in the autonomous navigation function depending on the range of the asteroid. During the 'far range', when the asteroid fits entirely in the camera image, the image processing will compute the line-of-sight that the navigation filter will use to refine the onboard knowledge. In the 'close range,' the image processing will track unknown features on the surface, and the navigation filter will process them to avoid knowledge degradation [63].

The main guidance and navigation objective are to fuse sensor data between the optical camera, Infrared (IR) camera, and hyperspectral camera to increase vision robustness and finally demonstrate the strategy of sensor switching. The goal is to maintain nominal operation even in case of sensor unavailability. The use of the thermal infrared camera can provide navigation measurements on the dark side of the asteroid, whereas optical navigation cannot provide measurements.

Two CubeSats will fly with Hera: Juventas will attempt an uncontrolled landing without the possibility of retargeting or landing site selection. Milani, the second CubeSat, will take images and measures the characteristics of the asteroid environment [64, 65].

Figure 1.7: An illustration of HERA spacecraft with the two CubeSats.(ESA)

Martian Moons Exploration

Set for launch in 2024, JAXA's MMX is the first sample return mission from Mars' largest moon Phobos [66]. It is thought that Martian moons are captured asteroids, and the mission aims to answer many questions about moons' formation. The development of the landing technology is the top technical issue for the mission, the moon has a strong gravitation attraction compared to the other small celestial bodies, but the gravity is not enough to keep the spacecraft secured to the surface after landing. Following the heritage of Hayabusa, a new landing technology is being developed; four shock-absorbing landing legs are the key technology.

1.3 Research Goals

From the research motivation given in Section 1.1.2 and the current state-of-the-art review (Section 1.2.1), the landing phase emerges as the most critical phase for every mission. All the functionalities that converge on the lander autonomy must be applied to the full extent to grant a safe pinpoint landing.

The main goal of this thesis is then the following: *to research, develop, implement, and test precise and safe landing technologies for a μLander in a binary asteroid environment.*

The research question is answered in two main categories, identified as the core research topics: 1) *environment perception*, and 2) *decision-making*. The initial classification, known as *environment perception*, involves surveying the surroundings to create a map and determine the spacecraft's location within it. The main difficulty compared to Earth-based applications is the absence of GPS signals. When the navigation filter has limited or no knowledge of the absolute position, the filter's estimates may drift due to the accumulation of relative position errors over time. Moreover, the surface geometry is only known up to a certain degree of accuracy, necessitating periodic updates to the onboard map. Additionally, the onboard computers' computational capabilities are significantly less, necessitating lightweight algorithms.

The researched solutions to these challenges are to use optical and ranging sensors in the form of cameras and LRFs. Two novel navigation technologies are developed and implemented (Sections

D-3), which allow accurate performance in all the phases of the landing.

LiDAR unit provides 3D information; however, it is not employed to comply with the μLander architecture mass limitation, as detailed in Section 2.4.3.

Camera-based solutions present a range of advantages, chief among them being their lightweight and compact design. While these solutions are limited to two-dimensional data, this shortcoming is easily overcome by supplementing the data with additional information from a shape model or an altimeter. Camera-based algorithms do not have a maximum range, unlike their LiDAR counterparts. This makes them especially well-suited for landing scenarios where a spacecraft may begin several kilometers from the surface. Moreover, both camera- and LRF-based solutions allow for autonomous navigation around the SSSB without relying on ground-based tracking or communication.

The second category *decision-making* is the ability to steer the spacecraft away from a nominal trajectory. In both landing and surface exploration scenarios, the trajectory is meticulously planned ahead of time to ensure it meets specific landing requirements. However, hazardous objects might not be identified before takeoff if the objects are smaller than the available surface resolution. To address this issue, autonomous hazard detection during flight is implemented to observe the surface at a closer range. If a hazard is detected in the path of the designated trajectory, a new landing site must be identified, and the trajectory must be adjusted onboard.

The challenge for the decision-making is to fulfill multiple landing requirements, e.g., surface slope and roughness, at the same time. The nominal and target landing sites must be assessed for these requirements with precise accuracy and high reliability. A new trajectory has to be feasible by considering the system constraints while being able to adapt to the changing perceived environment.

Since no LiDAR is available, camera images can be segmented to detect hazards. An AI-based algorithm is proposed for this task because they have been proven to excel in segmentation.

Finally, a novel mission concept has been meticulously designed within the framework of the Near Earth Orbit Modelling and Payloads for Protection (NEO-MAPP) study [67]. Serving as a test scenario for implementing and validating the presented research topics, this study aims to address the critical issue of planetary defense. By employing advanced research methodologies, the NEO-MAPP study seeks to develop and assess innovative techniques, instruments, and strategies to mitigate the risks posed by NEOs. Within the study, a complete μLander system is defined with a particular focus on the GNC subsystem:

NEO-MAPP test case is not a limitation; the knowledge gained, and the technological advancements made through this research can be applied to various other small celestial bodies within our solar system, such as asteroids and comets. Additionally, the research outcomes have the potential to extend beyond planetary defense, finding applications in planetary descent missions as well, as described in Section 3.9.

1.4 Contribution of the Thesis

In this section, the key contributions made through my research are outlines, which have advanced the knowledge and understanding of autonomous technologies for μLanders. By addressing the research question, this work has made significant progress in the following areas:

1. Designed, implemented, and tested a LiDAR-free autonomous safe landing site selection technology that fuses image processing and machine learning methods. The algorithm requires

minimum user input as it incorporates landing requirements directly in the pipeline. The technology is applied to real mission images for validation [29].

2. Designed, implemented, and tested an autonomous vision-based absolute navigation system that employs a COTS camera and a laser range finder. The algorithm requires limited prior environment knowledge and a simple ellipsoid shape model. The algorithm can navigate a small lander in a binary asteroid environment up to a few hundred meters from the surface [1, 9, 68].

3. Designed, implemented, and tested an autonomous vision-based relative navigation system that allows one to navigate in the proximity of the surface using relative measurements. The navigation utilizes a novel monocular SLAM-based filter assisted by altimeter measurements to grant a pinpoint landing at the target landing site [69, 70].

4. Defined, designed, and characterized a μLander asteroid mission to safely bring NEO-MAPP payload on the surface using the previous technologies. The problem domain has been identified, GNC requirements are derived, and the concept of operations is designed.

The research developed in the framework of NEO-MAPP highlights the robustness, reliability, and efficiency of the proposed autonomous navigation solutions, vision-based extended Kalman filter, and hazard detection and safe landing site selection framework for space exploration missions. The extended Kalman filter-based navigation solutions are robust to high sun phase angles, irregular asteroid shapes, noisy and distorted camera images, and uncertainty in its initial state estimate. They are computationally efficient, use image processing efficiently, and maintain accuracy in challenging conditions. The Monte Carlo analysis conducted on the filters demonstrates their robustness to boundary conditions. The hazard detection and safe landing site selection framework provides a lightweight and reliable solution for micro-lander autonomy, fulfilling stringent landing requirements with a limited mass budget, and has few free design parameters, allowing for rapid tuning and efficient onboard implementation. Both solutions are highly promising for future space exploration missions and can be applied not only to SSSBs surface but also to planetary landing.

1.4.1 External Contribution

The autonomous spacecraft and landing high altitude phase algorithms discussed in this thesis ([9, 68]) were developed within the framework of a Master's thesis conducted in collaboration with TU Delft. This Ph.D. work serves as the foundational scenario for the Master's thesis, and the author played a significant role in advancing the Master's project, contributing extensively to technical implementations, knowledge transfer, and academic support as the supervisor.

Several innovative contributions emerged from this collaborative effort, enriching the scientific knowledge base. Notably, the suite of sensors employed in this study represents a distinctive combination not commonly encountered in existing literature. The mission scenario assumes the relay of updated ephemeris data from the mothership to the lander. Positioned on the outer pole of the secondary asteroid, the landing site presents a unique challenge as the primary asteroid is situated behind the secondary body (refer to Figure D.2b). This arrangement precludes the use of angles-only navigation due to the absence of separation between the bodies.

During various flight phases, both asteroid bodies are observable within the camera frame, as depicted in Figure D.2a. This research deviates from the standard approach in the literature, where image processing algorithms eliminate one of the bodies, resulting in a single measurement. Instead, this study aims to extract information about both the primary and secondary asteroids from these images, providing a more comprehensive understanding.

Furthermore, the integration of a Laser Range Finder (LRF) with visual data has been explored in the past, primarily in the context of landmark tracking for absolute navigation. In this case, the LRF is employed even in the absence of a highly detailed surface model. This departure from conventional methods demonstrates the adaptability and robustness of the current approach, offering insights into scenarios where detailed surface models may not be available.

In summary, the collaborative efforts between the present Ph.D. work and the Master's thesis have yielded valuable contributions to autonomous spacecraft and landing algorithms, introducing novel elements to the existing body of scientific knowledge. The unique combination of sensors, the challenging mission scenario, and the innovative integration of LRF with visual data mark this research as a significant advancement in the field of autonomous space exploration. More derivation are presented in Appendix D.

1.5 Outline

This section will provide an overview of the thesis structure, guiding the reader through the various chapters and their contents. The thesis is organized into five chapters, each focusing on specific aspects of this work.

Chapter 2 It delves into the mission and spacecraft characteristics, providing essential context for the subsequent chapters. This chapter presents a detailed overview of the mission (i.e., the concept of operations), including its purpose, goals, and target destination. Furthermore, it explores the technical specifications of the spacecraft, discussing its payload and onboard systems with a specific focus on the GNC subsystem.

Chapter 3 It addresses close-range navigation using novel feature tracking and SLAM-based Kalman filtering techniques. It discusses the unique challenges encountered in relative navigation and the significance of feature tracking increased with altimeter knowledge. The chapter outlines the system design, integrates these techniques, and evaluates the navigation performance through experimental results.

Chapter 4 It highlights the development of autonomous algorithms for safe landing site selection and hazard detection. It outlines the methodology used for autonomous site evaluation and presents the hazard detection algorithm. The innovative approach uses a hybrid combination of machine learning solutions and more traditional image processing. Simulation and experimental results are provided to demonstrate the effectiveness of these algorithms.

Chapter 5 It concludes the thesis by summarizing the main findings of the research. It discusses the contributions made to the mission and spacecraft navigation field, highlighting the novel

advancements achieved. The chapter also acknowledges the study's limitations and suggests future research directions to enhance spacecraft navigation capabilities further.

Appendix D It focuses on vision-based navigation for far-range navigation. It introduces the concept of vision-based techniques and their advantages in overcoming the challenges of far-distance autonomous navigation. The appendix presents the strategies for absolute state estimation, including developing a novel altimeter-aided navigation filter. Navigation algorithms are derived, simulator developments are explained, and experimental results are briefly presented and analyzed.

Throughout the thesis, references are provided to ensure the sources' credibility. Additionally, appendices are included to provide supplementary information such as reference frames (Appendix A), units and payloads details (Appendix B.1), and simulator developments (Appendix C) that support the research presented in the main chapters.

Chapter 2

Safe and Autonomous Landing on a Binary Asteroid System

The prospect of landing on binary asteroid systems presents a unique and complex challenge. In this chapter, I delve into the design of a safe and autonomous landing mission for such systems. Firstly, the target binary asteroid system is described. The concept of operations forms the foundation of the current exploration, outlining the mission phases, initial and final conditions, and the overarching goal of achieving a successful landing. Various landing approaches are then explored, including hover & go, touch & go, and traded-off.

Next, landing requirements imposed on the GNC system are derived, examining the objectives and the system drivers. A comprehensive overview of the spacecraft architecture follows, highlighting the GNC avionics suite and the trade-off associated with a LiDAR-free solution.

Furthermore, the propulsion system selection is explored, which includes considerations of thruster type and reaction wheel utilization. Finally, the NEO-MAPP payload is presented.

Through a detailed examination of the $\mu Lander$, this chapter sets the environment and system scenario for the researched solutions in achieving a safe and autonomous landing on a binary asteroid system.

2.1 Binary Asteroid System

The Didymos binary system comprises Didymos (main body) and Dimorphos; its orbit is a near-Earth orbit around the Sun. The perihelion is at 1.01 AU, and the aphelion is at 2.28 AU, then the resulting eccentricity is 0.38. The classical orbital elements are described in Table 3.2, they are helpful for initial orbit propagation, but for accurate calculation, NASA ephemeris is used.

Dimorphos moves in an approximately circular retrograde orbit with an orbital period of 11.9 h, which equals the rotation period assuming synchronous rotation.

Before DART's impact in September 2022, the only dynamical parameters measured directly through observations were the orbital period of the secondary around the primary, their orbital separation, the primary rotation period, and the secondary-to-primary size ratio. The diameters of the binary components are measured to be about 780 and 160 m. A model of the short-term binary dynamics suggests possible librations of the secondary with up to 10° amplitude, depending on its axial ratio.

A shape model of the Didymos primary is based on past radar observations in combination with light-curve data. Radar data cannot provide a model of the secondary since the SNR is too weak, echoes are not sufficiently resolved, and the rotation coverage is limited. The secondary shape is assumed to be a triaxial ellipsoid for modeling purposes.

The primary, with an estimated 2.1 g/cc bulk density (uncertainty 30%), has a rotation period of 2.26 hours that may imply a cohesive strength of several tens of Pa. At this rate, perturbed regolith material may go through take-off/landing cycles and cause loss of fines due to solar radiation pressure. The system may be subject to weak thermal radiation forces (BYORP) with a period drift of no greater than 1 s/yr.

The solar radiation model uses the distance to the Sun to define power availability and external disturbances due to solar radiation pressure. The synthetic-hybrid environment will be generated. The information for the latter is sourced from past mission data, for which detailed orbital and physical parameters are available. The selection of the synthetic models should match closely with the reference target bodies but also enable a flexible adaptation to another mission scenario.

Didymos' orbit will be considered. It is assumed that the heliocentric trajectory is known with enough accuracy for precise orbit determination. Since the change of position w.r.t. the Sun is neglected due to the short landing duration compared to the heliocentric motion, the perihelion of Didymos is defined as a fixed orbital position has to be defined. Firstly, the closer distance to the Sun maximizes the solar radiation pressure. Secondly, the gravitational perturbation due to the Sun is maximum; as a consequence, the perihelion represents a worst-case scenario, and in general, it is different from the actual Hera deployment conditions. The synthetic environment approach allows high-resolution shape models to inject into the optical sensor pipeline; since no high-fidelity information about the actual bodies is available, some proxy bodies will be used. Section 3.3 presents the detailed asteroid generation process.

2.2 Concept of Operations

The mission starts with deploying the $\mu Lander$ from its mothership near Didymos' system. The $\mu Lander$ release point is close enough to navigate toward the asteroids safely and far enough for the safety of the mothership.

In the following sections, the mission phases are presented, the initial condition is described, and the end condition is shown.

2.2.1 Mission Phases

The following is a top-level concept of operation for the $\mu Lander$. The mission is divided into three mission phases:

1. Separation and commissioning

2. Descent

3. Soft static landing

Table 2.1 describes the main mission phases. Descent operations (as in Figure 2.1) can be partitioned into two sets of operational sub-phases: High Altitude Phase (HAP) and Low Altitude Phase (LAP).

Mission Phase	Sub-phase	Functions	GNC Task
Separation & Commissioning	-	Avionics System Check Asteroid Acquisition	Descent towards Home position Pointing Home position
Descent	High Altitude Phase (HAP)	Approach the target body Asteroid parameter estimation Telemetry	Environment parameter estimation Descent towards *home* position Pointing Home position
	Low Altitude Phase (LAP)	Landing site selection Landing preparation Hazard-relative navigation	Descent towards the selected landing site Hazard detection and avoidance Pointing selected landing site
Soft Static Landing	Touchdown	Science surface operation	$\mu Lander$ stabilization Monitor estimated state

Table 2.1: Mission phases

During **Separation and Commissioning Phase**, the $\mu Lander$ initiates an avionics system checkout, and the navigation status is acquired; in addition, potential inter-satellite communication is tested between the mothership and the $\mu Lander$ [71]. Telemetry is returned to the ground and relayed via the mothership during all the operations. In the Separation and Commissioning Phase, the $\mu Lander$ begins an un-propelled slow descent for a short period, and attitude control is granted to start asteroid acquisition procedures.

The **Descent Phase** begins autonomously and is divided into two sub-phases. The sub-phases are related to the avionics suite selection and different navigation and guidance strategies needed for an accurate pinpoint landing. HAP is from the initial condition to a few hundred meters away from Dimorphos with the same relative velocity. This phase includes an initial assessment of the landing region and gathering information about its gravity field, surface properties, and dynamics to support the following close-up operations. The switching to the next phase happens when the sensor suite provides reliable data for the LAP algorithm. Then, the spacecraft moves to a closer altitude, i.e., in the order of hundreds of meters. This phase aims to perform a close characterization and navigate to reach the landing site. It is also considered to switch at a *home* asteroid fixed position; the latter allows more effortless patching between the two sub-phases and can be chosen a few hundred meters above the target landing site position.

During Low Altitude Phase (LAP), the online estimation of the approaching terrain and hazards is fundamental to enable the use of hazard avoidance algorithms. Due to the communication delay between the asteroid's location and the ground, which is expected to be in the order of tens

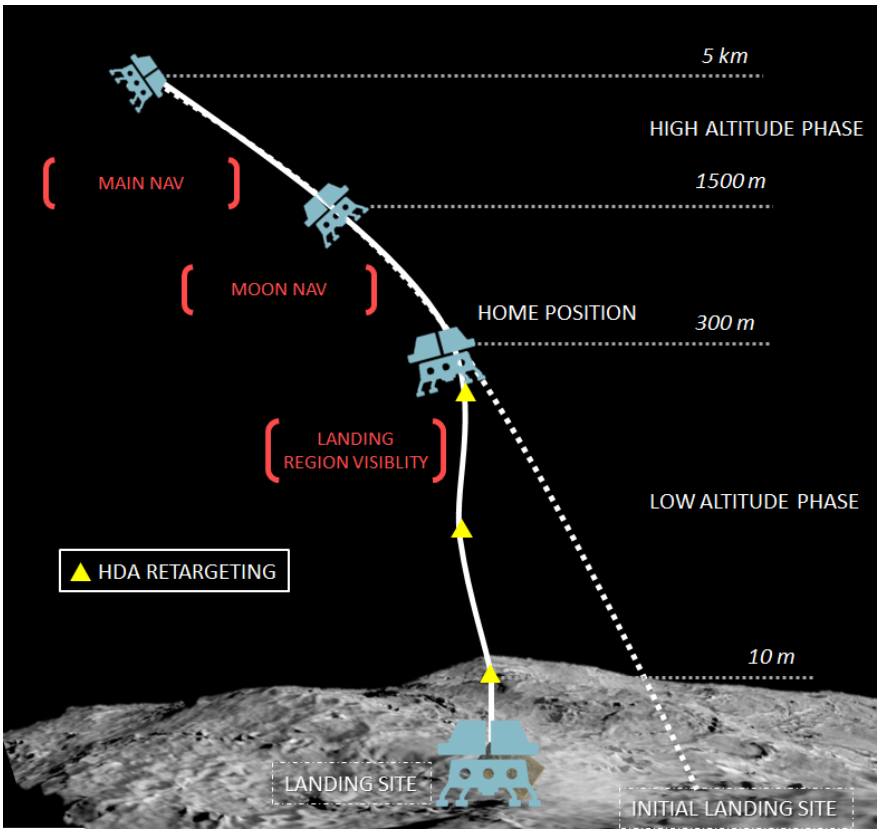

Figure 2.1: Concept of operations during descent from [1].

of minutes, this operation must be performed entirely autonomously up to the final landing site selection and touchdown.

Soft Static Landing includes touchdown (and optionally a few meters ballistic phase) where the *μLander* keeps a stable attitude and position to allow surface operation. The final condition is presented in Section 2.2.3.

The phases differ from GNC modes and are defined according to the other environmental and operational characteristics that the *μLander* experiences. In addition, the switching between phases is done autonomously, permitting the mission objectives. Proximity operations represent a challenging mission phase and require significant advances concerning GNC technologies.

2.2.2 Initial Conditions

The ESA Hera mission has been chosen as reference mission [72], then the Hera Payload Deployment Phase (PDP) is assumed as *μLander* initial condition [73]. In particular, Hera will deploy two CubeSats while the *μLander* in the studied scenario will be deployed. The *μLander* detachment shall not endanger Hera's mission by changing the trajectory safety margin or attitude constraints. However, Hera is not designed to carry a *μLander* on the asteroid; consequently, the orbital initial condition will be the same as PDP, but the deployment velocity is considered a free design parameter. Moreover, using the maximum ejection velocity used for CubeSat of 0.05 m/s relative to Hera spacecraft will cause a ΔV to be applied to the spacecraft because there is a small mass difference between *μLander* (approximately 50 kg) and Hera spacecraft (launch mass 870 kg). From the conservation of momentum:

$$m_{SC}V_{SC} + m_{LAN}V_{LAN} = 0 \tag{2.1}$$

where all the velocities are measured w.r.t the CoM of the system. $V_{SC} = 0.30\ cm/s$ is the ΔV applied to the mothership after the deployment.

The *μLander* trajectory should allow sufficient time for safe commissioning considering deployment uncertainties, but most of the system is checked out before deployment. In particular, actuators and inter-satellite communication are checked after the deployment. The landing operation is initiated via telecommand; the telecommand not only provides the detachment order but also updates the necessary configuration parameters for the *μLander* and makes prior knowledge of the asteroid environment available.

The initial states of the *μLander* depend both on the knowledge of the mothership's state and on the release mechanism, and it represents the initial conditions of the navigation as developed in Section D. The mothership's state is estimated via range measurement techniques from the ground, and the inertial attitude is known from the STRs [74].

Hera Payload Deployment Phase defines the initial condition as in [75], in Table 2.2 the initial conditions with related uncertainties are presented.

State	Nominal Value	Uncertainty	Comment
Velocity magnitude [cm/s]	7-14	10%	Initial velocity w.r.t. I-frame
Velocity direction [deg]	-90/90	0.5	Direction of the deployment velocity w.r.t. Line of Sight (LOS) vector. The angle between the Hera-Primary line and deployment ΔV. The initial attitude is known very accurately with STRs, and then the uncertainty value is conservative.
Distance [km]	5-8	0.050	A worst-case scenario uncertainty is assumed.

Table 2.2: Initial conditions

The initial conditions are given regarding possible ranges compliant with Hera operations. The accurate initial state is defined during specific simulation scenarios. The deployment is allowed from any position around the system within the boundaries of the initial condition. Finally, two design criteria for initial conditions are to be considered:

1. An approach out of the moon orbital plane is preferred because it allows a visual separation between the two bodies for most of the landing; generally, it reduces the possibility of eclipses.

2. An approach from the Sun direction implies optimal illumination conditions of the landing site.

2.2.3 Final Conditions

This section presents different landing strategies, and a trade-off is produced to choose the optimal surface interaction scenario. Several criteria can be identified to select the final conditions, i.e., the target landing site. The concept of autonomous operations foresees the possibility of the operator choosing a landing region, and then the spacecraft will select the landing site within the region. Two main criteria are underlined to select the nominal landing site:

- Minimum moment of inertia of S-frame (as defined in Appendix A) is oriented along Didymos CoM direction. The moon is tidally locked to the latter; if the moon is rotating along that axis, the poles represent the landing site with minimum angular velocity. Consequently, the guidance can more easily null the ground relative motion during landing.

- Eclipse times are lower at the poles; if the moon rotates, more extended illumination is possible.

Given the criteria above, optimal landing sites are represented by the poles; in particular, the one opposite to Didymos can be reached easier coming from outside the binary system; this location is selected as the nominal landing site.

2.2.4 Landing Approach Design

Once reaching the proximity of the asteroid's surface (i.e., *home* position), the LAP starts. Generally, the landing envisages three possible scenarios:

1. Static Landing: the spacecraft lands on the surface and assumes a "stable" configuration while performing the surface operations. The landing point also represents the initial condition for relocation maneuvers. The time scale of these operations can vary from a few minutes to a few hours, depending on the available fuel and the type of operations. In fact, due to the low gravity experienced on the asteroid's surface, an almost continuous thrust is required from the propulsion subsystem to guarantee the needed stability enabling the surface operations. An alternative solution is the use of harpoons [76]; however, these devices greatly limit the flexibility for the relocation phase, in fact for every landing, a new set of harpoons has to be used.

2. Touch & Go: the spacecraft performs a fast "touch" of the surface, in the order of a few seconds, and bounces back to orbit. This operation is concise and imposes significant constraints on the sampling mechanism. In this case, mobility is limited and only possible if a series of TAG events are executed; consequently, mission complexity increases.

3. Hover & Go: the spacecraft does not have any contact with the surface of the asteroid but hovers over it. As for the Touch & Go case, if a sampling mechanism is present, this approach imposes severe constraints and may cause uncertainties regarding the sample site characteristics. This solution also implies that the GNC algorithms can maintain the spacecraft at a very low altitude (order of tenths of centimeters) from the surface to enable sample collection.

Hover & Go

In the Hover & Go mission option, the spacecraft does not touch the surface but only an appendage. The main feature of this option is the limited interaction between the spacecraft and the asteroid's surface. This reduces the level of interaction between the spacecraft and the asteroid and the risk of the spacecraft becoming 'stuck' on the asteroid. However, the scope of the present *μLander* is surface direct interaction and mobility for relocation. For Hover & Go, the limited time for in-situ measurements or other experiments is a significant disadvantage. This reduces the scientific return.

In addition, this strategy does not require any dedicated landing system, therefore saving dry mass. Instead, a dedicated mechanism should be adapted to the transfer system (if a robotic arm, for instance) to absorb the shocks at touchdown and the residual lateral velocities and avoid the tumbling of the spacecraft. However, this mechanism can probably be much lighter than landing legs have to be. The stay time above the surface can be very short, depending on which sampling mechanism is used, limiting integrated radiative thermal effects and propellant consumption.

Overall, such a concept can save a non-negligible mass on the spacecraft. For instance, this mass reduction concerning a landing strategy will translate into cost savings, an advantage for this mission. This cost-saving seems balanced by the higher complexity of the specific systems required for this approach, such as sample transfer, GNC, and touchdown absorbing mechanism. The former needs further technological advancements to reach an adequate level of development in Europe.

The Hover & Go option is the most demanding for the GNC system because the spacecraft has to remain aligned with the terrain and at a constant distance to the ground with high stability to perform the sampling. Moreover, the non-uniform gravity perturbations are not negligible during this period near the surface, e.g., deployment of the sampling mechanism.

The need for a remote sampling mechanism and long-reach deployment system, which can cancel any residual velocities, also adds to the mission complexity.

Touch & Go

The Touch & Go mission option uses an impulsive rebound of the spacecraft with fast sampling and immediate re-orbiting. This implies that the spacecraft has a short but direct interaction with the surface, potentially requiring the adoption of the same landing leg design for the landing mission.

The Touch & Go option offers no significant advantage over the Hover & Go or the Static Landing as the spacecraft makes complete contact with the asteroid but has a limited time ($<$3s) for the sampling operations. Moreover, the stability of the spacecraft during the sampling operations represents a critical aspect that could compromise the success of the mission, together with a fast and autonomous capability to react to events/hazards is required. In the Static Landing option, the spacecraft fully lands on the asteroid to perform sampling operations. The GNC system and the firing of reaction control thrusters ensure the stabilization of the spacecraft during the stay.

Static Landing

For the Static Landing option, the GNC system shall apply a force to maintain the spacecraft on the ground and avoid rebound. In fact, given a restitution factor $C_r = 0.5$ and a touchdown velocity of V=1 cm/s relative to the ground, the required time to achieve a rebound height smaller than 0.10 m is approximately 40 minutes. The sampling operations are, therefore, more secure in the full

landing option. In some cases, anchoring systems (e.g., harpoons) could be envisaged to enhance the stability of the *μLander* on the surface, but as discussed, limiting mobility function on the ground.

The extended period available on the surface for scientific operations gives additional flexibility in the type of analysis; moreover, it allows stable and accurate initial conditions for relocation maneuvers.

Trade-Off Landing

The preliminary trade-off for the mission type is presented in Table 2.3. Based on this trade derived from previous investigations, the preferred mission option would be a static landing on the asteroid because it simplifies the stabilization of the *μLander* before the sampling and surface operations and allows relocation.

Criteria	Weight	Max Value	Hover & Go	Touch & Go	Static Landing
Technical Advancement	0.3	10	7	8	9
Mission Return	0.3	10	4	5	9
Risk	-0.2	10	6 (low risk)	6	9 (high risk)
Cost	-0.1	10	6	6	8
Complexity	-0.1	10	5 (low complexity)	6	8 (high complexity)
Total			1	1.5	2

Table 2.3: Landing Approach Trade Off

The goal of the present work is to define a system that is flexible and adaptable to a variety of missions; the static landing approach represents the optimal landing condition to have increased scientific return on the asteroid surface, allowing less constrained payload, in particular, it removes the need for a fast sampling mechanism. Moreover, static landing is a real technological advancement, and few missions succeeded in this approach; being an ambitious goal to pursue.

Finally, the static landing scenario seems to provide the highest success probability to meet the science requirement of deploying instruments on the surface or collecting samples. This scenario offers various advantages, among which the possibility to:

- Select the operation to be performed with support from the ground on a longer time scale
- Perform multiple attempts on the same sampling site without the implementation of critical maneuvers
- Select more sampling mechanism concepts (more sampling mechanisms are compatible with this type of mission)
- Allow stable relocation and mobility initial condition, decreasing mission complexity

Finally, the contamination and temperature aspects have to be taken into account. From a mission and system point of view, the Hover & Go, as well as the Touch & Go, are providing a lower level of contamination and temperature of the sample site concerning the case of the Static Landing.

Based on the discussion provided in the previous section, the following is assumed:

1. A static landing is selected for the landing approach. This solution increases the probability of directly interacting with the surface on a longer time scale.

2. The target selection represents an essential input for understanding the suitability of the approach. Although the landing option seems to provide more substantial advantages, it has to be noted that this can be severely affected by the size of the asteroid. Landing on a few hundred meters in diameter asteroids is expected to be more complex than landing on one a few kilometers in diameter.

3. Final conditions (target landing site) can be defined in the body fixed coordinates of Dimorphos. In particular, the pole opposite Didymos represents an optimal choice.

2.2.5 Retargeting Operations

The Safe Landing Site Selection (SLSS) functionalities run at specific gates during LAP to accomplish the mission target, see Section 2.2.1 and Section 4.4.8: landing on the secondary body of the Didymos binary system.

LAP starts approximately 300 m from the surface and ends with the soft touchdown on the secondary body. Once the target landing site is defined before deployment, the system can refine the selection according to safety and mission return criteria (e.g., visiting a specific region) during descent and define an updated landing site on board. Safe Landing Site Selection (SLSS) routine is discrete to avoid continuous shifts in the target landing site position while landing. Three SLSS gates are identified, as shown in Figure 2.1:

1. when the LAP begins at around 300 m from the surface (resolution = 0.31 m/pixel)

2. when the mid-point of the trajectory is reached at 150 m (resolution = 0.16 m/pixel)

3. at 50 m from the surface, the last retargeting gate is reached (resolution = 0.05 m/pixel)

2.3 GNC System Landing Requirements

2.3.1 Objective

The need of the mission is an autonomous and safe landing in a partially known environment from a farther distant orbit leading to asteroid surface interaction of the µLander. The identified mission objectives are:

- Small deep space platform deployment
- Asteroid physical properties acquisition
- Surface science package landing

The GNC subsystem shall have a reduced impact on the spacecraft and allow a flexible adaptation to different mission architectures. Most of the requirements are defined bottom-up from the GNC level to the mission level because the mission represents only a test case, and it is helpful to demonstrate the flexibility of the proposed solutions.

2.3.2 System Drivers

In this section, the major system drivers from which the requirements are derived:

- Autonomy: the long signal flight time in the order of tenths of minutes implies that the system shall perform the operations autonomously. Autonomy shall be granted during both the nominal decision-making process and accidental malfunctions always to prioritize mission survival.
- Robustness: due to the partially known environment, the *μLander* shall robustly react to unforeseeable/unmodelled forces and avoid divergence from the nominal onboard derived guidance profile.
- Landing Site Selection: once the target landing site is defined before the deployment, the system can refine the selection according to safety and mission return criteria (e.g., visiting a specific region) during descent and define an updated landing site onboard.
- Soft Landing: the system shall perform a touchdown with minimal translational and rotational velocity. Moreover, it should allow a working functionality for the payload to be stable on the landing site for a determined time.

2.3.3 Landing Requirement Definition

The Landing Site Selection driver expresses the rationale to have an autonomous landing site detection and selection on the *μLander*; from this driver, the following SLSS requirements are derived. The SLSS requirements define those constraints related to the SLSS functionality and the target landing site.

Title	Description	Rationale	Note
Landing Footprint	The landing site area shall be within a circle of 100 cm + 40 cm radius	The landing footprint is the geometrical projection of the *μLander* area onto the surface. The landing footprint considers the mechanical landing footprint and adds a safety margin of 40%	The landing footprint is the area on which the *μLander* touchdown. The dimensions are used in the SLSS as a fundamental parameter to verify that this area is clear from hazards.

Title	Description	Rationale	Note
Illumination	The surface shall have a minimum Sun phase angle of 45° during touchdown	Shaded areas are considered unsafe because it is impossible to identify any hazard in them. Dark areas the sensors system cannot process should be classified a priori as unsafe; they could represent a deep crater or the shadow generated by a boulder hiding more hazards.	The sun phase angle is granted during mission design on the ground.
Slope	The maximum landing footprint slope w.r.t. the local gravity is 30°	The *μLander* physical characteristics limit the slopes where it can land to avoid keeling.	Local gravity is assumed to be known.
Closest Landing Site	The selected landing site shall be closer than 50 m from the nominal landing site.	The selected target landing site shall be in the neighborhood of the nominal landing site. The latter is chosen before deployment and has a high scientific interest.	The nominal landing site is selected on the ground before the deployment. Its knowledge is limited, and if it is unsafe, the SLSS re-target to a different landing site
Minimum Distance	The target landing site shall be at least 1.5 m from the closest unsafe landing site	The safe landing site should be far from any unsafe landing site to account for performance error and increase system safety.	-
Roughness	The maximum local rock density for a target landing site is 80%	Rock density is defined as the area containing detected rocks divided by the overall area analyses (see Section 4.4.4).	The local rock density is an indirect measurement of the surface roughness [77]. The physical and geometrical characteristics of the *μLander* touchdown system determine the maximum hazard size the *μLander* can take without damaging any part of the system.

Table 2.4: SLSS system requirements

2.4 Spacecraft Architecture

The available mass budget largely determines the *μLander* design. The following mass characteristics play an important role:

- Mass of the *μLander* to be launched
- CoM position
- Moment of Inertia (MOI)

Generally, a μLander is defined as a mass ranging from 10-150 kg. Evaluating the actual and past missions to Near-Earth objects and the successful lander missions on Mars, a system total wet mass of 50 kg is assumed, including a 20 % margin.

In Table 2.5, the estimated relative mass of the subsystems is given in percentages. The percentages are averaged out over several spacecraft. For the GNC subsystem, a 7.5 kg mass is allocated considering AOCS, and it is excluded part of the propulsion system; in particular, the total mass estimate is made a requirement to have selection criteria during design, the decision-making process for avionics shall consider this value.

Subsystem	(%)	Mass [kg]
Structure	15	7.5
Propulsion (RCS)	10	5
GNC	15	7.5
Power	12	6
TT&C	5	2.5
Thermal	2	1
Payload (incl. antennae)	9	4.5
Wiring	5	2.5
Data Handling	4	2
System Margin	20	10
Propellant	3	1.5
Total	100	50

Table 2.5: Mass Budget

The *μLander* system mass represents a key driver for overall complexity and potentially implemented functionalities into the system. Thus, it is a crucial figure for overall feasibility. As presented in Table 2.6, the estimated and calculated mass properties are needed assumptions for the GNC system development.

Parameter	Unit	Value
Mass (wet)	kg	50
MoI w.r.t. B-frame	$kg \cdot m^2$	$\begin{bmatrix} 1.021 & 0 & 0 \\ 0 & 1.021 & 0 \\ 0 & 0 & 1.021 \end{bmatrix}$

Table 2.6: Mass properties of the NEO-MAPP *μLander*

2.4.1 GNC Avionics Suite

The following section briefly describes the selected sensors; detailed specifications can be found in Appendix B.1. Moreover, some trade-offs are identified to assess the optimal sensor configuration and actuators definition for the specific concept of operations; the trade-off results are presented in Appendix B. Figure 2.2 shows the sensor's configurations.

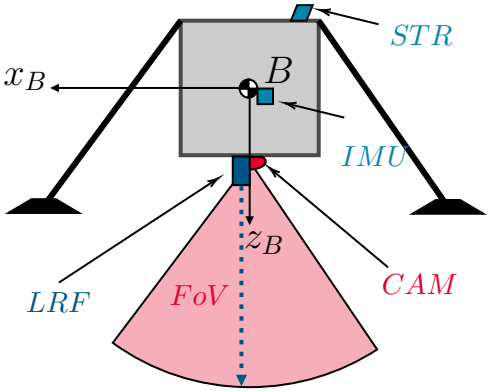

Figure 2.2: Sensor Configurations

The baseline avionics for the GNC system includes:

- STR (B.1.1): the unit provides attitude information, and it is used on a classical gyro-stellar estimator by measuring attitude quaternion.
- IMU (B.1.3 and B.1.2): the units are tailored for low gravity field environment, and it is used for dynamic model propagation in the navigation filters.
- Camera (B.1.4): it is the fundamental unit for navigation, providing different measurements according to the mission phases (i.e., centroid estimation or tracked features).
- LRF (B.1.5): it represents a very accurate LOS measurement used in both the developed navigation filters and for the SLSS functionalities.

2.4.2 Payload

The suitable payload for NEO-MAPP has been identified by NEO-MAPP partners' payload developments. The payload specifications are presented in Table 2.7.

Payload	Description	Value	Reference
Inter-Satellite Link (ISL) technology	Range Rate Accuracy (2 σ)	30 mm/s	[71]
	Range Accuracy (2 σ)	1 m	
	Frequency	5 s to 600 s	
Bistatic Radar Low Frequency Radar (LFR)	Carrier Frequency	50-70 MHz	[78]
	Resolution (monostatic)	2.5 m	
	Pulse repetition	5 s	

	Mass	1360 g	
	Mean power	10 W	
Gravimeter	Dimensions	1U Cubesat	[79]
	Mass	400 g	
Seismometer	Volume	2 l	[80]
	Mass	2 kg	

Table 2.7: Payload Overview

2.4.3 LiDAR-free Solution Trade-off

Next, I explore the trade-off between utilizing LiDAR-based solutions and LiDAR-free alternatives, examining their respective advantages and limitations. Finally, I discuss the selection process for the propulsion system, analyzing various technologies' implications on the avionics architecture and overall vehicle performance.

Table 2.8 presents a comparison between LiDAR units: it appears that all of the LiDAR options currently available are either too heavy or out of range for the mission scenario.

A LiDAR-free mission will be necessary to stay within the mass constraints of the GNC system. While the HERA LiDAR is the most promising option, it is still in the early development stages. It has a minimum range of only 200 m, making it unusable during landing proximity operations [81].

However, it is essential to note that not having a LiDAR onboard does come with inevitable trade-offs: the spacecraft's ability to accurately sense its surroundings and make necessary adjustments could be compromised, potentially leading to higher levels of risk during landing operations.

Unit	Mass	Range	Accuracy	Comment
HELENA [81]	$<2kg$	200 m-14 km	n/a	Low TRL. The minimum range does not include proximity operations
Hayabusa-2 [55]	3.5 kg	50 m-50 km	0.5 m	Flown on Hayabusa-2, heavy and over-performing for the current mission scenario.
Goldeneye [82]	6.5 kg	-	-	Mass beyond GNC envelope, state of the art for space-borne LiDAR

Table 2.8: LiDAR Comparison

2.4.4 Propulsion System Selection

Thruster Type

Table 2.9 provides information on three propulsion systems for asteroid landers: electric, cold gas, and chemical propulsion.

Type	Electric	Cold gas	Chemical
Reference	ACFT Airbus [83]	CGT1 AST [84]	MR-401 Aerojet [85]
Min Impulse Bit	-	-	60 sec
Isp[s]	1500	65	184
Propellant	Xenon	Nitrogen	Hydrazine
Mass [kg] (each thruster)	1.5	0.12	1
Thrust Range [N]	0-0.01	0-0.01	0.07-0.09
Power to Thrust Ratio [W/mN]	20	-	-

Table 2.9: Thruster Comparison Properties

Electric propulsion offers a much higher specific impulse (I_{sp}) of 1500 seconds, providing a higher velocity change per propellant unit than the other two systems. Using Xenon as a propellant offers higher efficiency, and the power-to-thrust ratio of 20 provides a more sensitive and controllable thrust, making it useful in low-gravity environments. However, the mass of the thruster is higher at 1.5 kg each.

On the other hand, cold gas propulsion uses Nitrogen as a propellant, which is less efficient. Still, it provides a smaller impulse bit suitable for more minor, more precise maneuvers. It is a mature technology with a Technology Readiness Level (TRL) of 9, which means it has been extensively tested and is reliable. Additionally, the thruster's mass is the lowest at 0.12 kg, making it more lightweight, simple, and inexpensive.

Finally, the chemical propulsion system offers a higher minimum thrust range than the other two systems, with a maximum thrust of 0.07-0.09 N. This higher thrust is unsuitable for sensitive maneuvers in low-gravity environments but could be helpful for landing and take-off phases. The Hydrazine propellant used is not as efficient as Xenon, and the mass of the thruster is higher at 1 kg each. However, chemical propulsion is a well-established technology, and the MR-401 Aerojet system has been used extensively in space missions.

In conclusion, cold gas propulsion has several advantages, making it a suitable option for space missions. Firstly, it is a mature technology with a Technology Readiness Level (TRL) of 9, which means it has been extensively tested and is reliable. Additionally, it has a small impulse bit, making it ideal for more minor, more precise maneuvers. Cold gas thrusters are also simple, robust, and inexpensive. For missions that require only landing, electric thrusters may be too heavy. However, electric propulsion may become the preferred solution for more considerable velocity changes. Electric thrusters have a TRL of approximately 6.

Assuming a generic cold gas thruster with a thrust range of 10-50 mN, an I_{sp} of 60, and a mass of 0.3 kg, different options such as Nanoprop [86], VACCO [87], or CGT1 DASA [88] can be considered.

Reaction Wheel Utilization

The assessment in Table 2.10 shows that using RW and cold gas RCS have their advantages and disadvantages.

Regarding micro-vibrations, the utilization of RW can introduce such disturbances; however, their amplitudes can be mitigated by implementing damping isolators. Nevertheless, it is worth noting that micro-vibrations may also reach negligible levels, thereby minimizing their significance. Regarding the slew maneuver, both RWs and RCS demonstrate comparable ratings, yet the RCS configuration exhibits a higher threshold for torque. Moreover, the RCS configuration holds the advantage of being lighter in mass, rendering it an appealing option in terms of weight considerations. From a cost perspective, incorporating RWs entails additional expenses. Furthermore, RWs tend to possess a higher complexity rating due to their susceptibility to errors and necessitating more extensive verification processes. Power-wise, the RCS requires less energy, whereas RWs offer the advantage of a longer operational lifespan and enhanced resilience against radiation. The parasitic ΔV is similar for both alternatives, with wheel offloading performed before landing, while a balanced thruster configuration effectively minimizes the impact of ΔV on the wheels.

Regarding Technology Readiness Level (TRL), applying RWs for interplanetary missions has not been previously undertaken, whereas RCS enjoys a higher TRL rating. Lastly, operational constraints may impose the necessity of concurrently employing both RWs and RCS.

Taken as a whole, the comprehensive assessment table illustrates the respective advantages and disadvantages of both alternatives. However, considering the brief duration of the mission phases in the case of NEO-MAPP, it is determined that using RWs would be redundant. Consequently, the decision is made to refrain from incorporating RWs into the NEO-MAPP system.

Criteria	RW	Cold gas	Comment
Micro-vibrations	2	3	RW introduce micro-vibrations
Slew	2	3	-
Mass	2	3	4+1 kg vs 4 kg (12 RCS + 4 RWs configuration)
Cost	1	3	-
Complexity	1	3	-
Power	2	3	-
Lifetime	3	1	-
Parasitic ΔV	2	3	Effect of wheel offloading
TRL	2	3	Never used CubeSat RW on an Interplanetary mission.
Total	17	25	-

Table 2.10: Reaction wheels assessment table (low score is worse)

Chapter 3

Feature-based Altimeter-aided Navigation for Close Range

In this chapter, a novel approach of feature-based altimeter-aided navigation is explicitly designed for close-range scenarios. The Introduction outlines the significance of the research and its contributions to the field of relative navigation. Subsequently, the prevailing Low Altitude Navigation Strategies are explored to identify the existing limitations and pave the way for the current proposed solution. An Environment Modelling section highlight the challenges in the asteroid modelling and in building a representative simulator. The subsequent sections focus on crucial aspects, including Relative State Estimation, where the techniques employed are detailed to estimate the platform's state in relation to its surroundings. Next, Sensors and Measurement Models are presented, which form the backbone of this feature-based approach. Furthermore, the Navigation Filter Development is presented, which illustrates the development and implementation of this navigation filter based on the proposed feature-based methodology. The navigation filter workflow is applied to a lunar landing test case to prove the applicability of the solution to a planetary landing. Finally, the chapter culminates with a comprehensive results section, thoroughly evaluating the system's performance in various scenarios.

3.1 Introduction

This section investigates the navigation solution for the second phase of the landing. The primary objective is to enhance the accuracy and robustness of navigation strategies at low altitudes where absolute measurements are unavailable. Since the secondary fills the field of view, the centroid cannot be estimated, and a feature-based approach is used. The features are extracted and tracked from the observed images and used together with the LRF measurement to estimate the state of the lander. In this approach, no absolute information is measured, and the relative state with reference to the surface is observed. The solution is intended to be used at short distances from the surface. The chapter contributes to developing a novel navigation filter that fuses efficient features and LRF measurements by granting a high accuracy and reduced drift of the solution.

3.2 Current Close Range Navigation Strategies

3.2.1 Current Asteroid Relative Navigation Systems

Relative navigation built on feature-based techniques has been successfully used for a few asteroid landing missions, providing a reliable solution for spacecraft navigation without GPS signals. However, a pure relative solution has never been used (without prior information). Pien [89] conducted pioneering research on the autonomous exploration of Mars, focusing on precision-landing strategies and autonomous navigation, which can be considered synonymous with relative navigation. This foundational study emphasized the significance of relative navigation in space missions.

DIMES [90] represented a groundbreaking milestone as the first use of computer vision to control spacecraft landing. DIMES measured horizontal velocity using two camera images as a Vision-based Navigation (VBN) system. This approach was vital for countering potential steady-state winds and mitigating hazards to the airbag landing system.

The Autonomous Precision Landing Hazard Avoidance Technology (ALHAT) project [91], developed by NASA, aimed to enable safe, precise lunar landings without lighting constraints and avoid hazards for human-scale vehicles. ALHAT targeted landing accuracies ranging from hundreds to tens of meters, and the project focused on advanced GNC hardware and software technologies, reaching TRL 6.

In the context of space missions, unexpected challenges often arise, as seen in the Osiris Rex mission [58]. Due to the high boulder density on the asteroid's surface, stricter landing requirements were necessary. The use of Natural Features Tracker (NFT) as the baseline navigation method [92] instead of LiDAR proved essential, as LiDAR had limitations in cross-track accuracy and sensitivity to albedo heterogeneity.

Hayabusa 2 [54] employed a Target Marker Navigation (TMN) system, deploying a small target marker on the asteroid's surface. Using a high-resolution camera, the spacecraft determined its relative position and orientation, achieving precise positioning during mission operations.

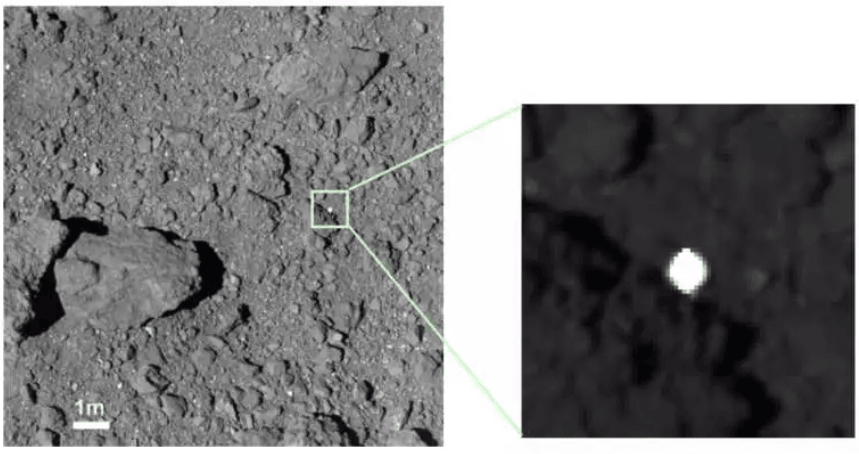

Figure 3.1: Hayabusa target marker on Ryugu (JAXA)

The Ingenuity mission [93, 94], a part of NASA's Mars 2020 project, showcased the application of relative navigation principles for aerial exploration on Mars. Deploying a small helicopter drone to the Martian surface, Ingenuity employed a LRF and state filter update frequency to determine its position and orientation during flights, demonstrating the viability of aerial exploration in Mars'

atmosphere.

In all these missions, relative navigation based on features-based techniques provided a reliable and accurate solution for spacecraft navigation. However, pure relative navigation still represents the frontiers of SSSBs and planetary explorations.

3.2.2 Challenges in Asteroid Relative Navigation

In the domain of VBN, it is essential to establish clear definitions for the terminology employed in this study. Typically, all methods using images or DEMs/depth maps to localize the lander are collectively referred to as VBN systems. However, it is crucial to differentiate between methods that utilize images to position the lander relative to a pre-existing map or ephemerides and those that solely perform localization based on the currently sensed image from the spacecraft. The former method can determine the inertial, absolute position of the lander (as in Section D). At the same time, the latter can only provide localization relative to the current image, thus minimizing the accumulation of relative error from the IMU over time. In this work, I will use the term *absolute navigation* to refer to the former method and *relative navigation* for the latter, emphasizing the critical distinction between them.

A significant challenge is the necessity for autonomy, a requirement shared across various mission aspects, including relative navigation and already presented in Section 1.1 and Section D.

It is essential to note that *absolute navigation* and *relative navigation* significantly differ in their applications. Absolute navigation can guide a spacecraft toward a predefined landing region, whereas relative navigation can be employed to avoid hazards identified in an onboard hazard map or achieve a precision landing without preventing hazards. The accuracy of absolute navigation methods depends on the resolution of the reference maps, ephemerides (as shown in Section D), or catalogs used for matching, whereas pre-existing data do not restrict relative navigation. While absolute navigation can ensure safe and precise landing when very high-resolution surface images are available, such as in the case of planetary landings, it is insufficient for ensuring safety on other celestial bodies where hazardous landing regions may be present and detailed terrain maps are unavailable.

Addressing these challenges, features-based relative navigation is a promising approach to enhance accuracy. By utilizing landmarks and distinct surface features for navigation, features-based methods offer improved precision in determining relative positions, allowing for more reliable and successful missions.

3.2.3 Recent Research

Most terrain-relative navigation technologies fall into the absolute navigation section as defined above. As presented in multiple surveys [95, 96], matching measured landmarks [97–99], craters [100], or DEMs to pre-existing catalogs or data is the current state-of-the-art technology.

In the context of navigation through unexplored terrain or as the spacecraft approaches its landing site, absolute navigation methods face limitations in recognizing landmarks or centroids. During these critical phases, the vehicle is most vulnerable, demanding the utmost reliability in navigation systems. In such scenarios, where traditional landmarks and reference points are unavailable, the need for alternative and robust navigation strategies emerges. Hybrid approaches fusing landmarks

matching with features tracking are available [101].

According to the degree of a priori information used, different features-based navigation range from using just a rough shape model [102] to fully autonomous systems [103, 104].

Decreasing the dependency on a-priori data (e.g., landmarks, shape models, etc.) requires advanced navigation techniques such as Simultaneous Localization and Mapping (SLAM) and visual odometry. SLAM is a technique that allows a spacecraft to simultaneously create a map of its surroundings and localize itself within that map. This is done using sensors such as cameras [105] and LiDAR [106] to measure the distance and orientation of nearby objects. By combining this sensor data with information about the spacecraft's motion and dynamics, SLAM algorithms can accurately determine the spacecraft's position and orientation relative to the planetary surface without pre-existing information.

3.2.4 Research Novelties

This research explores several novel technologies to address the challenges the landing environment poses and μLander architecture on Simulataneous Localization and Mapping (SLAM) systems. The weak gravitational pull necessitates precise landing velocity knowledge to avoid crashing or bouncing off from the surface, while reduced parallax at far ranges complicates feature triangulation in structure-from-motion methods. Additionally, the large stereo-camera baseline required to account for the landing altitude excursion is impractical for the μLander size. Accurate position knowledge is vital for targeting the landing site. At the same time, the absence of a LiDAR unit hinders depth estimation, and ConOps eliminates the possibility of loop closure during landing.

To overcome these challenges, several innovative approaches have been developed. A monocular camera method is introduced to address the limitations of stereo-camera and LiDAR. A SLAM-based approach robustly tracks features and improves the limitations of structure-from-motion methods. Utilizing a LRF enhances observability along the LOS without relying on prior shape models. An Extended Kalman Filter (EKF)-SLAM is implemented to achieve accurate velocity and position estimates, and efficient data fusion techniques are employed. These technological advancements offer promising solutions to effectively navigate and address the complexities of the landing environment and μLander architecture.

3.2.5 Close Range Navigation Architectures Review

An overview of the relative navigation methods and related sensors in the literature is shown in Table 3.1. The analysis is limited to features-based filters with limited or without prior knowledge. An EKF implementation will be used because it has shown promising results compared to particle filters or graph-based implementations; these have much higher computational and implementation complexity with minor result improvements [107]. The LRF/altimeter unit is fundamental to increase the observability normal to the surface, and the monocular approach represents the optimal configuration to account for the lack of LiDAR and the limited stereo baseline on the μLander. Finally, a limited number of tracked features is employed to keep the filter state reasonable in size while granting accurate landing. The HERA implementations [74] are close to the researched one. However, it is not tailored for a landing scenario, has substantial avionics differences, and has limited published details.

Paper	Architecture	Sensors	Description
[108]	EKF-SLAM	Monocular Camera	Not a space application, indoor environment, heavy implementation, dynamics features number.
[109]	Graph-based	Earth-relative position, Monocular Camera	Graph-based heavy implementation, additional non-visual measurement, proven SLAM-feasibility, not designed for landing missions.
[106]	Graph-based, EKF	LiDAR, IMU	LiDAR unit employed, GPU used, very power intensive, not for landing but for characterization phase.
[74]	EKF	Monocular camera, IR camera, laser altimeter, IMU	Mission experimental phase, additional sensors used, features tracking, HIL validated, promising solution but limited details.
[103]	Particle Filter	Monocular camera, Altimeter, IMU	High computational effort, features matching, loosely coupled approach for altimeter, a large number of particles for accuracy

Table 3.1: Overview of architectures in reviewed literature

3.3 Environment Modelling

In the current section, a detailed environment modeling description is provided. Since a high-fidelity model is needed for simulation and testing, a combination of synthetic properties and actual estimates is used to define a high-resolution mission environment. The focus is an enhanced environment compared to the available knowledge to accurately model the interaction between spacecraft and asteroid scenarios.

3.3.1 Reference Target Body

Baseline Parameters for Binary Asteroid Environment

The baseline parameters of the target bodies are summarized in Table 3.2. More detailed information is contained in [110].

	Baseline Value
General	
Target Name Primary	Didymos
Target Name Secondary Dimorphos	
Physical Parameters Primary	
Overall dimensions	832 m $\times$ 837 m $\times$ 786 km
Rotation Period	2.26 hrs

Rotational speed	7.7227e-04 rad/s
Rotation Axis (body fixed z-axis w.r.t. J-frame)	RA: 270 deg Dec: -87 deg
Obliquity	175 deg
Orbital inclination	0 deg
Physical Parameters Secondary	
Overall dimensions	208 m $\times 160$ m $\times 133$ km
Rotation Period	11.9217 hrs
Orbital Period	11.9217 hrs
Rotational speed	1.4640e-04 rad/s
Rotation Axis (body fixed z-axis w.r.t. J-frame)	RA: 90 deg Dec 87 deg
Density	2170 kg/m^3
Total Volume	18.7 km^3
Total System Mass	5.278 10^{11} kg

Table 3.2: Baseline parameters for target body environment

3D Shape Model

The high-resolution 3D shape models are given in the format of an obj-file. The shape models are used for several purposes:

- Model the image processing and camera acquisition
- Model the laser range finder acquisition
- Generate a machine learning dataset for the hazard detection functionalities
- Derive the gravity fields of the two bodies using a constant density model

The models importing pipeline includes two main operations for each model (primary and secondary):

1. Rescaling: in which the high-resolution shape model fits the assumed actual asteroid size as in [110].
2. Enhancing, in which the high-resolution shape model is further detailed, adding boulders, base asteroid Perlin noise, and surface features (e.g., craters.)

The 3D polyhedron models of Bennu and Itokawa are stretched to match the ellipsoid models' extent along their principal inertia axes. After calculating the volume of the reshaped 3D polyhedron models, the density of the two asteroids is recalculated to match the mass of the reshaped asteroids to the masses.

These operations are the necessary pre-processing for the shape model. In the following, it is referred independently to rescaled Bennu/Itokawa or Didymos/Dimorphos.

The rescaled version is used for gravity field generation (boulders mass is neglected).

The two available shape models are enhanced to increase the resolution. The available ESA/JPL shape models are used to model the system. These models are the most updated knowledge available of the binary system. The Bennu shape model is used for the primary body and rescaled according to Didymos' main moment of inertia (MOI) to simulate the mass properties. Bennu shape model is chosen because it is a high-resolution model, and the spherical shape fits Didymos estimated shape. For Dimorphos, the estimated NASA/JPL model consists of a low-resolution ellipsoid model, which is not sufficient to perform high-fidelity landing sequences using vision-based navigation.

Figure 3.2: Synthetic Didymos Environment Generated with ESA/PANGU Software

The model is enhanced following three main steps: base model improvement, surface features addition, and albedo matching as presented in Figure 3.3. In the first step, a high-resolution Itokawa asteroid model [111] is rescaled to match Dimorphos' main moment of inertia (MOI) to have a more representative body, compared to the ellipsoid. Itokawa is chosen because it has a well-known high-resolution shape model, and the highly oblate shape fits closely with the Dimorphos estimated ellipsoid compared to other NEO such as Bennu or Ceres. This step allows to have increased base surface resolution and matches Dimorphos mass properties, i.e., MOI); the rescaling factors are shown in Table 3.3.

MOI Axis	Itokawa [km]	Dimorphos [km]	Scale Factor
X	0.562	0.208	0.370
Y	0.306	0.160	0.523
Z	0.244	0.133	0.545

Table 3.3: Itokawa Dimorphos Scale Factors

Perlin noise is applied to the base asteroid model to increase the base mesh's resolution. Perlin noise is created by summing several octaves of coherent noise, each subsequent octave having

increased frequency and reduced amplitude. Frequency is the frequency of the initial octave, lacunarity is the frequency multiplier between each octave, and persistence is the amplitude decrease factor between each octave. For the Dimorphos model, the values in Table 3.4 are used.

Parameter	Values
Number of octaves	10
Frequency	3000
Lacunarity	2
Persistence	0.1
Scale	1

Table 3.4: Perlin Noise Specifications

The ESA/Planet and Asteroid Natural Scene Generation Utility (PANGU) environment simulator [112] is used for the following steps. Surface feature addition consists of iteratively adding boulders to the surface according to the precise rock distribution law provided by the Hera reference model. According to Hera's science team, rocks and boulders are added as in [110]. The differential size frequency distribution of surface rocks is assumed to follow a power law described by:

$$dN = KD^q dD \tag{3.1}$$

Where dN is the number of boulders per unit area in the diameter range from D to $D + dD$ and where $q = -(K/c + 1)$, the model parameter are described in the Table 3.5.

Parameter	Values
Diameter	0.164 km
Lower Cutoff Rock Diameter	6.4 cm
Upper Cutoff Diameter	5 m
c	$0.121/m^2$
K	$0.30\ 1/m^2$

Table 3.5: Surface Modelling

Finally, surface albedo is matched with available optical observation and estimated albedo. In Figure 3.4, a comparison is shown between the modeled high-fidelity surface and the 67P/Churyumov–Gerasimenko comet surface.

The PANGU software also provides for each RGB image the corresponding masked boulder image, which is precisely the labeled data on which the neural networks are trained as presented in Section 4.5.1.

3.4 Relative State Estimation

This section aims to provide a comprehensive definition of relative state estimation, explicitly focusing on the dynamics equations involved in the estimation process. The term relative, as opposed

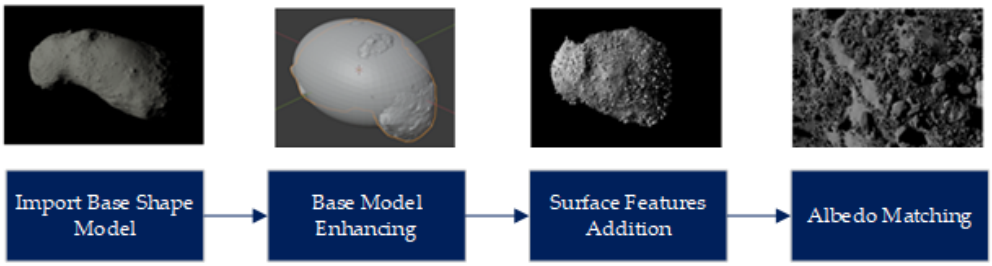

Figure 3.3: Asteroid Modelling Pipeline

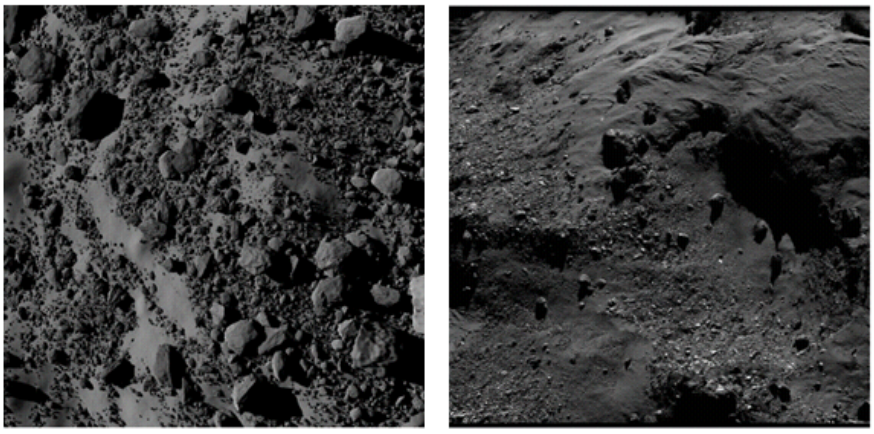

Figure 3.4: Synthetic surface detail(left) and 67P/CG Comet surface (right).

to absolute, defines a state generally described with reference to a non-inertial reference frame (i.e., L-frame). The relations between the L-frame and the I-frame are derived given the final knowledge of the High Altitude Phase Navigation (HAPNAV).

3.4.1 Translational Dynamics

The dynamics are written in the L-frame (defined in Appendix A) as in Eq. 3.2; in Figure 3.5 a sketch of the reference frame definition is illustrated.

$$\ddot{\mathbf{r}}_L^{LB} + 2\boldsymbol{\omega}_L^{IS} \times \dot{\mathbf{r}}_L^{LB} + \boldsymbol{\omega}_L^{IS} \times [\boldsymbol{\omega}_S^{IS} \times (R_{LS}\mathbf{r}_S^{LS} + \mathbf{r}_L^{LB})] = \mathbf{u}_L + \mathbf{g}_L + \mathbf{d}_L \tag{3.2}$$

where $\mathbf{r}_L^{LB}$ is the lander position in the relative body-fixed frame, $\boldsymbol{\omega}_S^{IS}$ is the angular velocity of the secondary body with respect to the primary, $\mathbf{u}_L$, $\mathbf{g}_L$, $\mathbf{d}_L$ are respectively the control acceleration, the gravitational acceleration (i.e., primary and secondary acceleration) and any external modeled disturbances.

3.4.2 Attitude Dynamics

For the attitude dynamics, the same consideration presented in Section D.2.2 are valid for the rotational dynamics. In particular, it is chosen to develop a 3 DoF implementation focused on translational navigation. The attitude problem already has well-grounded state-of-the-art solutions with proven efficacy, and for the NEO-MAPP activity, attitude is assumed to be perfectly known.

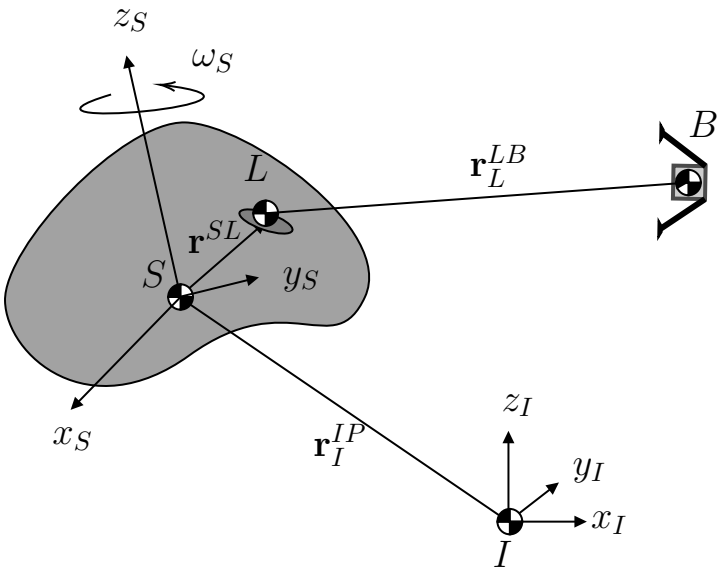

Figure 3.5: Relative navigation reference frame sketch

3.5 Sensors and Measurement Models

The same HAP sensor suite is also used for the LAP. However, the sensors provide different measurements and are fused using different approaches compared to HAPNAV.

3.5.1 Accelerometer

Exact derivation and specification of Section D.3.1 are valid.

3.5.2 Camera

The navigation camera represents the primary sensor for the Low Altitude Phase Navigation (LAPNAV). The RGB image is processed by extracting and tracking the features in the navigation filter. Relative feature-based navigation filters rely on images captured by cameras to determine the spacecraft's relative position and orientation with respect to a celestial body.

The camera takes images of the asteroid's surface and identifies salient features such as craters, boulders, and ridges that can be easily distinguished. These features act as reference points and can be tracked to estimate the spacecraft's position and orientation by comparing them to previous instances; the aim is to reduce the drift of the solution compared to the inertial frame.

The feature-based navigation back-end uses the EKF to estimate the position and orientation of the spacecraft. This algorithm considers the noise and uncertainties associated with the measurements obtained from the camera and other sensors on board the spacecraft, such as accelerometers.

The 3D points on the surface tracked in the filter are defined *landmark*s, while their 2D projection on the sensor are *feature*s.

Camera Characteristics

Table B.4 shows the camera's characteristics. Since a high-fidelity scene is needed to assess representative mission performance, a high-resolution model of the landing area is rendered. Due to

hardware limitations, a completely high-fidelity asteroid would excessively slow down the development and testing process. The 3D models and modeling steps are the same as Appendix 3.3. Still, only a cut-out of approximately 50 m around the landing zone is rendered for faster generation performances; see Figure 3.13. The inputs for PANGU are defined in Section D.3.2.

Camera Model

Similar to the previous chapter, a camera model extracts spatial information from the images. Landmarks are projected into features using the pinhole camera model. The pinhole camera model [113] is used to calculate the pixel coordinates associated with the projection of the i-th landmark defined in B-frame:

$$\begin{pmatrix} u_i \\ v_i \end{pmatrix} = \frac{f}{h_{px} z_B^{Bi}} \begin{pmatrix} x_B^{Bi} \\ y_B^{Bi} \end{pmatrix} \tag{3.3}$$

In figure 3.6, 38 landmarks are projected on the image sensor.

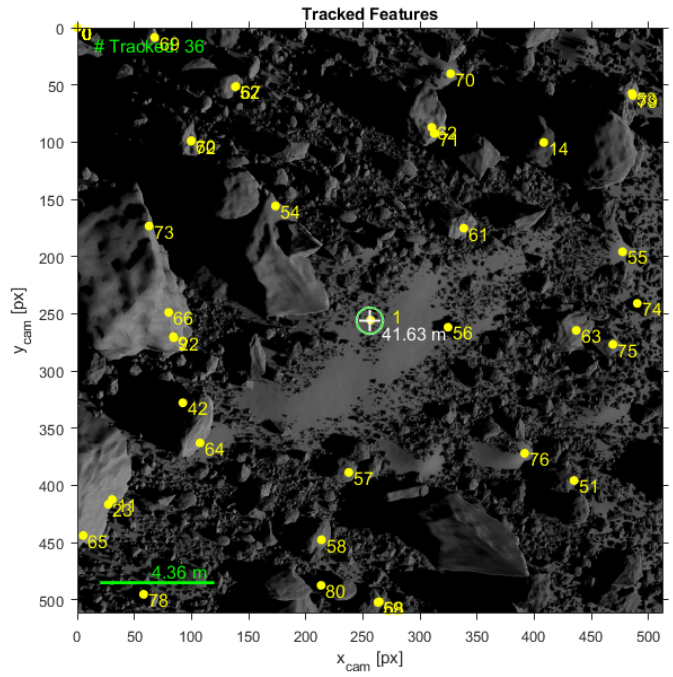

Figure 3.6: Landmarks projected into features on a sample image, the white cross is the LRF measurement

3.5.3 Laser Range Finder

The LRF points in the same direction as the camera, the z-axis of B-frame, and provides a distance measurement to landmark linked to the current target landing site or any hit landmark. The current target landing site tracking is kept by attitude guidance using visual information. When the filter is initialized, a feature is forced on the sensor origin (i.e., initial target landing site), and the attitude guidance and control keep this feature centered in the frame.

If the target landing site pointing is lost, the LRF measurement is linked to the landmark hit by the beam within a fixed threshold. The measurement is invalid if no landmark is hit, as in Figure

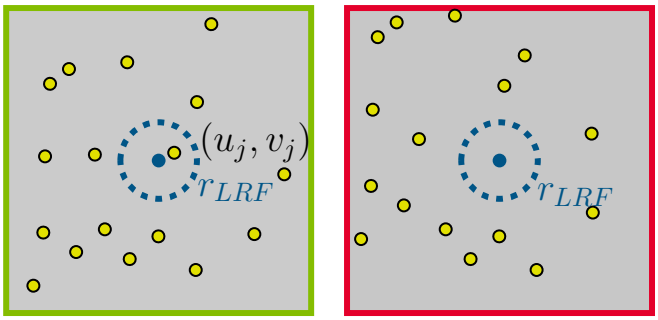

Figure 3.7: LRF measurement association: valid (left) and invalid (right) measurement

3.7. The distance r_{LRF} measured by the LRF between the spacecraft and a landmark j on the surface of the secondary asteroid is sketched in Figure 3.8 and is expressed as:

$$\tilde{r}_{LRF} = \tilde{r}_B^{Bj} = |\mathbf{r}_L^{Lj} - \mathbf{r}_L^{LB}| \tag{3.4}$$

The measurement is obtained using PANGU and uses the 3D model of the landing site area.

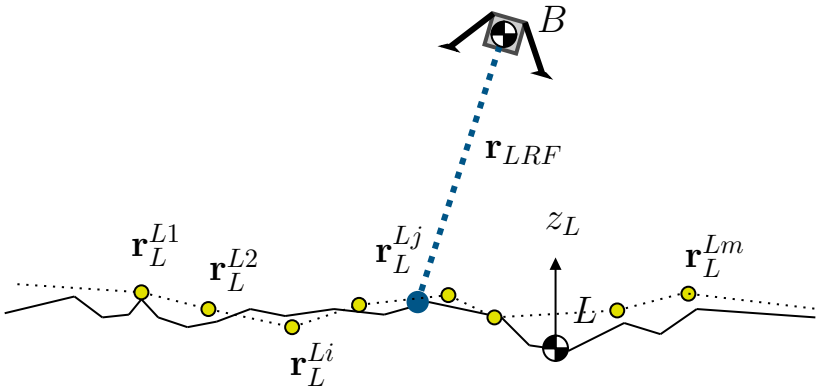

Figure 3.8: LRF measurement (blue) in LAP and estimated landmarks (yellow)

3.6 Image Processing

The image processing front-end of the LAPNAV filter uses Japanese for "wind" (KAZE) [114] as a feature detector and Kanade Lucas Tomasi Tracker (KLT) for feature tracking [115, 116] as shown in Figure 3.9; it includes the steps presented in Algorithm 1.

A total of 50 features is tracked; however, when the number of the tracked features goes below 20 (i.e., they are lost from the Field of View (FOV)), new features are detected, their relative landmark initialized and added to the filter state.

3.6.1 Feature Extractor

A feature extractor is a computer vision algorithm that detects and extracts distinctive features from an image [117], which can be used to track objects over time. In a tracking Kalman filter, a feature extractor is typically used in the front end of the filter to extract features to track. The KAZE algorithm is proven to have stable and accurate performance on asteroid and comet scenarios [118],

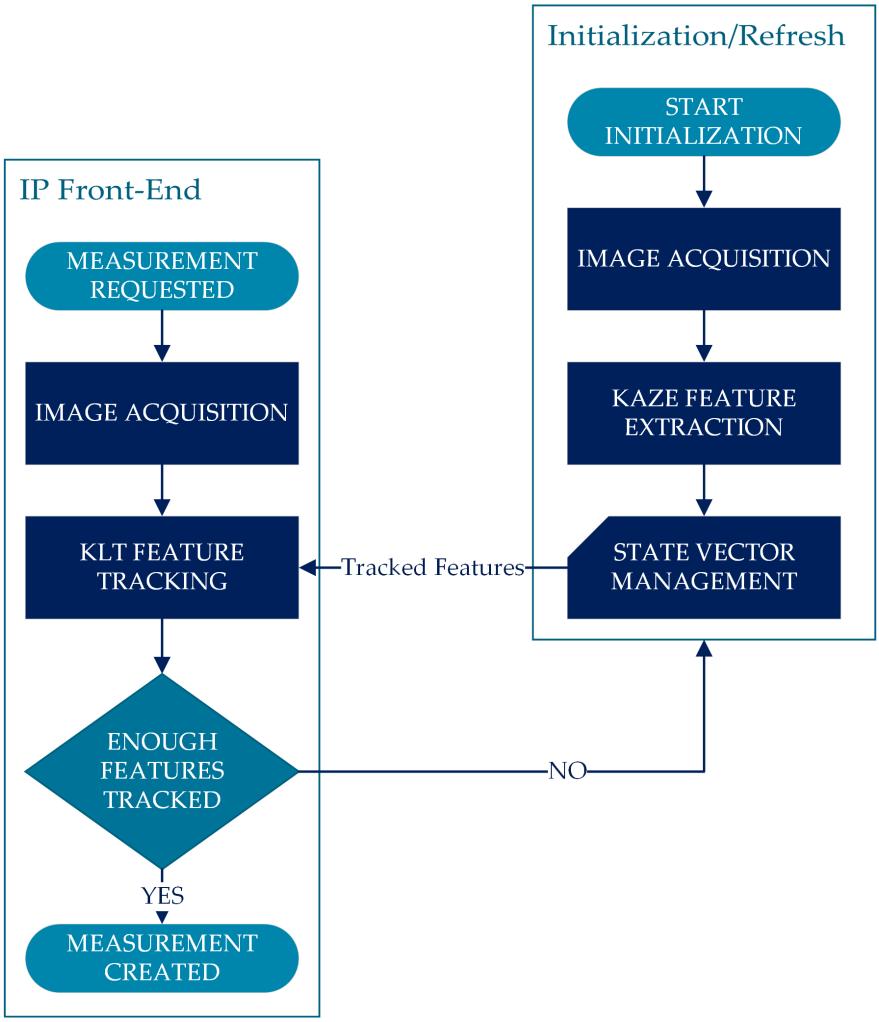

Figure 3.9: Image processing front-end flow chart

Algorithm 1 LAPNAV Image Processing Algorithm

1: Image acquisition. ▷ The first step is acquiring the camera's images.
2: Preprocessing. ▷ The acquired images are typically preprocessed to remove noise and enhance the features. This step includes distortion removal, given the calibration parameters of the camera.
3: Feature detection. ▷ KAZE is used as a feature detector. KAZE is a scale and rotation invariant feature detector that can detect keypoints with high repeatability and robustness to image noise and blur. Features are detected and extracted; particularly, the feature associated with the LRF measurement is detected.
4: Feature tracking. ▷ Once the features are detected in the current frame, the KLT algorithm is used to track the features across subsequent frames. KLT tracks the features by estimating the optical flow between the frames. Each feature is identified by an ID allowing the filter to track every measured landmark.

and it is chosen for initiating the extraction process in the navigation filter. KAZE (or "Accelerated-KAZE") is a feature extractor algorithm commonly used in computer vision applications such as object detection [114], image registration, and 3D reconstruction. Here are some characteristics of the KAZE feature extractor:

- Scale and rotation invariance: The KAZE algorithm is designed to be invariant to scale and rotation, meaning it can detect the same features regardless of their size or orientation in the image.
- Non-linear scale space: KAZE uses a non-linear scale space representation of the image, allowing it to capture more complex structures than linear scale spaces such as Gaussian pyramids.
- Non-maximum suppression: KAZE applies non-maximum suppression to the detected key points to remove redundant keypoints close to each other.
- Gradient-based feature extraction: KAZE computes feature descriptors based on the gradient orientation and magnitude of the image at each keypoint, similar to other feature extractors such as SIFT and SURF [117].
- Fast computation: KAZE is designed to be computationally efficient, making it suitable for real-time applications such as video tracking and augmented reality.
- Robustness to image noise and blur: KAZE is designed to be robust to image noise and blur, which can be challenging for other feature extractors that rely on precise image gradients.

Overall, the KAZE feature extractor is a powerful tool for detecting and describing image keypoints, with desirable characteristics such as scale and rotation invariance, fast computation, and robustness to image noise and blur. Figure 3.6 shows an example of KAZE-extracted features.

3.6.2 Feature Tracking and Matching Analysis

Two main approaches can be used in the front end after the features are extracted, feature tracking and feature matching. A comparison is presented in Table 3.6.

Feature matching is a one-time process used to find correspondences in two or more images; feature tracking is a continuous process used to track the movement of features over time. In the matching, features are extracted independently from each image and then matched by comparing their descriptors. In the tracking, the features are extracted from the first image and then tracked in subsequent frames [119].

Criteria	Feature Matching	Feature Tracking
Number of features	Vary significantly between frames	Same over multiple frames
Initialization	Detect new features in each frame	Track previously detected features
Matching step	Computationally expensive	Faster and less computationally expensive

Outliers	False matches and mismatches	Use RANSAC to remove them
Accuracy	when many features are available	Effective when few features are available
Implementation	Slower, more computational effort	Faster, less computational effort
Re-initialization	Frequent, relatively short-term tracking	Track features for extended periods

Table 3.6: Comparison feature matching and tracking

Feature matching can be more accurate when many features are available but can suffer from false matches and mismatches and requires detecting new features in each frame. Feature tracking is faster, requires less computational effort, and can track the same features over multiple frames. However, it may be less effective when few features are available and can still suffer from mismatches and require outlier removal.

One of the critical advantages of feature tracking is its speed and efficiency. Compared to feature matching, feature tracking requires less computational effort and can be implemented faster, making it a more practical choice for real-time applications. Additionally, feature tracking can track the same features over multiple frames, allowing longer-term tracking and reducing the need for repeated feature detection and matching. This can help to improve the accuracy and reliability of navigation filters and other computer vision applications, especially in situations where features may be difficult to detect or where motion is complex or unpredictable. Overall, the speed, efficiency, and longer-term tracking capabilities of feature tracking make it a valuable tool for many different types of computer vision applications.

Figure 3.10 it is shown how feature tracking (KLT) has higher performance compared to feature matching (KAZE): the number of tracked features decreases at a lower rate in the tracking. It allows less filter refresh, in addition to the advantages mentioned above.

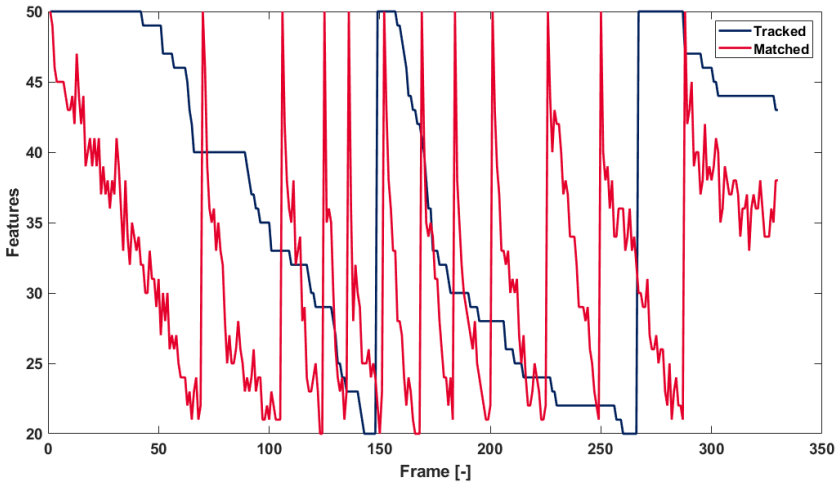

Figure 3.10: Comparison of feature tracking versus feature matching

3.6.3 KLT Tracking and Performances

KLT tracking is a computer vision technique used to track and estimate the motion of objects in a video sequence. The algorithm uses feature points in the image to track the object's motion. KLT tracking is beneficial in high motion or occlusion scenarios [115, 120].

The KLT tracking algorithm first identifies a set of feature points in an initial frame using a feature extraction algorithm, in this case KAZE [114]. The algorithm then tracks the motion of these feature points in subsequent frames using the Lucas-Kanade algorithm, which estimates the optical flow between two consecutive frames. The Lucas-Kanade algorithm assumes that the intensity of a pixel in an image does not change significantly between frames. Hence, the motion of a pixel can be estimated by minimizing the error between the intensities of the pixel in the first frame and its corresponding pixel in the second frame. The algorithm models the motion of the feature point as a translation in x and y directions and then uses a linear least squares method to estimate the motion parameters.

Once the motion parameters are estimated, the feature point is projected onto the next frame using the estimated motion parameters, and the process is repeated for the next frame. The KLT tracking algorithm can track multiple feature points simultaneously, and it is computationally efficient, making it suitable for real-time applications.

To assess the performance of the KLT algorithm, a method is defined to evaluate the performance of KLT tracking by comparing the projection of the true features with the tracked features. The steps are presented in the Algorithm 2.

Algorithm 2 KLT Performance Evaluator Algorithm

1: Extract feature points (u, v) from the image at time t_0 using KAZE. These features are used as reference points for tracking.
2: For each feature, extract the corresponding 3D landmark: the landmark linked to each feature is extracted using PANGU. These 3D locations are considered true landmarks and are fixed in L-frame.
3: Propagate pose (translation and attitude) at t_1
4: The feature points extracted at t_0 are tracked in the image at t_1 using the KLT algorithm. The resulting tracked feature points are called *tracked features*.
5: The true landmarks extracted at t_0 are projected to the image at t_1 using the real pose of the camera. The resulting projected feature points are called *true features*.
6: Evaluate error between *true features* and *tracked features*

The algorithm aims to estimate and understand if the noise in the tracking system is Gaussian. By evaluating the error between the true features and tracked features using various metrics, I can determine the characteristics of the noise in the system. If the noise is Gaussian, the error distribution will be normal, and the error signal will have a flat frequency content. In Figure 3.11a, the drift along (u, v) directions are presented for all the features during a sample landing: as known in the literature [121], the process is not Gaussian but has a drift over time. The mean features drift, presented with the bold line, is 0, but in this specific landing simulation, the u axis has an increased drift, probably depending on the principal direction of motion. In Figure 3.11b, a randomly selected feature drift is shown; it is noted that a 1 px drift is accumulated in 500 seconds simulation. By observing the magnitude of the drift in Figure 3.11c, it is clear that some features have higher drift than others, probably depending on the KLT performance in some specific surface texture.

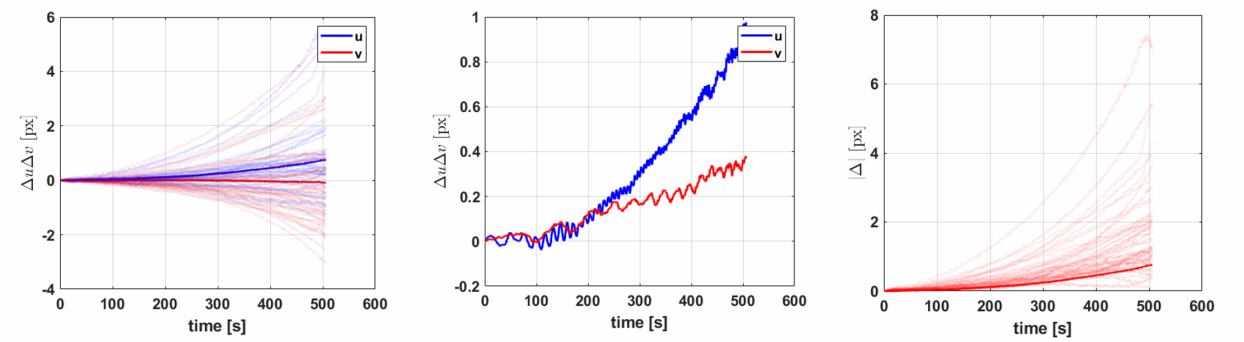

(a) Features drift over time **(b)** Sample feature drift **(c)** Drift magnitude

Figure 3.11: KLT tracking performances

This behavior is modeled in the filter using an adaptive covariance in the measurement covariance matrix, as presented in Equation 3.20.

The measurement provided by the image processing front-end is composed of the tracked ID number and the current features coordinate as:

$$\mathbf{f}_i = \begin{pmatrix} ID_i & u_i & v_i \end{pmatrix} \tag{3.5}$$

Figure 3.12 presents tracked features over time. The minimum and maximum number of tracked features can be easily identified. Also, the refresh procedure is well-defined. At the beginning of the trajectory, no feature decrease is observed because all the features are detected on a small central portion of the image, as shown in Figure 3.13, and some time must occur before they are lost from the field of view. At the end of the trajectory, the features refresh gets more frequent because the parallax effect is more significant at a lower altitude, and then the features are lost at a higher rate.

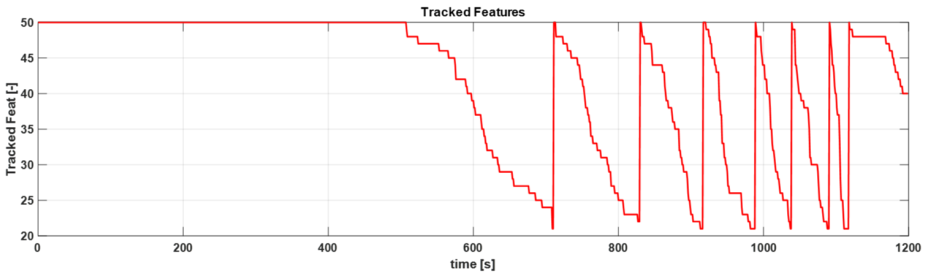

Figure 3.12: KLT tracking performances: tracked features over time for a sample trajectory

3.7 Navigation Filter Development

This section presents the navigation concept that is implemented using an EKF, the EKF state vector, and the propagation and measurement update steps of the EKF. Directly following the EKF development is a description of the reference landing trajectory, the initial setup and tuning of the EKF.

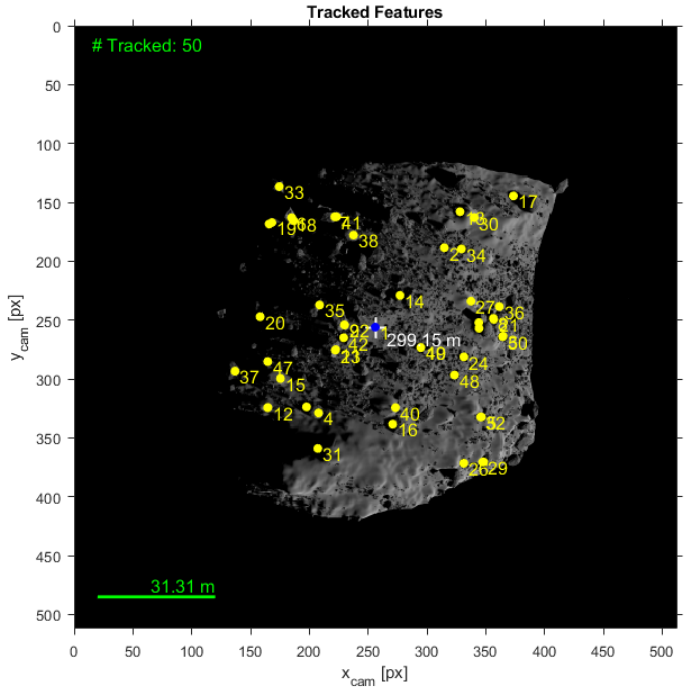

Figure 3.13: Image processing preview: in yellow tracked features in red true features, in blue LRF beam and measurement

3.7.1 Navigation Concept

The navigation concept estimates the relative position with reference to the lander's surface. Since no absolute information is measured, only the relative state can be measured, and the drift of that knowledge shall be limited over time. On-board measurements keep the estimation drift bounded and allow to estimate precisely the relative state. Camera images provide tracked features while the LRF improves the observability along the LOS axis, as introduced in Section 3.2.4. Both the accelerometer and the LRF resolve the scale ambiguity of using only a monocular camera. No prior knowledge of the environment is used except for the initial inertial condition and camera pose.

3.7.2 State Definition

The camera and LRF measurements are relative to the observed features, i.e., surface features. The camera tracks up to 50 features/landmarks from the surface and at least 20 features/landmarks. Defining the state vector in the L-frame is favorable because measurements are directly provided in this relative frame. The state vector, therefore, consists of the position and velocity of the spacecraft in the L-frame, respectively $\mathbf{r}_L^{LB}$, $\dot{\mathbf{r}}_L^{LB}$ and the accelerometer random walk $\mathbf{b}_a$ in B-frame; all the current tracked landmarks $\mathbf{r}_L^{Li}$ are included in the state vector. The velocity random walk is also called the accelerometer bias. The state vector is thus as follows:

$$\mathbf{x} = \begin{pmatrix} \mathbf{x}_{dyn} & \mathbf{x}_{map} \end{pmatrix}^T = \begin{pmatrix} \mathbf{r}_L^{LB} & \dot{\mathbf{r}}_L^{LB} & \mathbf{b}_a & \mathbf{r}_L^{Li} \end{pmatrix}^T \tag{3.6}$$

$$\mathbf{x}_{dyn} = \begin{pmatrix} \mathbf{r}_L^{LB} & \dot{\mathbf{r}}_L^{LB} & \mathbf{b}_a \end{pmatrix}^T \tag{3.7}$$

$$\mathbf{x}_{map} = \left(\mathbf{r}_L^{Li}\right)^T \tag{3.8}$$

With $i = 1, \ldots, m$, and m is the number of current tracked features.

At each time step, the tracked landmarks are managed by removing the lost ones and adding the newly detected ones; in fact, the map part of the state $\mathbf{x}_{map}$ is dynamically changing over time.

3.7.3 State Propagation

The six DoF dynamics equations in L-frame are given by:

$$\begin{cases} \dot{\mathbf{r}} = \dot{\mathbf{r}}_L^{LB} \\ \ddot{\mathbf{r}} = R_{BL}^T\left(\ \mathbf{q}_{LB}\right)\left(\tilde{\mathbf{a}}_B - \mathbf{b}_a\right) - 2\boldsymbol{\omega}_L^{IS} \times \dot{\mathbf{r}}_L^{LB} - \boldsymbol{\omega}_L^{IS} \times \left[\boldsymbol{\omega}_L^{IS} \times \left(R_{LS}\mathbf{r}_S^{SL} + \mathbf{r}_L^{LB}\right)\right] + \\ \mathbf{g}_L - R_{BL}^T\left(\mathbf{q}_{LB}\right)\boldsymbol{\eta}_a \\ \dot{\mathbf{b}}_a = \boldsymbol{\eta}_{ba} \\ \dot{\mathbf{q}}_{LB} = \frac{1}{2}\left[\tilde{\boldsymbol{\omega}}_B - \mathbf{b}_g - R_{BL}\left(\mathbf{q}_{LB}\right)\boldsymbol{\omega}_L^{IS} - \boldsymbol{\eta}_g\right] \otimes \mathbf{q}_{LB} \\ \dot{\mathbf{b}}_g = \boldsymbol{\eta}_{bg} \end{cases} \tag{3.9}$$

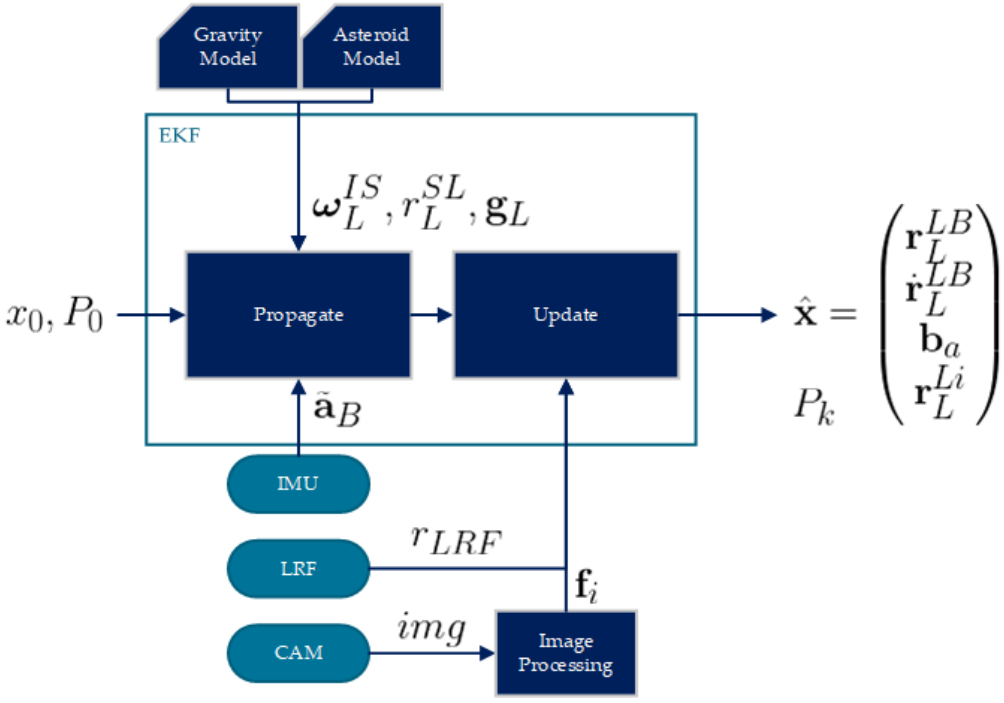

Figure 3.14: Relative navigation architecture sketch

As explained in Section 3.4.2, only the 3 DoF dynamic is developed. The actual relative acceleration of the spacecraft is unknown. Therefore, the measured acceleration, corrected for bias, is used in the filter in the dynamic-model replacement form [122]. The uncertainty in this measurement is included in the propagation equation through the G matrix and the input noise vector. A Look Up Table (LUT)-based polyhedron model is used as input for the gravity model $\mathbf{g}_L = \mathbf{g}_L(\mathbf{r}_L^{LB})$; the polyhedron model is updated with the most recent environment knowledge. The nonlinear

propagation equation is as follows:

$$\dot{\mathbf{x}}_{dyn} = f_{dyn}\left(\mathbf{x},\mathbf{u}\right) + G\boldsymbol{\omega} = \begin{pmatrix} \mathbf{v}_L^{LB} \\ \ddot{\mathbf{r}}_L^{LB} \\ \dot{\mathbf{b}}_a \end{pmatrix} + G\begin{pmatrix} \boldsymbol{\eta}_a \\ \boldsymbol{\eta}_{ba} \end{pmatrix} =$$
$$= \begin{pmatrix} \dot{\mathbf{r}}_L^{LB} \\ \mathbf{g}_L + R_{LB}\left(\tilde{\mathbf{a}}_B - \mathbf{b}_a\right) - 2\boldsymbol{\omega}_{IS} \times \mathbf{v}_L^{LB} - \boldsymbol{\omega}_{IS} \times \boldsymbol{\omega}_{IS}\left(R_{LS}\mathbf{r}_S^{SL} + \mathbf{r}_L^{LB}\right) \\ \mathbf{0}_{3\times 1} \end{pmatrix} + \tag{3.10}$$
$$+ \begin{bmatrix} \mathbf{0}_{3\times 3} & \mathbf{0}_{3\times 3} \\ -R_{IB} & \mathbf{0}_{3\times 3} \\ \mathbf{0}_{3\times 3} & \mathbf{I}_{3\times 3} \end{bmatrix} \begin{pmatrix} \boldsymbol{\eta}_a \\ \boldsymbol{\eta}_{ba} \end{pmatrix}$$

The acceleration equation contains the centripetal and Coriolis terms linked to the non-inertial L-frame system: $\mathbf{r}_S^{SL}$ represents the coordinate of the landing site in the S-frame, $\boldsymbol{\omega}_{IS}$ is the angular rate of the secondary to the primary in the L-frame. Since all the landmarks are static in the L-frame, their propagation equation is trivial.

$$\dot{\mathbf{x}}_{map} = \mathbf{0}_{3m\times 1} \tag{3.11}$$

The Jacobian of the state derivative is used to propagate the covariance matrix P of the EKF. The $\nabla\mathbf{g}_L$is the gravity gradient calculated using a binary point mass assumption. For the dynamic part of the state, the following is obtained:

$$F_{x,dyn} = \frac{\partial f_{dyn}(\mathbf{x},\mathbf{u})}{\partial \mathbf{x}_{dyn}} = \begin{bmatrix} \mathbf{0}_{3\times 3} & \mathbf{I}_{3\times 3} & \mathbf{0}_{3\times 3} \\ [\boldsymbol{\omega}_{IS}]_\times[\boldsymbol{\omega}_{IS}]_\times + \nabla\mathbf{g}_L & -2[\boldsymbol{\omega}_{IS}]_\times & -R_{BL,3\times 3} \\ \mathbf{0}_{3\times 3} & \mathbf{0}_{3\times 3} & \mathbf{0}_{3\times 3} \end{bmatrix} \tag{3.12}$$

where

$$\nabla\mathbf{g}_L = \nabla\mathbf{g}_L^P + \nabla\mathbf{g}_L^S = -\mu_P R_{LS} R_{SP} J_P\left(R_{SL}R_{SP}\right)^T - \mu_S R_{SL} J_S R_{SL}^T \tag{3.13}$$

with

$$J_{P/S}\left(\mathbf{r}_{P/S}^{PB/SB}\right) = \frac{1}{|r|^5}\begin{bmatrix} -2x_1^2 + x_2^2 + x_3^2 & -3x_1x_2 & -3x_1x_3 & \\ -3x_1x_2 & x_1^2 - 2x_2^2 + x_3^2 & -3x_2x_3 & \\ -3x_1x_3 & -3x_2x_3 & x_1x_2 & x_1^2 + x_2^2 - 2x_3^2 \end{bmatrix} \tag{3.14}$$

The gravitational parameters are $\mu_{P/S} = Gm_{P/S}$, where $_{P/S}$ subscripts are used respectively for the primary and secondary body. For the map section of the state, the Jacobian is $\mathbf{F}_{x_{map}} = \mathbf{I}_{3m\times 3m}$ Finally, the process noise covariance matrix Q is created using the accelerometer noise and bias covariances:

$$Q = \begin{bmatrix} \sigma_a^2\mathbf{I}_{3\times 3} & \mathbf{0}_{3\times 3} \\ \mathbf{0}_{3\times 3} & \sigma_{ba}^2\mathbf{I}_{3\times 3} \end{bmatrix} \tag{3.15}$$

3.7.4 State Update

The state update step includes the Kalman gain calculation, the measurement update itself, and the covariance matrix P update. An essential part of these calculations is the function $\mathbf{z} = h(\mathbf{x}, \mathbf{u})$, which calculates the measurement that is expected given the current best estimate for the filter state $\mathbf{x}$. The Jacobian of $h(\mathbf{x}, \mathbf{u})$, called H_x, is used in the Kalman gain calculation and the covariance matrix update. The measurements that must be calculated are the expected feature locations on the sensor and the expected distance to the hit landmark measured by the LRF.

The measurement updates are performed separately from one another. Details on the measurement update for the camera and the LRF are given below.

Camera Measurement

The image processing calculates which features are tracked and which are lost for every image the camera outputs and sorts the state accordingly. The landmark-feature data association is done at this stage, thanks to the feature ID provided by the front end. If some feature is lost, no measurement update happens for that particular feature. The size of the measurement update varies between the minimum and the maximum number of tracked features. In the following, the generic update for the i-th feature is presented.

The image processing outputs $\tilde{\mathbf{f}}_i = \begin{bmatrix} ID_i & u_i & v_i \end{bmatrix}$, its measurement for feature location in the sensor frame and the ID connected to the specific landmark.

To calculate the expected value for this measurement using $z = h(\mathbf{x}, \mathbf{u})$, the knowledge of the mapping between the i-th feature and the i-th landmark (ID) is used. The measured feature is connected to its specific landmark. This landmark point must now be projected onto the camera sensor. First, it must be transformed into the B-frame. This is done as follows:

$$\mathbf{r}_B^{Bi} = R_{BL} \left(\mathbf{r}_L^{Li} - \mathbf{r}_L^{LB} \right) \tag{3.16}$$

where the attitude navigation gives R_{BL} and, as mentioned, assumed known. The next step is to use the pinhole camera model to calculate the corresponding pixel coordinates of $\mathbf{r}_B^{Bi}$. The coordinates are shifted by 256 pixels to transform them to the image coordinate system because the image coordinate system $(0, 0)$ is at the image border, while the pinhole model is at the center of the image. The resulting equation is:

$$\mathbf{z} = h(x, u) = \hat{\mathbf{f}}_i = \frac{f}{h_{px} z_B^{Bi}} \begin{pmatrix} x_B^{Bi} \\ y_B^{Bi} \end{pmatrix} + \begin{pmatrix} 256 \\ 256 \end{pmatrix} \tag{3.17}$$

where h_{px} is the pixel metric width. Now to find H_x, the Jacobian of $h(\mathbf{x}, \mathbf{u})$ is calculated:

$$H_x = \frac{\partial h(\mathbf{x}, \mathbf{u})}{\partial \mathbf{x}} = \begin{bmatrix} -R_{BL}J & 0_{2\times 6} & \dots & R_{BL}J & \dots \end{bmatrix} \tag{3.18}$$

Where J is:

$$\frac{\partial h(\mathbf{x}, \mathbf{u})}{\partial \mathbf{r}_B^{Bi}} = \frac{f}{z_B^{BP} h_{px}} \begin{bmatrix} 1 & 0 & -\dfrac{x_B^{BP}}{z_B^{BP}} \\ 0 & 1 & -\dfrac{y_B^{BP}}{z_B^{BP}} \end{bmatrix} \tag{3.19}$$

The covariance matrix for the feature measurement uses an adaptive expression; as the feature is observed for a longer time, its drift increases. Features initialized for longer times should have higher covariance, as shown in Figure 3.11a. The adaptive covariance is given by:

$$\sigma_{cam} = 2 + 0.05 \cdot t_{k,refresh} \ [px] \tag{3.20}$$

Where $t_{refresh}$ counts the step from initialization, this equation empirically represents the conclusion driven in Section 3.6. The camera covariance has an initial value of 2 px, and at each time step increases of 0.05 px, these values have been empirically derived.

Laser Range Finder Measurement

The LRF update is only performed if a valid LRF measurement is obtained from PANGU and if one of the following conditions is verified:

- The current target landing site is hit by the LRF beam within a certain tolerance.
- Any tracked landmark is hit by the LRF beam within a certain tolerance.

From a practical point of view, the target landing site is treated as any other landmark. However, the two concepts are separated for increased clarity. See Figure 3.7 for an example of valid or invalid measurement.

The sensor model projection equation calculates the j-th expected LRF measurement from the filter state. The main challenge here is the data association between LRF beam and j-th landmark. This approach uses no shape model, and only when the laser beam collides with the j-th tracked landmark, the measurement is valid.

The Jacobian is calculated from Eq. 3.4 as follows:

$$H_x = \frac{\partial h(\mathbf{x},\mathbf{u})}{\partial \mathbf{x}} = \begin{bmatrix} \frac{\partial h(\mathbf{x},\mathbf{u})}{\partial \mathbf{r}_L^{LB}} & \mathbf{0}_{1\times 3} & \mathbf{0}_{1\times 3} & \dots & \frac{\partial h(\mathbf{x},\mathbf{u})}{\partial \mathbf{r}_L^{Lj}} & \dots \end{bmatrix} \tag{3.21}$$

Now the chain rule is applied:

$$\frac{\partial h(\mathbf{x},\mathbf{u})}{\partial \mathbf{r}_L^{LB}} = \frac{\partial h(\mathbf{x},\mathbf{u})}{\partial \mathbf{r}_B^{Bj}} \frac{\partial \mathbf{r}_B^{Bj}}{\partial \mathbf{r}_L^{LB}} = -\frac{\partial h(\mathbf{x},\mathbf{u})}{\partial \mathbf{r}_B^{Bj}} \mathbf{I}_{3\times 3} \tag{3.22}$$

$$\frac{\partial h(\mathbf{x},\mathbf{u})}{\partial \mathbf{r}_L^{Lj}} = \frac{\partial h(\mathbf{x},\mathbf{u})}{\partial \mathbf{r}_B^{Bj}} \frac{\partial \mathbf{r}_B^{Bj}}{\partial \mathbf{r}_L^{Lj}} = -\frac{\partial h(\mathbf{x},\mathbf{u})}{\partial \mathbf{r}_B^{Bj}} \mathbf{I}_{3\times 3} \tag{3.23}$$

The remaining partial derivative to complete the Jacobian is given by:

$$\frac{\partial h(\mathbf{x},\mathbf{u})}{\partial \mathbf{r}_B^{Bj}} = \frac{\partial |\mathbf{r}_L^{Lj} - \mathbf{r}_I^{LB}|}{\partial \mathbf{r}_B^{Bj}} = \frac{\mathbf{r}_L^{Lj} - \mathbf{r}_I^{LB}}{|\mathbf{r}_L^{Lj} - \mathbf{r}_I^{LB}|} \tag{3.24}$$

Landmarks Initialization / Refresh

There are many possible approaches to initialize the landmarks in the filter state; the most commonly used are to define landmarks in an inverse depth parametrization [123] where landmarks are

initialized at infinite while being observed if enough parallax is achieved, they converge to the true 3D state.

However, a less complex approach is used in the current implementation. The landmarks are parametrized in Cartesian form as follows:

$$\mathbf{r}_L^{Li} = \begin{bmatrix} x_L^{Li} \\ y_L^{Li} \\ z_L^{Li} \end{bmatrix} \tag{3.25}$$

Once the filter is initialized, the landmarks are located on a plane orthogonal to the LOS (estimated using the attitude determination) and located at the LRF measurement, it is assumed a planar surface, and as a consequence, all the features are projected on that plane.

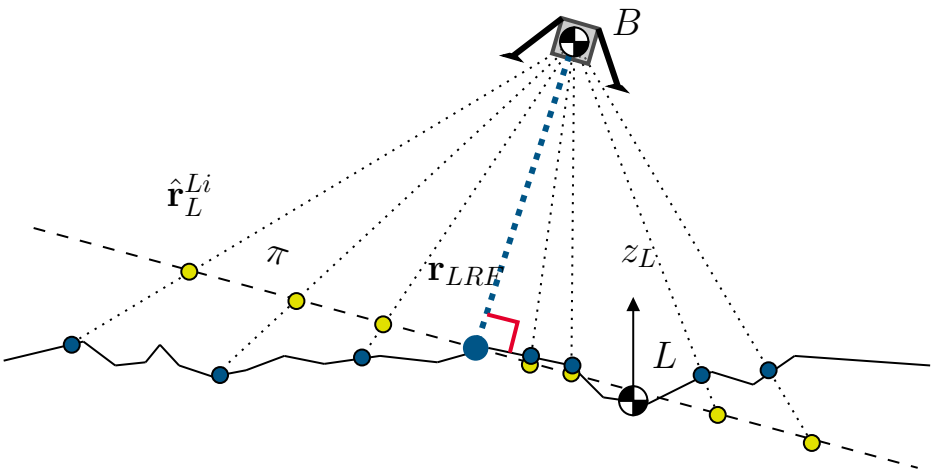

Figure 3.15: Landmarks initialization/refresh: predicted landmarks locations (yellow) on π (LRF plane) and true landmarks (blue).

The former assumption provides a more significant error once the filter is initialized, i.e., far from the surface, however as the surface is approached, the surface curvature decreases and increases the validity of the assumption; as the lander approaches the surface, the initialization error linked to curvature decreases. Also, as the landing is mostly nadir, the LOS direction tends to be parallel to the plane normal, minimizing the error of the assumption.

The same algorithm is used to refresh lost landmarks. Once a state refresh is triggered, the number of tracked features goes below a predefined threshold, new features are detected, and their corresponding landmarks are initialized on a plane orthogonal to the LRF measurement.

This simplified initialization/refresh algorithm has proven stable and robust initialization even in cases with high curvature shape models, i.e., the current Itokawa reshaped model (see Section 3.3.1).

3.7.5 Reference Landing Trajectory

The nominal flight time is 30 minutes, and the starting position is 300 m above the surface at the *home* position, i.e., above the outward-facing pole of the secondary (as defined in Section 2). A sample trajectory is shown in Figure 3.16 with position knowledge error. A set of reference trajectories of the spacecraft is shown in Figure 3.17; this set will be discussed as part of the Monte

Carlo reference landing scenario.

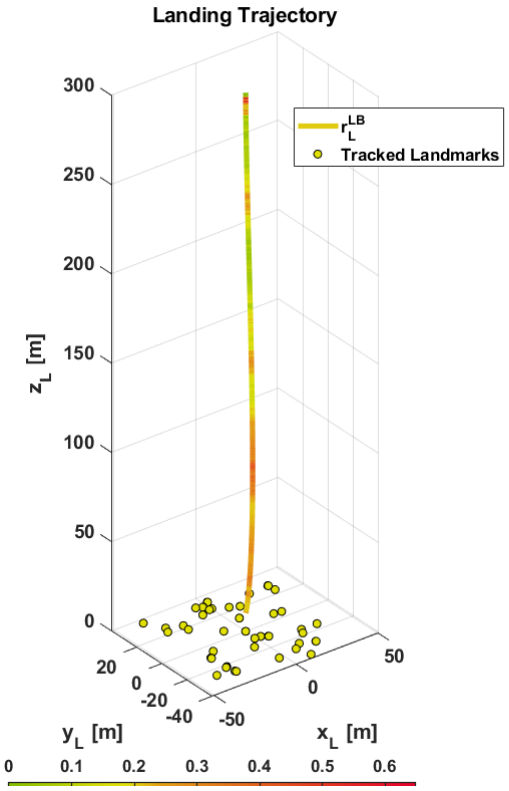

Figure 3.16: Sample landing trajectory: PKE in colorbar and tracked landmarks (yellow)

3.8 Results

This section presents the findings of my investigation into the navigation system's filter configuration, spanning the initial setup and tuning process, filter consistency and characteristics, default configuration performance, LRF measurement sensitivity, and Monte Carlo analysis.

3.8.1 Filter Configuration and Consistency

Two requirements must be met by a consistent state estimator: ensuring zero-mean estimation errors, and maintaining a covariance matrix that is either smaller or equal to the one computed by the filter as described in [124]. To assess the consistency of the developed EKF, ideal measurements are used for LRF via Eq. 3.4 and for the camera using Eq. 3.3. This process involves utilizing precise state information from the simulator as input to these equations. White noise with a known variance is then introduced to these ideal measurements. These variances are incorporated into the EKF via the measurement covariance matrix R. Consequently, the filter's output must be compliant with the two requirements for a consistent state estimator.

The position and velocity knowledge errors are presented for a sample run. The knowledge error is defined as the difference between true and estimated quantity. The filter performances are shown in Figure 3.18.

Several observations can be made from this figure:

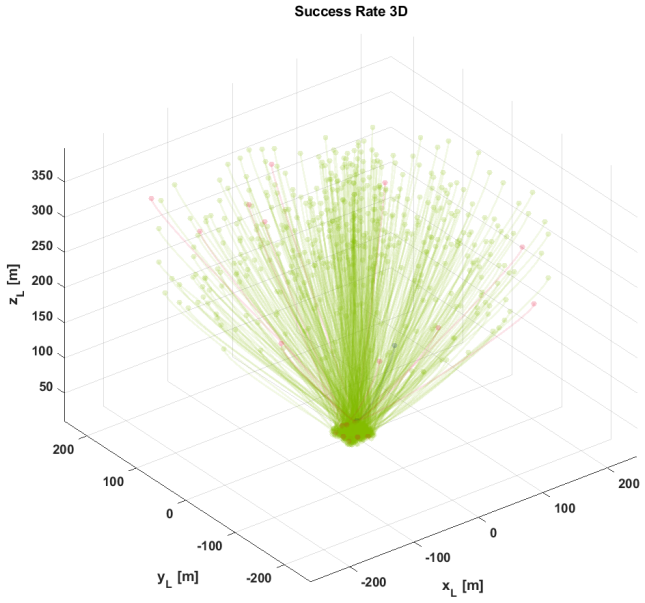

Figure 3.17: Sample landing trajectory used for Monte Carlo analysis: green and red respectively success and failed requirement trajectory

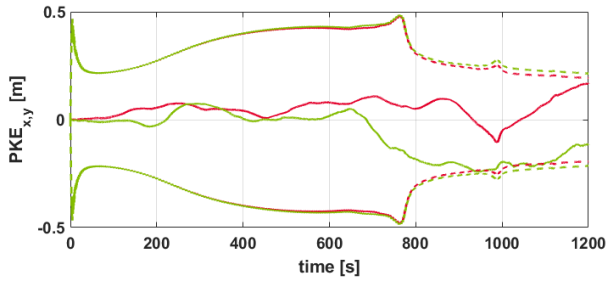

(a) PKE on x-(red) and y-axis (green)

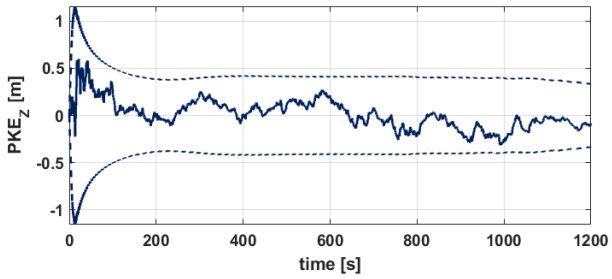

(b) PKE on z-axis

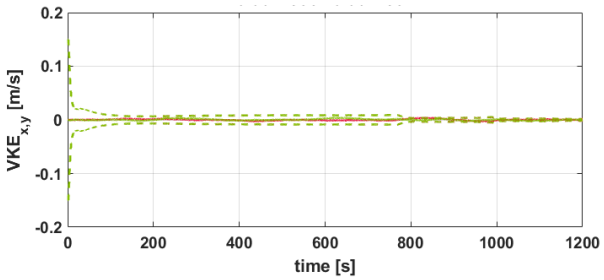

(c) VKE on x-(red) and y-axis (green)

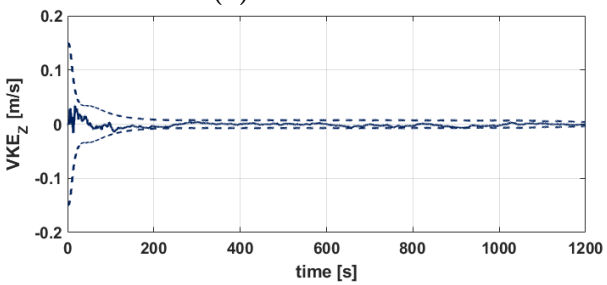

(d) VKE on z-axis

Figure 3.18: EKF performances: position and velocity knowledge error and predicted covariance (dashed).

- The EKF is consistent on the three-axis for position and velocity.
- The estimated across bore-sight dimension has slightly more bias compared to the LOS direction: this is due to the presence of LRF precise measurement along the z-axis, which increases the observability along that particular axis.
- The estimated quantities and their predicted uncertainties comply with the navigation requirement as in Equation 3.26.
- The abrupt decrease in the predicted covariance along the x- y-axis is linked to the triggered features refresh. New features are detected with the same initial pixel covariance as t_0; however, at lower altitudes, it translates into lower metric covariance than the filter initial condition. In other words, once the features are initialized at a lower altitude, the measurements have higher accuracies.

The increase in the drift in the final phase of the simulation is connected to the limit in simulation resolution. Since the 3D landing site area model cannot have infinite resolution, the quality of the detected features at the end of the simulation is low, as shown in Figure 3.19. The predicted drift stays bounded and limited during the LAP.

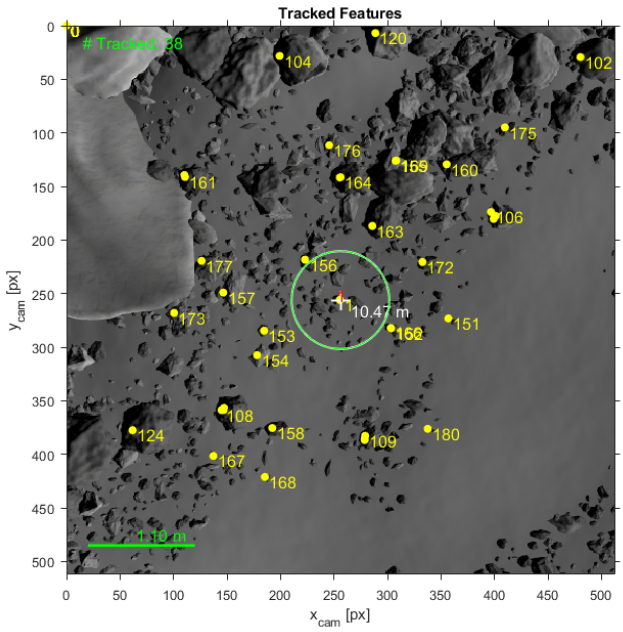

Figure 3.19: Final landing image: in yellow tracked features, note the lower resolution at such a low altitude due to simulation limitations.

Navigation filter default configuration

The default configuration for the navigation filter established after this initial testing phase is given in Table 3.7.

Setting	Value	Unit
Pointing Strategy	Target landing site	-

Setting	Value	Unit
Approach Trajectory	Vertical descent	-
Starting Altitude	300	m
Final Altitude	10	m
Flight Time	0.5	h
Accelerometer Sample Time	0.125	s
Cam & LRF sample time	5	s
Acc. uncertainty (1σ)	2.8284e-4	m/s^2
Acc. bias uncertainty (1σ)	2.8284e-5	m/s^3
R_{cam} uncertainty (1σ)	adaptive	-
R_{LRF} uncertainty (1σ)	0.5	m
Initial error and uncertainty	0	-

Table 3.7: Navigation filter settings in default configuration at LAP

3.8.2 LRF Measurement Sensitivity

The LRF significantly improves the filter consistency and estimate accuracy. In Figure 3.20a and Figure 3.20b, the position and velocity knowledge error is shown with and without the LRF measurement.

The significant contribution is brought on the z-axis, i.e., the LOS axis, by increasing position and velocity observability. For the x- and y- axis, there are only minor changes in the knowledge errors. Still, on the z-axis, the estimates' accuracy and consistency improve using the LRF unit. The most considerable effect of LRF is found on the position knowledge error on the z-axis (Figure 3.20a); the z-position estimate becomes inconsistent on the center of the trajectory by going beyond the 3σ bounds when the measurement is not used. Moreover, the 3σ bounds are significantly higher than the case with LRF, implying an inaccurate estimate.

This analysis shows as the LRF improves the estimate accuracy being a fundamental sensor for the landing scenario. In particular, the sensor enhances the observability along LOS compared to the pure monocular camera approach [125].

3.8.3 Monte Carlo Analysis

To test the robustness of the filter to a variety of initial and end conditions, a Monte Carlo analysis of the boundary conditions has been run. The goal of the study is to assess if there are limit trajectories that degrade filter performances. In particular other sensitivity analysis linked to Sun phase angles or camera artifacts has already been presented in [9].

The initial and end conditions for the analysis are randomly sampled to generate 600 trajectories. The initial state derives from a spherical section volume centered at the nominal landing site, while the end condition is located inside a box centered on the nominal landing site. The distribution values are presented in Table 3.8, and some trajectories are shown in Figure 3.17. Figure 3.21 presents the generated boundary conditions.

Some condensed metric has been identified to synthetically assess the Monte Carlo analysis results. In particular, the analysis shall verify the requirement for the navigation as defined in

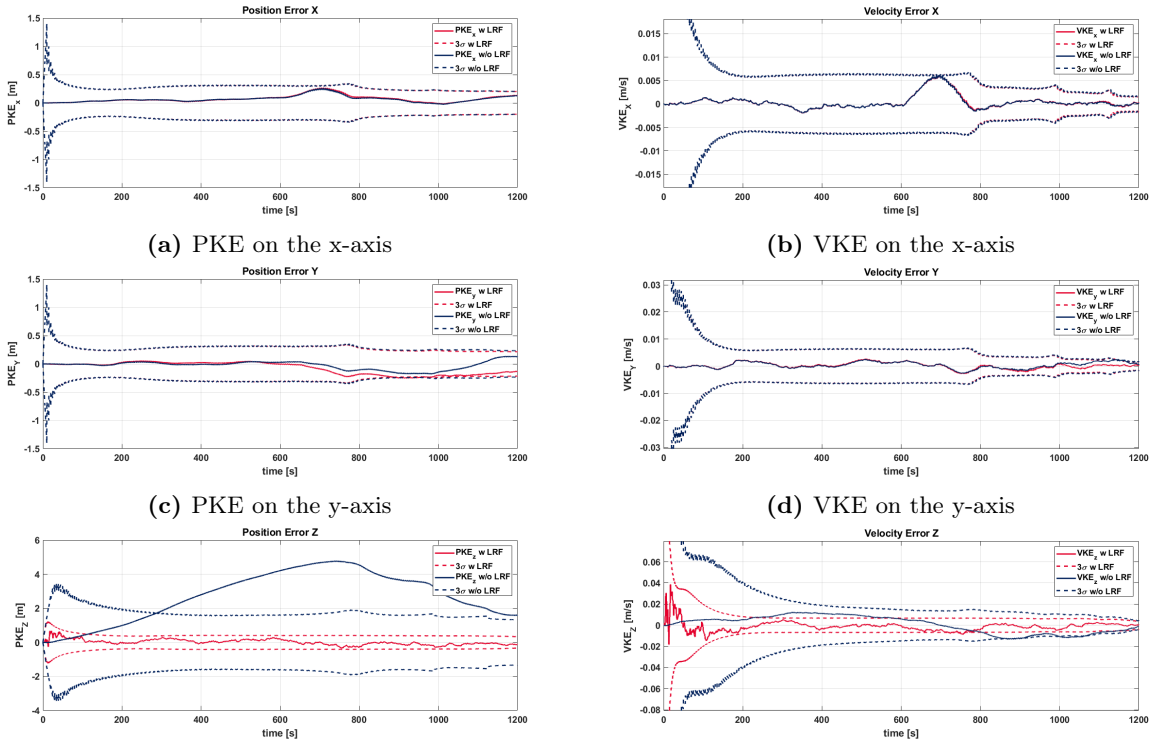

(a) PKE on the x-axis

(b) VKE on the x-axis

(c) PKE on the y-axis

(d) VKE on the y-axis

(e) PKE on the z-axis

(f) VKE on the z-axis.

Figure 3.20: LRF measurement performances with (red) and without (blue) LRF measurement and predicted covariance (dashed).

Setting	Value	Unit
Initial condition azimuth	[0-360]	°
Initial condition elevation	[40-90]	°
Initial condition range	[200-350]	m
End condition volume	30x30x10	m

Table 3.8: Monte Carlo Boundary Conditions

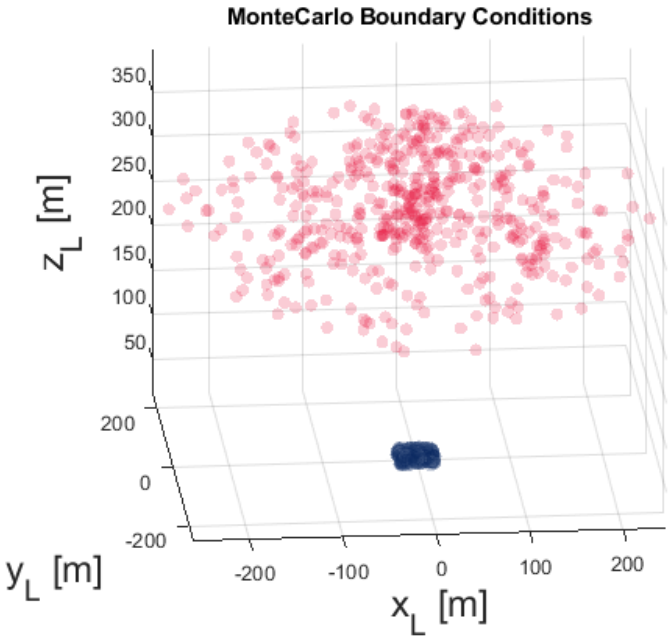

Figure 3.21: Monte Carlo initial (red) and end (blue) conditions.

Equation 3.26. Figure 3.22-3.23 presents a set of the analyzed trajectories.

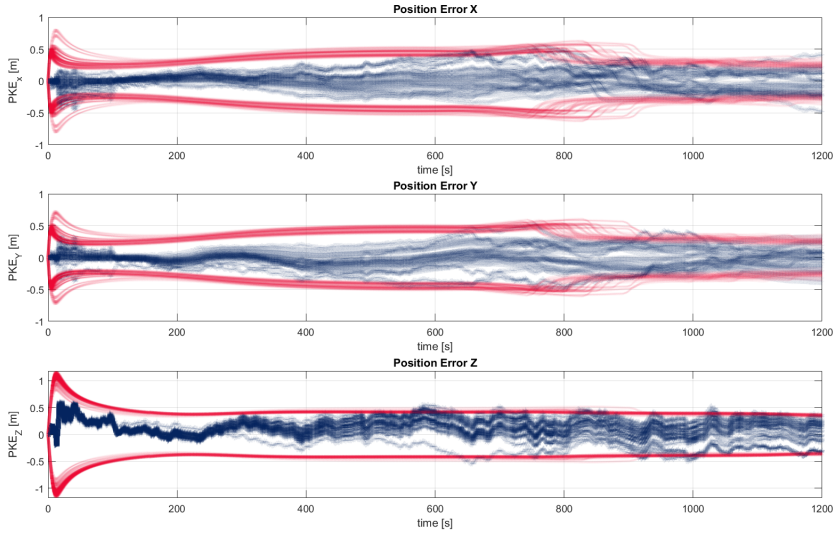

Figure 3.22: Monte Carlo analysis on boundary conditions: position knowledge error (blue), predicted covariance (red)

Figure 3.22 presents the Monte Carlo results for position knowledge error. It is noted that there is a much larger error distribution at the end of the trajectory because the effects on the end condition are more evident and result in different surface textures and light conditions. On the contrary, the initial condition distribution is minimal due to fewer changes in the images (textures, lightning) at the start of the trajectory. Moreover, different selected features may trigger refresh at other times; this is visible in the predicted covariance (red). The covariance decreases for different runs linked to the refresh, which can be triggered sooner or later during the trajectory.

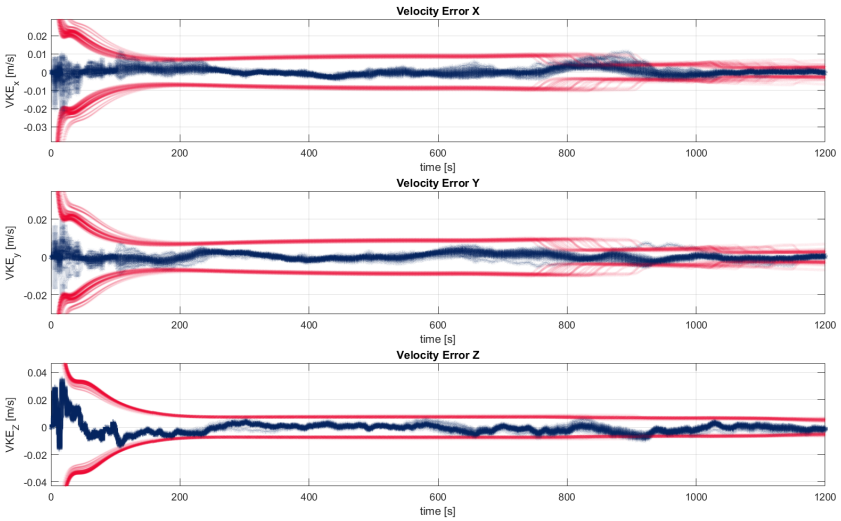

Figure 3.23: Monte Carlo analysis on boundary conditions: velocity knowledge error (blue), predicted covariance (red)

Similar considerations are valid also for Figure 3.23; it is also noted that the error distribution is smaller on the z-axis because the presence of direct LRF measurement limits the influence on boundary conditions (i.e., different surface textures or changes in lighting conditions).

The main requirement checked is that the position knowledge error [126] stays within 10% of the distance from the surface.

$$PKE \leq 10\% |\mathbf{r}_L^{LB}| \tag{3.26}$$

On a single trajectory, this requirement may be verified only partially. In particular, it is assessed for how long this requirement is verified along a trajectory, and the time of compliance is defined as:

$$Time\ Compliant = \frac{t^*\,(PKE < Req.)}{t_{TOT}} \tag{3.27}$$

Where t_{TOT} is the specific simulation time of a trajectory and t^* states for how long the requirement is verified in Figure 3.24a it is shown that for approximately 98% of the simulation, the requirement is verified 100% of the time, i.e., for the entire simulation. Also, it can be seen that less than 1% of the simulation is compliant for less than 30% of the time. In other words, 98% is compliant with the requirement on position knowledge error.

Another interesting metric is to assess how far the position knowledge error is outside the requirement. It is possible to state that the requirement is almost verified if the trajectory is close to the aforementioned 10% threshold. Figure 3.24b presents the compliance distance frequency. It is highlighted that the majority (99%) of the simulation has a minimal compliance distance, and less than 1% has a considerable compliance distance. These latter are linked to limit cases trajectory that, due to the initial-end conditions combination, have very high glide slope angle and, consequently, low navigation performance due to invalid LRF measurement. An example image is presented in Figure 3.25, here LRF is invalid for most of the trajectory, some poorly observable

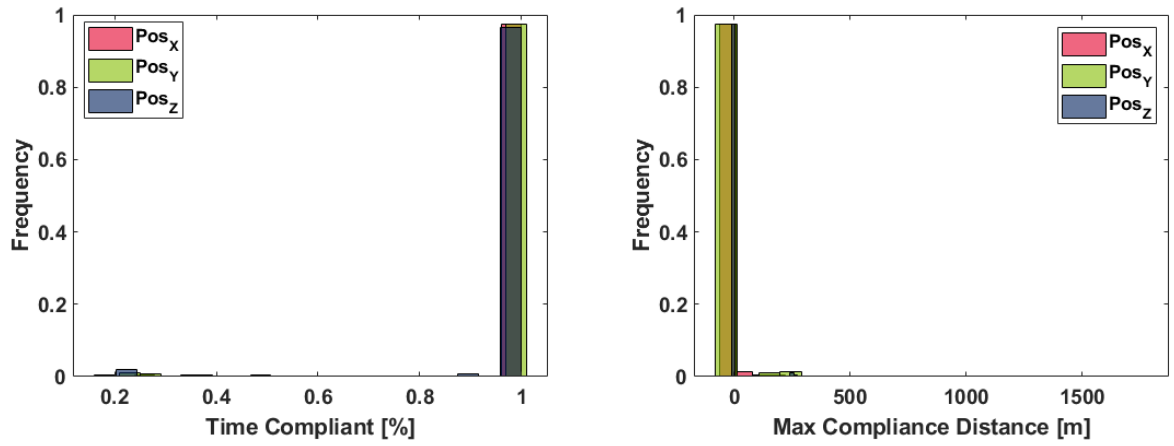

(a) Compliance time of position knowledge requirement. **(b)** Compliance distance of position knowledge requirement.

Figure 3.24: Monte Carlo compliance analysis

trajectories, the red ones, are presented in Figure 3.17.

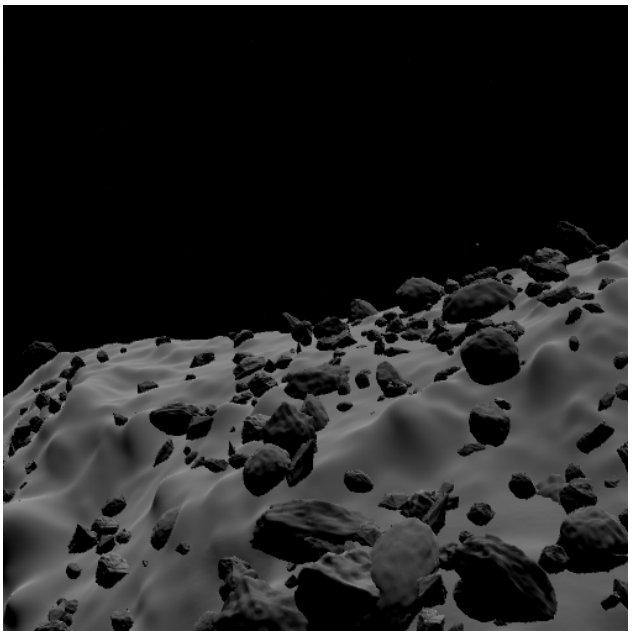

Figure 3.25: Example of limited observability.

Once the trajectories that comply with the main navigation requirement have been evaluated, the quality of these must be assessed. In particular, the consistency of EKF is checked for each successful trajectory. Two primary metrics are used: the duration of consistency and the consistency error. A filter is defined as consistent (see Section 3.8.1) where the knowledge error is within the 3σ bound.

The following analysis has been run on the subset of trajectories compliant with the requirement. In Figure 3.26a, the consistency time is presented: it is shown that 35 % is consistent for the entire simulation, and the majority of the simulations are consistent for 80% of the time or more. From Figure 3.22, it can be seen that in a few samples, the filter starts to get inconsistent at the end of the simulation, and this is due to the limited simulated resolution of boulders, i.e., features close to

the end conditions. In other words, the features at the end of the simulation have degraded quality, and the filter tends to be more inconsistent.

However, if the consistency distance is presented, as in Figure 3.26b, it can be seen that most of the sample is inconsistent for a minimal space, below $<0.25\ m$. Approximately 60% of the inconsistent sample has a maximum error from 3σ of less than 25 cm.

Finally, the Monte Carlo analysis was conducted to test the extended Kalman filter's robustness to various initial and end conditions. Six hundred trajectories were randomly sampled and analyzed to assess whether limit trajectories would degrade filter performance. The main requirement tested was whether the relative position knowledge error was smaller than 10% of the distance from the surface, as defined in Equation 3.26. The analysis found that for approximately 98% of the simulation time, the requirement was verified 100% of the time. Additionally, the compliance distance frequency showed that the majority (99%) of the simulations had minimal compliance distances. However, less than 1% of simulations had considerable compliance distances due to limit cases trajectories with high glide slope angles and invalid LRF measurements.

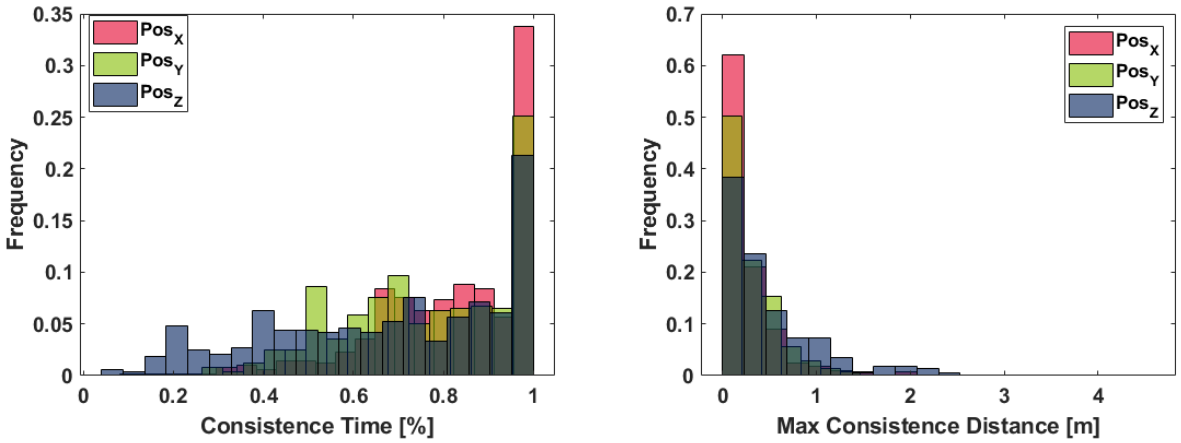

(a) Consistence time of position knowledge requirement. **(b)** Consistence distance of position knowledge requirement.

Figure 3.26: Monte Carlo consistency analysis

3.9 Lunar Landing Extension

This section highlight the needs for planetary landings, specifically targeting lunar surfaces. As humanity extends its reach beyond Earth, the exigencies of precision landing technologies on diverse planetary bodies become increasingly paramount [127]. This section is dedicated to an examination of lunar landing test case, with a specific focus on the transference and implementation of the current navigation filter algorithms to Moon environment.

At the core of this extension is the investigation into the adaptability of navigation filter algorithms to the lunar landing test case. The lunar surface, characterized by distinctive geological features, serves as an experimental platform to assess the operational efficacy of existing algorithms within this unique context .

A fundamental objective in this research is the modelling of large portions of lunar terrains, in contrast with the limited asteroid surfaces [128]. The spotlight is on understanding the adaptability

and critical points in the current navigation filter setup when dealing with the differences of lunar landscapes. This work represent only a preliminary initial analysis, the final aim is to fine-tune and optimize the current navigation systems, boosting the ability for precise and safe planetary landings in the future, with a special focus to lunar missions.

3.9.1 Argonaut Mission Test Case

The Moon holds a central position as a target mission for humankind, driven by a historical pursuit that spans millennia [129]. Recent decades have witnessed significant strides in lunar exploration through orbital, landed, robotic, and human missions, leading to substantial advancements in lunar knowledge [130]. The Moon's appeal transcends scientific curiosity, attracting global interest for technology research, scientific exploration, and potential resource mining.

Ongoing and planned robotic missions, propelled by breakthrough technologies and recent scientific discoveries, underscore the contemporary lunar exploration landscape. China's Chang'e missions, with rovers and orbiters exploring the dark side of the Moon, stand out as noteworthy accomplishments [131]. Meanwhile, private entities such as SpaceX and Blue Origin, along with upcoming university projects, contribute to the expanding lunar mission landscape [132]. Anticipating the return of humans to the Moon, the NASA leads an ambitious international effort, the Artemis program [133]. In collaboration with Japan, Europe, and Canada, the program aims to land humans from 2025. This marks a significant milestone in lunar exploration, highlighting collaborative endeavors on a global scale.

Among the pivotal lunar missions, the Argonaut Lander plays a prominent role within the ESA Terrae Novae Exploration Programme [2]. Formerly known as European Large Logistic Lander – EL3, Argonaut's Lunar Descent Element (LDE) is slated to deliver scientific or logistic payloads to the lunar surface from 2030 onward. With a focus on cargo delivery missions in support of the Artemis program, sample return, and scientific/technology demonstration endeavors, Argonaut's objectives are extensive.

Argonaut, weighing approximately 10 tons, possesses the capability to deliver up to 1500 kg of payload with pinpoint landing precision. The Lunar Descent Element (LDE) incorporates advanced GNC capabilities, including Terrain Relative Navigation (TRN), HDA, and throttleable engines.

The current test case is based on a Argonaut baseline lunar descent from main braking burn (MBB) to touch down (MECO). The concept of operations is presented in Figure 3.27 and it is defined into the open loop simulator to test the navigation.

3.9.2 Lunar South Pole Simulation

Initially, an open-loop simulator is developed with specific assumptions: the utilization of a flat moon model, neglecting lunar curvature, maintaining constant gravity throughout the landing, and disregarding any rotational effects of the moon.

The simulated terrain encompasses a 150 km x 150 km area around the South Pole [134]. The original NASA Digital Elevation Model (DEM) serves as the basis for this simulation. The Shackleton crater DEM is specifically obtained from 75S to the South Pole (90S) at a resolution of 30 m/px, then is cut to a square area of approximately 150 km per side. The South Pole coordinates are applied in this context. Further refinements include defining regions of enhanced resolution,

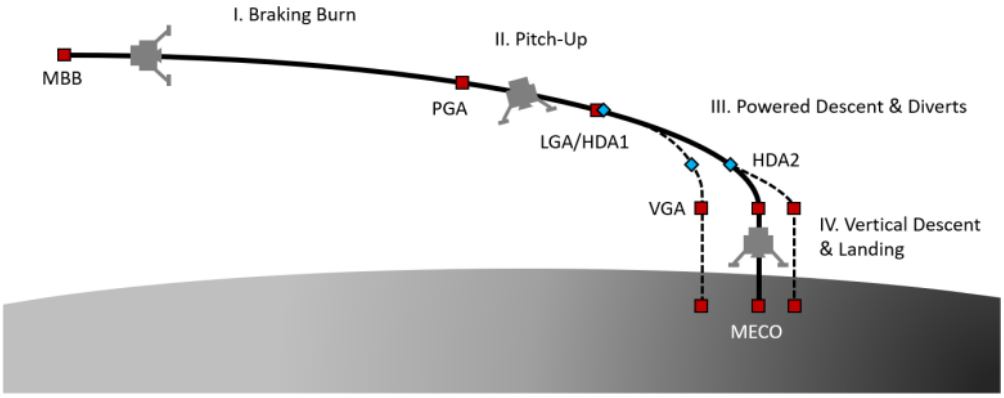

Figure 3.27: Descent and landing scenario from [2]

reaching up to 6 cm/px.

The Argonaut landing site, situated in proximity to the Shackleton crater rim, is characterized by specific coordinates. Crater and boulder modeling follows, with craters ranging from 1 m to 100 m being simulated in a designated area of 50 km x 50 km around the landing area. Boulders, spanning from 0.5 m to 15 m, are modeled in an area of 150 m x 150 m around the landing site. To enhance the accuracy of the simulation, SPICE kernel sun elevation is applied.

The Argonaut baseline trajectory is imported into the simulator, integrating the refined terrain and environmental parameters. This comprehensive approach ensures a detailed and consistent simulation of the lunar landing scenario.

In Figure 3.29 and Figure 3.28 some sample image from the landing sequence are shown, in the vertical descent overall illumination has been increase for better printing results.

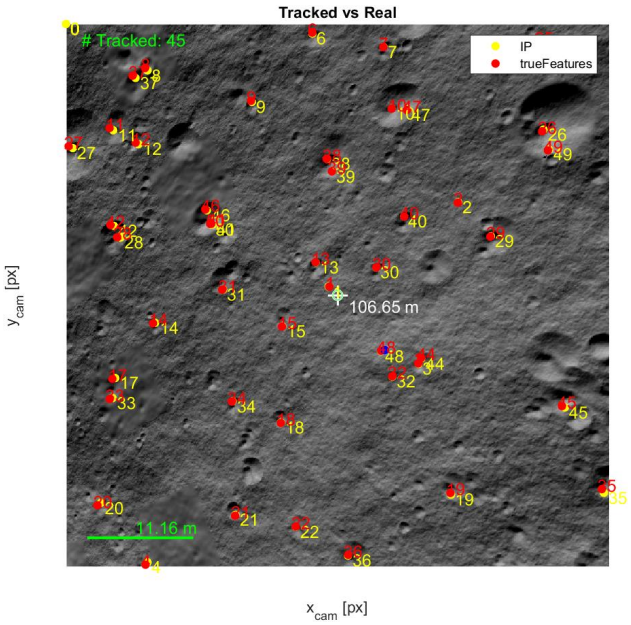

Figure 3.28: Terminal vertical descent approach with tracked features

The navigation equations are the same in Equation 3.9 with the aforementioned assumptions, and the same filter parameters are applied as defined in Table 3.7.

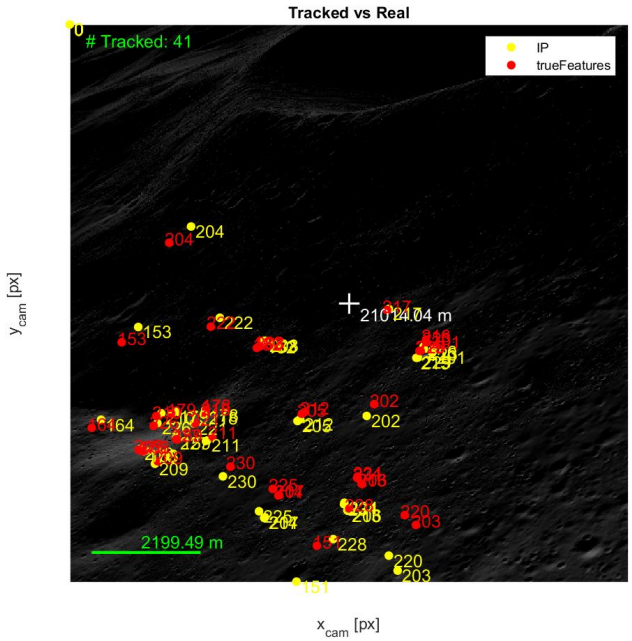

Figure 3.29: Initial landing phase with tracked features

3.9.3 Adaptations and Criticalities

In summary, this section comprehensively outlines the primary adaptations required and critical considerations inherent in the current lunar navigation approach. Distinct disparities compared to the asteroid scenario have been identified, manifesting in significantly faster dynamics, condensing the operational timeframe from 30 minutes to a mere 30 seconds for the lunar case (terminal vertical descent). The lunar environment introduces challenges, including lower feature density, prompting the necessity for a feature manager. The feature manager should assess the quality of each initialized features and manage their distribution over the frame for increased observability. Moreover, limitations arise from the impracticality of achieving high-fidelity surface modeling for extensive lunar terrains due to hardware constraints, notably the limitations of RAM for model loading.

The attitude of the lander preceding terminal descent further complicates matters, rendering the current filter initialization suboptimal. Notably, the baseline Argonaut camera pointing proves to be non-optimal in a non-Nadir orientation, impeding Laser Range Finder (LRF) filter initialization. This culminates in the infeasibility of conventional LRF initialization, prompting the proposal of using a moon shape model as an alternative means of filter initialization.

Moving forward, these identified challenges serve as focal points for future improvements if the current solutions are to be considered for the advancement of lunar navigation technologies. Addressing the accelerated dynamics, refining feature management strategies, overcoming hardware limitations for surface modeling, optimizing trajectory initialization, and innovating LRF initialization methods are improvements for future research and development in the domain of lunar exploration.

3.10 Conclusion

In conclusion, one of the main advantages of the novel EKF based on SLAM is its ability to increase the observability of the LOS. Using a LRF, the filter can better estimate the position and orientation of the spacecraft relative to the planetary surface, even in challenging environments with few distinguishable features. This increased observability enhances the filter's ability to estimate the spacecraft's state, particularly during the final landing stages when high accuracy is critical.

Another advantage of the novel EKF is its efficient use of features and reduced number of them. This reduces the computational burden of the algorithm, making it more suitable for on-board implementation. Additionally, the reduced number of features allows for faster processing and improved reliability, as fewer features mean fewer opportunities for errors in feature detection and matching.

The Monte Carlo analysis of the filter demonstrates its robustness to boundary conditions. This is particularly important in space exploration missions, where the spacecraft may encounter unexpected obstacles or environmental conditions. The ability of the filter to handle such scenarios and maintain accurate estimates of the spacecraft's state further enhances its reliability and usefulness for space exploration missions.

A simplified planetary landing test case is investigated highlighting the need for the filter adaption to account to the different environment in terms of dynamics and surface features.

Overall, the novel extended Kalman filter based on SLAM represents a significant advancement in space exploration and autonomy. Its ability to increase observability, use features efficiently, maintain accuracy in challenging conditions, and provide a relative estimated state for closed-loop guidance makes it a highly promising technology for the future of space exploration.

Chapter 4

LiDAR-Free Hazard Detection and Landing Site Selection

This chapter explores the critical aspects of LiDAR-free hazard detection and safe landing site selection for autonomous landing systems. I present the foundational landing autonomy framework, outlining its essential components and mechanisms. Subsequently, the safe landing site selection functionalities is analyzed, discussing the algorithms and methodologies used to identify suitable landing locations while mitigating potential hazards. This investigation then delves into the advancements in deep learning developments, showcasing the integration of deep learning techniques to enhance hazard detection and landing site evaluation. Through an in-depth analysis and performance assessment, I quantify the effectiveness and accuracy of my approach, considering various real-world scenarios and challenges. Finally, the chapter culminates in a conclusion, summarizing the findings, highlighting the strengths of this methodology, and outlining potential avenues for future research and improvement in LiDAR-free hazard detection and safe landing site selection for autonomous landings. Autonomous Safe Landing Site Selection (SLSS) is described in this section.

4.1 Introduction

Hazard identification and the selection of an appropriate landing site with autonomous capabilities involve recognizing threats that jeopardize the mission and pinpointing the optimal landing location based on mission criteria. HDA systems are designed to execute a spectrum of critical tasks, encompassing shadow detection, feature detection, slope estimation, and surface roughness estimation, among other functions. The significance of these tasks lies in their collective contribution to ensuring the spacecraft's ability to autonomously identify and circumvent potential hazards during the descent and landing phases. In the following paragraphs a brief state-of-the-art review will be presented focusing on the current systems and highlighting the main challenges of these class of methods. Finally, the research contribution will be highlighted.

4.2 Autonomy for Hazard Detection and Landing Site Selection

4.2.1 Current Hazard Detection Systems

The integration of hazard detection and avoidance systems in planetary missions has seen significant evolution over time. Historically, most planetary missions lacked dedicated terrain hazard detection and avoidance capabilities, relying primarily on human-operated apparatus or simpler methods. Notable examples include the Apollo missions, where the hazard detection system was essentially the human eye [135], with the consequent increased risks see Figure 4.1.

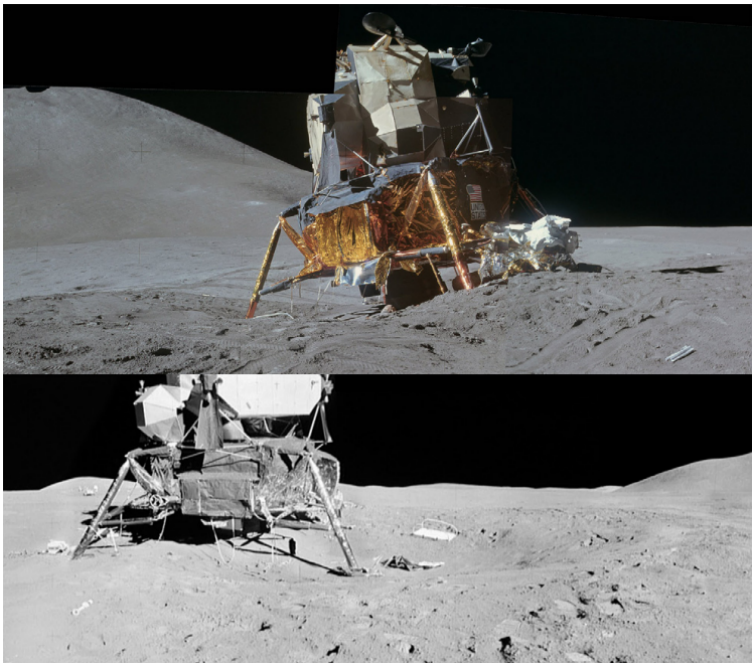

Figure 4.1: The Apollo 15 lunar lander positioned on the edge of a small crater is depicted in these two images. The landing incurred a tilt of approximately 11 degrees, merely 1° from maximum allowable limit, leading to damage to the engine bell. [3]

The Chang'e-3 mission marked a turning point by implementing an autonomous Hazard Detection and Avoidance (HDA) system using a two-step approach [136]. This involved classical image processing and a LiDAR system for precise hazard avoidance, showcasing a more advanced and automated hazard mitigation strategy.

Mars 2020, with the Perseverance rover, introduced a groundbreaking approach by utilizing an on-board hazard map referenced to observed images for hazard-relative navigation [137]. The hazard map, generated in the years leading up to launch through analysis of high-resolution data, covered multiple candidate landing sites.

Similarly, the Tianwen-1 mission [138] adopted a two-step guidance system akin to Chang'e-3, emphasizing the importance of autonomous hazard detection and avoidance in modern planetary exploration. For aerial exploration, the Ingenuity helicopter employed inertial navigation with optical odometry relative to pre-mapped hazards [139]. This innovative approach allowed for dynamic hazard avoidance during flight, demonstrating the adaptability of hazard detection systems across different mission profiles.

To focus on SSSB missions, limited examples of HDA exists: optical navigation relative to mapped natural features was utilized by the OSIRIS-REx mission, showcasing the versatility of

hazard detection methods [140]. This strategy involved navigating relative to pre-mapped natural features on the target asteroid.

Lastly, the Hayabusa-2 mission employed prior mapping and optical tracking relative to a target marker, emphasizing the importance of comprehensive hazard assessment before and during the mission [141].

It is highlighted that no fully autonomous systems currently exist. All the mentioned solutions are inherently based on prior knowledge and pre-mapping of potential hazards. Even in instances where advanced techniques such as LiDAR systems, image processing, or optical navigation are employed, these technologies rely on data collected and analyzed prior to the mission.

4.2.2 Challenges in HDA and Landing Site Assessment

Autonomous hazard detection and landing site assessment in space exploration pose formidable challenges, contributing to a historically low success and survival ratio of landing attempts. For instance, more than 60% of Mars exploration missions launched by NASA and ESA have encountered failures [142], with many attributed to complications during the landing phase. This trend underscores the critical need for advancements in autonomous systems to enhance the precision and reliability of landing procedures.

A particularly intricate challenge arises from the diverse and often hazardous terrain that planetary and SSSBs landers encounter. Many landing points of interest are situated in areas surrounded by craters, rocks, ridges and other geological hazards. The detection algorithms must, therefore, exhibit versatility in adapting to complex environments and operate autonomously to promptly identify and mitigate potential hazards [143].

Moreover, the inherent long communication delay induced by the vast distances between target planets and Earth-based base stations adds another layer of complexity. Combined with the limited capabilities of traditional planetary landing Guidance Navigation and Control modes, this communication lag restricts the effectiveness of real-time ground-based hazard detection and avoidance systems.

4.2.3 Recent Research

Three primary categories of solutions can be delineated:

1. A solution based on visual input supplemented with distance data [144].
2. A solution based on LiDAR technology [145].
3. Solutions that blend visual inputs [35] with direct depth measurements [3].

The first category can be divided into two subsections: 1) employing a single camera and 2) using a stereo camera system. In comparison to a single camera setup, the stereo approach offers the advantage of directly estimating and reconstructing surface 3D characteristics using established stereo techniques, which mitigates issues like scale drift. Nonetheless, a drawback of the stereo system is its reliance on the lander's size and geometry. In simpler terms, the camera baseline capacity on the proposed lander restricts the range resolution.

To enhance the previous technique, current missions involving Near Earth Orbit (NEO) utilize bulky LiDAR devices [55] to detect dangers and assess surface conditions that might affect safe

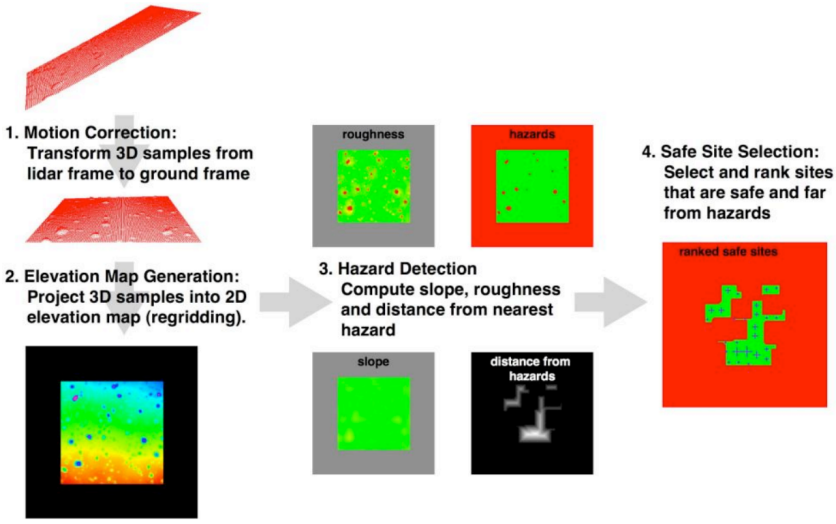

Figure 4.2: Typical HDA pipeline from [4]

landing [146]. The weight constraints of smaller designs (e.g., CubeSat) prevent the installation of on-board LiDAR, which also consumes more power compared to a passive sensor like a camera [147].

4.2.4 Research Novelties

The current strategy employs a combination of a single camera image and LRF measurements; these inputs are processed to create distinct safety maps directly associated with landing prerequisites: the identification of hazards (such as large boulders), minimum lighting conditions, maximum allowable surface slope, proximity to the designated landing site, and minimum distance from unsafe landing areas. The proposed approach seeks to address the challenges posed by a bulky LiDAR device and the inability of small landers to achieve a sufficient stereo baseline for depth resolution at operational altitudes.

An independent hazard detection system without LiDAR is introduced, enabling the on-board selection of safe landing sites based on specified requirements. The system's effectiveness is demonstrated and validated using the μLander configuration within the context of the NEO-MAPP study [1, 67], which serves as an ideal scenario for testing autonomous and secure landings on an asteroid's surface. The innovative solution seamlessly combines machine learning-driven (Machine Learning (ML)) hazard detection and slope estimation with traditional image processing (IP), resulting in a hybrid workflow.

The researched Safe Landing Site Selection system optimizes weight and cost, thereby serving as a facilitating technology for exploration missions demanding a high level of autonomy. The proposed algorithm delivers essential hazard detection [69] and avoidance functionalities, ensuring autonomy in the selection of a landing site that adheres to safety criteria.

4.3 Landing Autonomy Framework

The general SLSS routine uses navigation information, direct sensor measurements, and pre-configured parameter to assess the optimal landing site. The landing site shall verify the requirements in Table

2.4. The target landing site in the camera reference is the final output. Given the current state estimate, this information must be converted to the L-frame, as defined in Section 3.7.4.

The requirements maps are generated using classical IP coupled with the navigation estimates and ML strategies. Machine supervised learning functions allow us to predict with enough accurate information, which would require a heavier LiDAR unit [148]. In particular, hazards and slope information is derived by training neural network models on expected mission scenarios derives hazards and slope information. Fuzzy logic fuses the different maps into a final safety map.

The deep learning developments are detailed in Section 4.5. The fuzzy logic applies a human-based language and imports fusion parameters directly from landing system requirements [149]. Combining landing requirements and human-based rules minimizes the number of free design parameters in the fusion process, making this innovative approach more robust to various environmental conditions. The target landing site is assessed on the final safety map obtained and communicated to the guidance for re-targeting.

4.3.1 Inputs

The SLSS uses two primary sensors as inputs: the camera is used for most operations and functionalities, and the LRF is used mainly to establish a dimension conversion from pixel unit to metric unit. Additional information to the SLSS is provided by the LAPNAV solution. The RGB 1 MP resolution and 1 s sampling time, as shown in Table 4.1.

Category	Specification
Model	Pinhole
FOV	30 degrees
Resolution	512 x 512 pixel
Focal Length	50 mm
F-number	1.2

Table 4.1: On-board Camera Specifications

4.3.2 Outputs

The final output of the SLSS block is the position of the target landing site in the camera sensor reference frame $\mathbf{f}^*$. This output needs to be processed with the estimated camera pose and the LRF measurement to provide a target landing site position in the L-frame to the guidance algorithm:

$$\mathbf{r}_B^{Li} \approx \mathbf{K}^{-1}\mathbf{f}^* \tag{4.1}$$

$$\mathbf{r}_L^{Bi} = \mathbf{R}^{LB}\mathbf{r}_B^{Li} - \mathbf{r}_L^{LB} \tag{4.2}$$

where K is the intrinsic matrix to project the pixel position of the target landing site in the camera coordinate $\mathbf{f}^*$. Then, using the estimated lander position $\mathbf{r}_L^{LB}$ is possible to express the target landing site from B-frame to L-frame, the process is represented in Figure 4.3. The range information of the target landing site $\mathbf{r}_B^{Li}$ is provided by the direct LRF measurement as presented in Section 3.7.4.

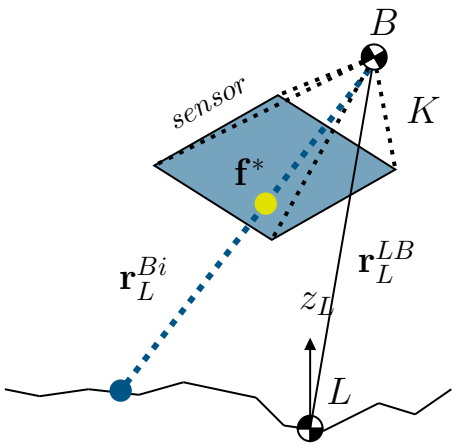

Figure 4.3: Target landing site projection sketch

4.3.3 Core Functionalities

Three main high-level functionalities compose the SLSS, as shown in Figure 4.4:

1. Pre-fusion: it fuses the slope, illumination, hazards, and reachability constraints to build an initial risk map.
2. Post-fusion: it fuses the preliminary risk map, reachability, and proximity constraints to build the final risk map.
3. SLSS decide the nominal if the landing site is safe and if the target landing site needs to be updated.

The two fusion functionalities are separated and run in series because the pre-fusion output must first be processed to build the proximity map. Given the requirements, the logic is a decision logic that outputs the optimal landing site $\mathbf{f}^*$. Figure 4.4 presents a high-level system description.

4.4 Safe Landing Site Selection Functionalities

In this section, all the direct input and output maps of the pre-fusion functionalities will be presented, and their functions described; a focus on the deep learning developments is detailed in Section 4.5.

4.4.1 Reachability

Input	Type	Output	Type	Parameter	Name
Nominal Landing Site	Double [3x1]	Reachability Map	Boolean [512x512]	Maximum distance from nominal landing site	α

Table 4.2: *distMap* interface definition

The input of this function is the nominal landing site location in the camera reference frame. The output is the *distMap* where 0 value is safe, and 1 is unsafe, which means too far from the

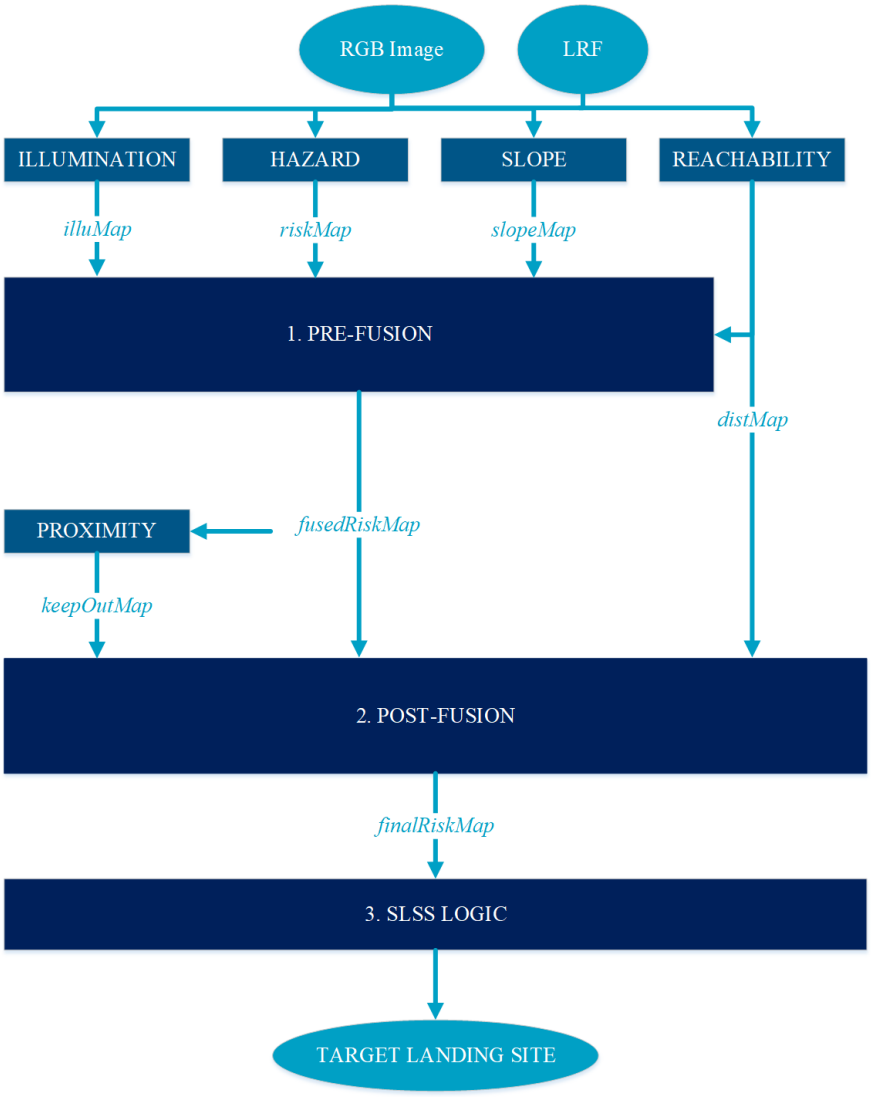

Figure 4.4: Core Functionalities High-Level Overview

nominal landing site. The map uses the $maxDivert = 3\alpha$ parameter (see Table 4.13), which states the maximum allowed distance from the nominal landing site. The parameter is derived directly from the landing requirement [35]. The map is built using a truncated 2D Gaussian distribution p(x) given by:

$$p(x) = \begin{cases} \frac{1}{|2\pi\Sigma|} e^{-\frac{1}{2}(x-\mu)^T \Sigma^{-1}(x-\mu)} & if\ |x| \leq 3\alpha \\ 0 & elsewhere \end{cases} \tag{4.3}$$

where μ is the nominal landing site position and Σ is the 3σ covariance equals to the 3α parameter. A sample map with a central position nominal landing site is shown in Figure 4.5.

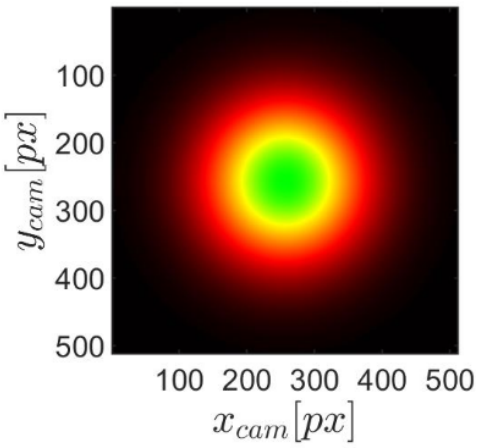

Figure 4.5: distMap example: red is unsafe, green is safe

4.4.2 Slope

Input	Type	Output	Type	Parameter	Name
RGB Image	Uint [512x512]	Slope Map	Double [512x512]	-	-

Table 4.3: slopeMap interface definition

The *slopeMap* generation is a ML-based process trained on a slope map ground truth to predict the slope for every pixel. The slope is defined as the angle between the line of sight vector from the spacecraft to the surface and the surface normal direction, as described in Figure 4.6. This slope definition does not account for the gravity direction. However, it is assumed that, on average, the gravity vector is aligned with the surface normal.

The input is the RGB image, and the output is the *slopeMap* expressed in degree. The prediction is based on a *U-net* [5] neural network architecture trained on various synthetic images and labeled depth maps. The main contribution of the *U-net* architecture is the shortcut connections. *U-net* proposes to send information to every up-sampling layer in the decoder from the corresponding down-sampling layer in the encoder [150]. Capturing finer information also keeps the computation low. Since the layers at the beginning of the encoder would have more information, they would support the up-sampling operation of the decoder by providing small details corresponding to the input image, thus improving the accuracy. A more detailed description of the deep learning process is presented in Section 4.5.

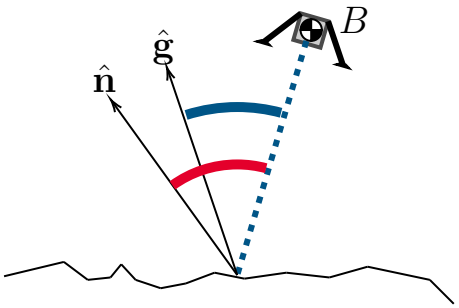

Figure 4.6: Slope definition sketch: measured slope (red), effective slope (blue)

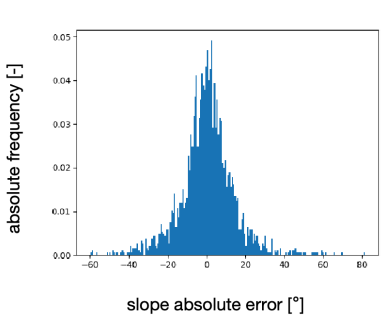

(a) Absolute slope error distribution: y-axis absolute frequency, x-axis predicted slope value.

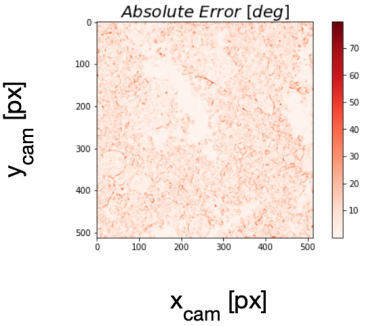

(b) Absolute slope error example: higher error is located on boulders edges.

Figure 4.7: Absolute slope error performances

The validation set statistics show an absolute estimate error (3σ) between 25-30 degrees, calculated over the entire dataset (42k images), as shown in Figure 4.7a. It is observed, see Figure 4.7b, that the highest estimate error is located where the slope angles are higher (close to boulders/craters edges), and since these locations are already excluded from the safety region by the other maps contributions, the estimated error does not concern the overall map quality in the area of potential landing. The predicted *slopeMap* is presented in Figure 4.8.

4.4.3 Illumination

Input	Type	Output	Type	Parameter	Name
RGB Image, Kernel Size	Uint16 [512x512] Double [1]	Binary Boolean Map	Boolean [512x512]	Shadow Tolerance	η

Table 4.4: *illuMap* interface definition

The input of this map is the RGB camera image, and the output is a binary map that is 0 for safe pixels (light) and 1 for unsafe ones (dark). The $shadowToll = \eta$ parameter (see Table 4.13) is linked to the thresholding operation, and the *kernelSize* is used as an additional input.

The final binary map is obtained in multiple thresholding steps, as shown in Figure 4.9.

1. RGB image is converted to grayscale.

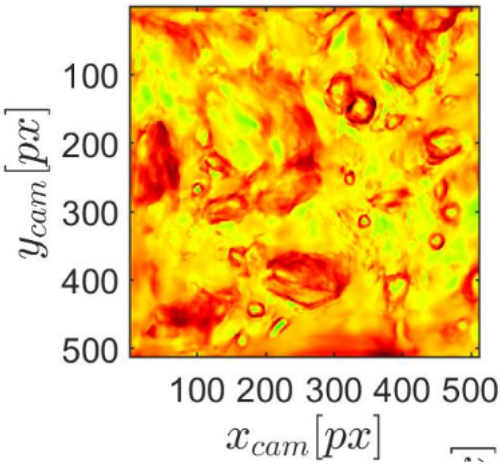

Figure 4.8: *slopeMap* example: smaller slope (green) and higher slope (red)

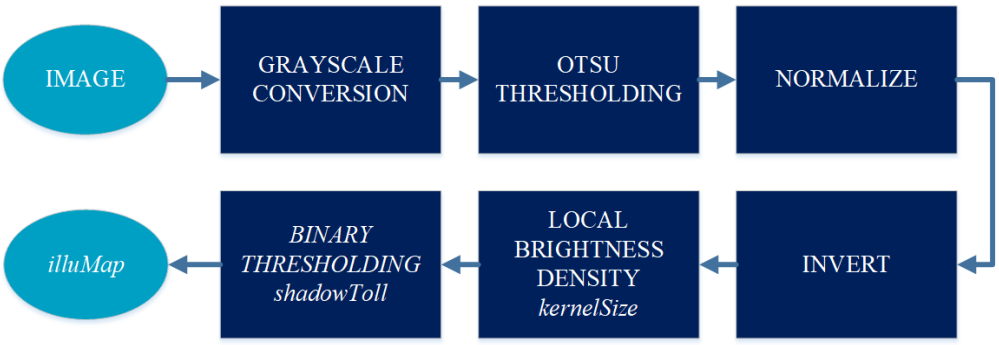

Figure 4.9: *illuMap* Generation Process

2. Otsu Adaptive Thresholding [151] is applied: this method is automatic, and the thresholding value is provided without intervention from the user (see Figure 4.10).

3. The image is encoded into 0-1 binary values: 0 values are linked to pixels darker than the threshold and 1 to pixels lighter than the threshold.

4. The local brightness density is evaluated: by using the kernel size as averaging window, the image is convoluted with a linear averaging kernel [152] as:

$$out(x, y) = \sum_{(x',y') \in kernel} kernel(x', y') * src(x + x', y + y') \tag{4.4}$$

Where $kernel = I_{kernelSize}$ and src is the binarized image.

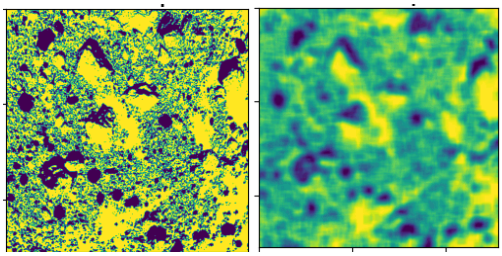

(a) Otsu's thresholding step **(b)** local brightness density

Figure 4.10: *illuMap* pre-processing

5. Binary thresholding is applied using the η parameter as level: according to the parameter intensity, the amount of brightness to be included in the unsafe regions is controlled by the user (see Figure 4.11).

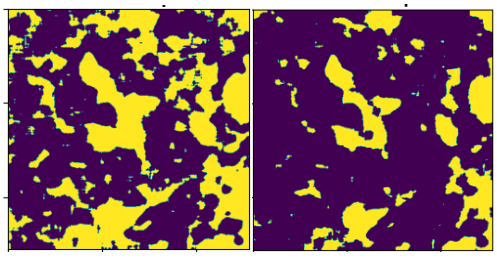

(a) η=70 % **(b)** η=80 %

Figure 4.11: *illuMap* example: yellow is unsafe, blue is safe

4.4.4 Boulders

Hazard

A detailed description of the present functionality is presented in Section 4.5.3, here it is shortly described for the sake of SLSS overview. The problem of boulders detection is identified as binary semantic segmentation; this formulation implies that the likelihood of being a hazard for each pixel is estimated. Thus, semantic segmentation consists of dense, i.e., pixel-wise predictions inferring labels for every pixel; in this case, the label is the *boulder/not-boulder* binary class.

Input	Type	Output	Type	Parameter	Name
RGB Image	Uint16 [512x512]	Hazard Map	Double [512x512]	-	-

Table 4.5: *hazMap* interface definition

The *hazMap* output provides a probability value from 0 to 1. The neural network is trained on various asteroid environments to avoid over-fitting to a specific condition.

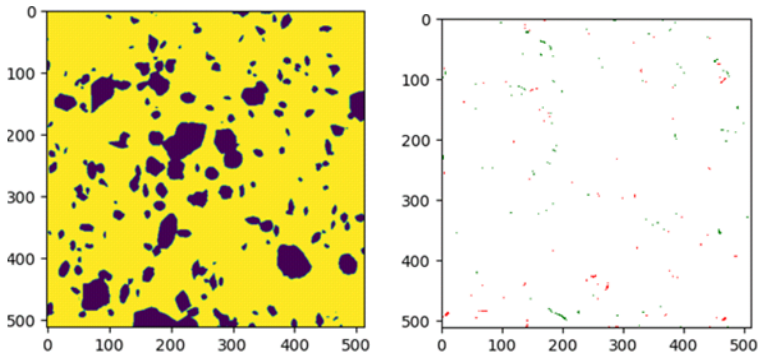

(a) Prediction **(b)** False positive (green)

Figure 4.12: *hazMap* Results

The raw output of the selected neural network is post-processed to include the information about the image scale (e.g., landing footprint and resolution) and to take into consideration the prediction probability, as shown in the flow chart below (Figure 4.13).

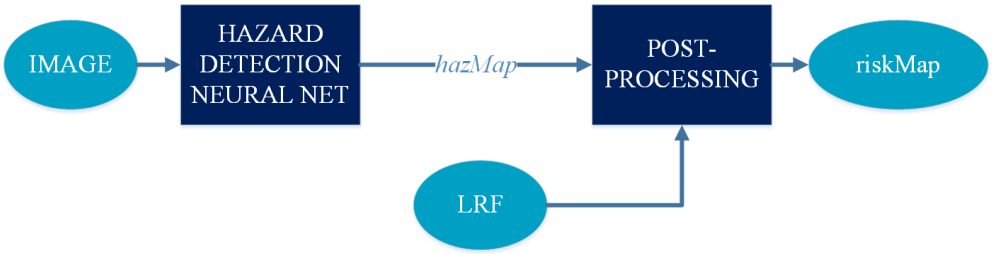

Figure 4.13: Post-Processing Workflow from RGB Image to *riskMap*

Hazard Map Refinement

The *riskMap* is built by processing the *hazMap* (i.e., the neural network prediction): the *riskMap* contains for each pixel the local rock density value. The local rock density is evaluated by averaging the *hazMap* values over a window of the size of the landing footprint obtained from the kernel size. In other words, an averaging filter is convoluted with the hazard map with a kernel size equal to the landing footprint.

The post-processing increases the safety of the hazard map; a point with no boulders, which is close (within a footprint size) to a very high detection probability area, has some rock density. While a small rock (i.e., a set of pixels where a boulder is detected) in a shallow detection probability area will have its density value decreased.

The methods allow filtering out boulders smaller than the lander footprint; thus, they do not

represent a risk for the landing. In addition, it increases the local rock density of areas close to dense boulders structure to avoid this area during re-targeting. The processing result is shown in Figure 4.14.

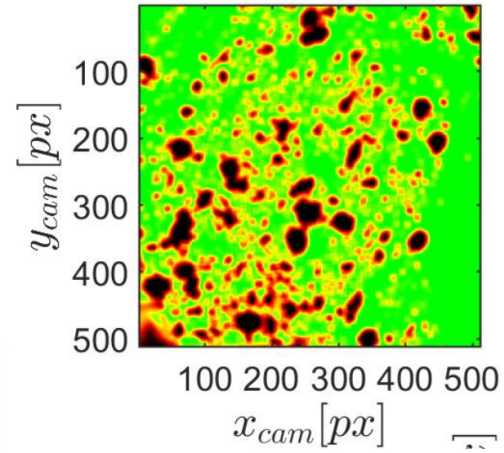

Figure 4.14: *riskMap sample*: green is safe and red is unsafe.

4.4.5 Preliminary Fusion

Input	Type	Output	Type	Parameter	Name
Boulders Map, Slope Map, Illumination Map, Reachability Map	Double [512x512]	Fused Risk Map	Double [512x512]	Maximum Roughness, Maximum Slope	γ, δ

Table 4.6: *riskMap* interface definition

The *fusedRiskMap* combines the previously mentioned maps by considering the roughness and slope requirements. The fusion implementation uses a look-up-table (LUT) approach. Fuzzy rules are defined to fuse the maps, and a multi-dimensional fuzzy function is obtained, then this function is encoded in a LUT [153]. On each pixel, the following operations are run:

1. Verify that the illumination map and the reachability map are safe.
2. If 1. conditions are valid, the fuzzy reasoning (LUT) is applied to the pixel.

The *riskMap* values are classified into three classes: smooth, rough, and very rough. The *slopeMap* values are classified into three categories: flat, incline, and steep. The class definition is established given the parameters provided by the requirements.

Once the requirements are set, the membership function design points are defined w.r.t. the requirement parameter (see Table 4.13), and the process is displayed in Figure 4.15. For the *riskMap* and *slopeMap* $\frac{1}{2}$ and $\frac{1}{4}$ of the set parameter.

Once the *slopeMap* and *riskMap* are fused according to the fuzzy logic defined rules, the resulting fused pixel can belong to four classes: safe, risky, very risky, and unsafe. These classes are defuzzified according to the following membership function to obtain the fused risk map value between 0 and 1. The unsafe area is increased to make the overall algorithm more conservative.

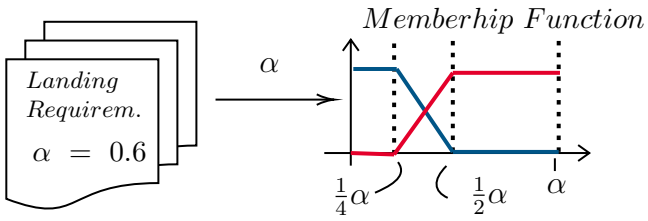

Figure 4.15: Membership function design process sketch

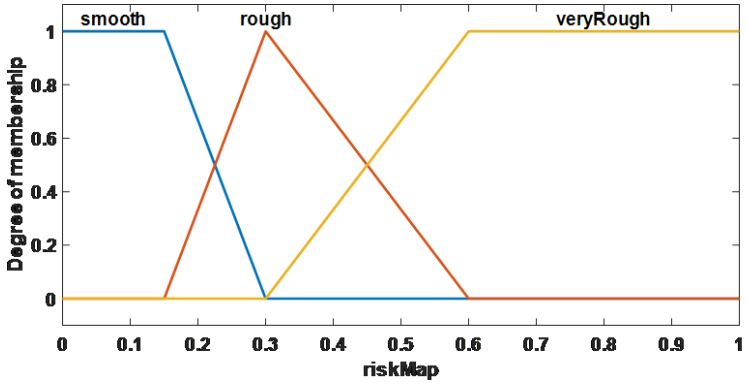

Figure 4.16: *riskMap* membership function: maximum roughness is set to 60% and design points are defined as $\frac{\gamma}{2}$ and $\frac{\gamma}{4}$ of the parameter

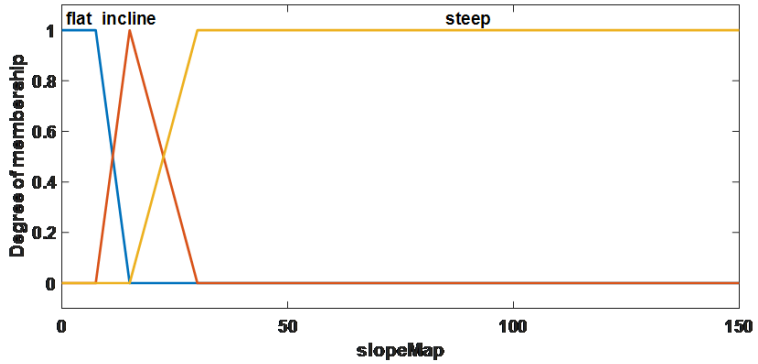

Figure 4.17: *slopeMap* membership function: maximum roughness is set to 30 degrees, and design points are defined as $\delta/2$ and $\delta/4$ of the parameter

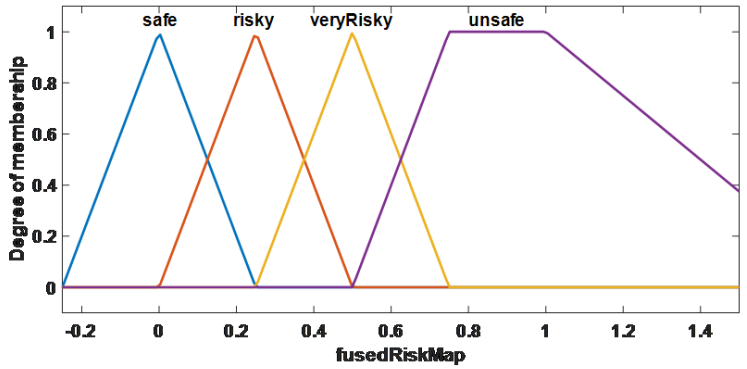

Figure 4.18: *fusedRiskMap* membership function: unsafe score is set to 80% and design points are defined by the user

The fusion rules are summarized in the table 4.7, and nine rules are obtained. Once the fuzzy set is obtained, the results are encoded into a LUT.

riskMap / *slopeMap*	Flat	Incline	Steep
Smooth	Safe	Risky	Unsafe
Rough	Risky	Very Risky	Unsafe
Very Rough	Unsafe	Unsafe	Unsafe

Table 4.7: Pre-fusion fuzzy logic rules

Finally, two additional criteria are integrated into fuzzy reasoning:

1. if a point is not compliant with any of the landing requirements, the point is labeled as unsafe
2. If all the criteria are safely verified, the point is labeled safe.

A sample LUT is presented in Figure 4.19 where it is shown that given a *slopeMap* and a *riskMap* value, the *fusedRiskMap* index is obtained.

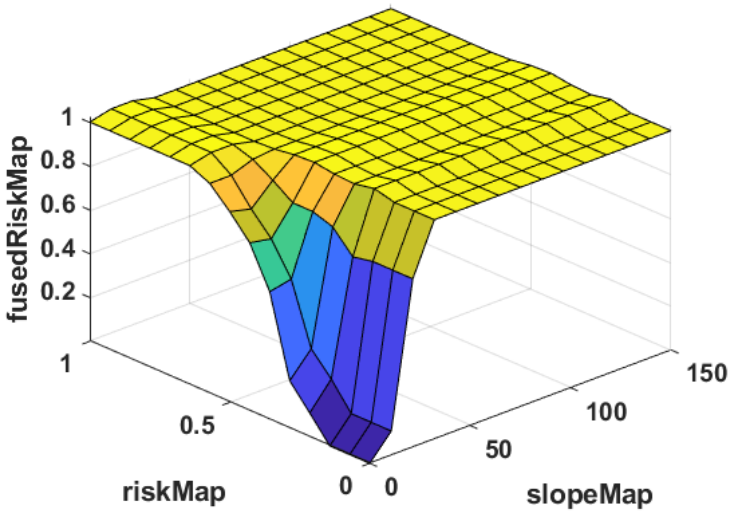

Figure 4.19: *fusedRiskMap* LUT: resulting score from riskMap and slopeMap fusion, illuMap, and distMap condition are checked at pre-fusion input.

4.4.6 Proximity

Input	Type	Output	Type	Parameter	Name
Fused Risk Map	Double [512x512]	Keep-out Map	Double [512x512]	Distance from unsafe area	β

Table 4.8: *keepOutMap* interface definition

The keep-out map takes the *fusedRiskMap* resulting from the pre-fusion block and processes it to label the area too close to a hazard as unsafe. The user has to input only the minimum distance from the unsafe area. A Euclidean distance transform is applied [154], and the map labels each

pixel with the Euclidean distance to the nearest obstacle pixel as shown in the simplified sketch in Figure 4.20; a sample map is presented in Figure 4.21.

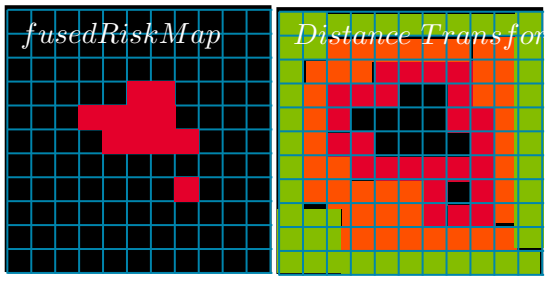

Figure 4.20: Distance Tranform Diagram

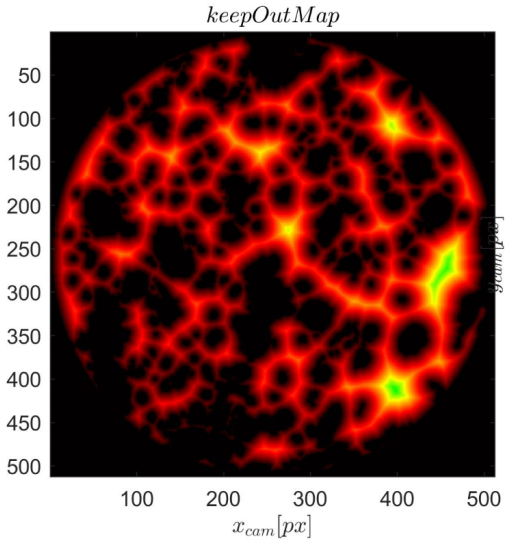

Figure 4.21: *keepOutMap* example: red are unsafe areas, green is the distance from the hazard.

4.4.7 Final Fusion Map

Input	Type	Output	Type	Parameter	Name
Fused Risk Map, Keep-out Map, Reachability Map	Double [512x512]	Final Risk Map	Double [512x512]	Maximum Distance from Nominal Landing Site Distance from the unsafe area	β α

Table 4.9: *finalRiskMap* interface definition

The *finalRiskMap* combines the previously mentioned maps by considering the hazard requirements, the reachability, and the distance from the hazardous areas. The fusion implementation uses a multi-dimensional look-up-table (LUT) approach. Thirty-six fuzzy rules are defined to fuse the maps (see Table 4.10), and a multi-dimensional fuzzy function is obtained. This function is encoded in a LUT.

finalRiskMap	*distMap*	AND	*keepOutMap*	AND	*fusedRiskMap*
Unsafe	Large		Far		Safe
Unsafe	Large		Far		Risky
Unsafe	Large		Far		Very Risky
Unsafe	Large		Far		Unsafe
Unsafe	Small		Far		Unsafe
Unsafe	Medium		Far		Unsafe
Unsafe	Large		Close		Safe
Unsafe	Large		Close		Risky
Unsafe	Large		Close		Very Risky
Unsafe	Large		Close		Unsafe
Unsafe	Small		Very Close		Safe
Unsafe	Small		Very Close		Risky
Unsafe	Small		Very Close		Very Risky
Unsafe	Small		Very Close		Unsafe
Unsafe	Medium		Very Close		Safe
Unsafe	Medium		Very Close		Risky
Unsafe	Medium		Very Close		Very Risky
Unsafe	Medium		Very Close		Unsafe
Unsafe	Large		Very Close		Safe
Unsafe	Large		Very Close		Risky
Unsafe	Large		Very Close		Very Risky
Unsafe	Large		Very Close		Unsafe
Safe	Small		Far		Safe
Risky	Small		Far		Risky
Very Risky	Small		Far		Very Risky
Risky	Medium		Far		Safe
Very Risky	Medium		Far		Risky
Very Risky	Medium		Far		Very Risky
Risky	Small		Close		Safe
Very Risky	Small		Close		Risky
Very Risky	Small		Close		Very Risky
Very Risky	Medium		Close		Safe
Very Risky	Medium		Close		Risky
Very Risky	Medium		Close		Very Risky
Unsafe	Small		Close		Unsafe
Unsafe	Medium		Close		Unsafe

Table 4.10: *finalRiskMap* LUT Rules

The *fusedRiskMap* values are classified into four classes as for the pre-fusion: safe, risky, very risky, and unsafe. The *distMap* values are classified into three categories: small, medium, and large diversion. The *keepOutMap* is classified according to three values: very close (to obstacle), close,

and far.

The class definition is established given the parameters provided by the requirements. The *distMap* membership function design points are defined as α, 2α, 3α. The *keepOutMap* membership function design points are linked to the requirement parameter as β, 2β, 3β see Table 4.13 for parameters definition.

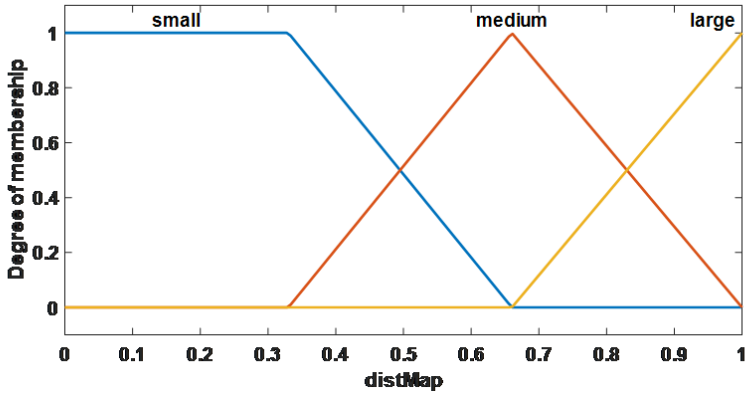

Figure 4.22: distMap membership function: set point are α, 2α, 3α

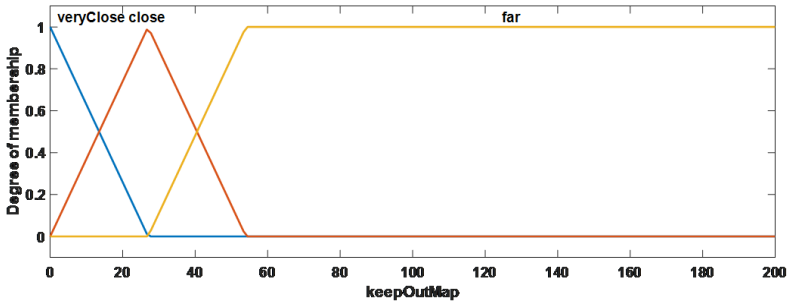

Figure 4.23: keepOut map membership function: set point are β, 2β, 3β

Once the *fusedRiskMap*, *distMap*, and *keepOutMap* are fused according to the fuzzy logic defined rules, the resulting fused pixel can belong to four classes: safe, risky, very risky, and unsafe. These classes are de-fuzzified according to the same pre-fusion membership function to obtain the *fusedRiskMap* value between 0 and 1, as shown in Figure 4.18. The unsafe area is increased to make the overall algorithm more conservative. In Figure 4.24, a sample *finalRiskMap* is displayed; every valid pixel represents possible landing requirements; in fact, it verifies the landing safety requirements after the fusions. Each pixel has a safety index (green is safe and red is unsafe) on which the landing site logic assesses the target landing site.

4.4.8 Assessment and Logic

The presented workflow is run at a fixed distance from the surface at a specific gate as in Section 2.2.5. The final logic can be resumed in the Algorithm 3. The logic can be applied to more than one landing site if needed.

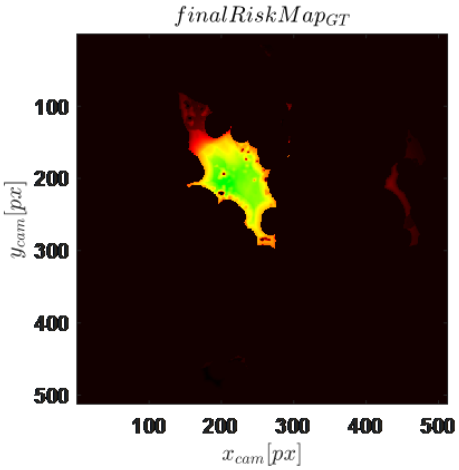

Figure 4.24: *finalRiskMap* example at 300m: green is safe, red is unsafe.

Algorithm 3 Safe Landing Site Logic

1: Evaluate $finalRiskMap(\bar{\mathbf{f}})$. ▷ Evaluate *finalRiskMap* at nominal landing site $\bar{\mathbf{f}}$ decided by operation/ ground operators.
2: Minimize *finalRiskMap*. ▷ Select global minimum for *finalRiskMap* namely located in $\mathbf{f}^*$.
3: **if** $finalRiskMap(\bar{\mathbf{f}}) - finalRiskMap(\mathbf{f}^*) \leq \epsilon$ **then** ▷ ϵ is a design decision threshold
4: Retarget to $\mathbf{f}^*$
5: **else**
6: Proceed to $\bar{\mathbf{f}}$
7: **end if**

4.5 Deep Learning Developments

The current section focuses on segmenting boulders from the surface images and building a hazard map containing the detected hazards to produce the *hazMap*. Firstly, the synthetic dataset generation workflow is explained, then, the supervised learning architectures trade-offs and results are introduced. Finally, the post-processing of the selected network is described, and the verification results on authentic mission images are presented. The process summary is shown in Figure 4.25.

4.5.1 Dataset Generation

In this section, the dataset generation workflow is presented. Firstly, the procedure for synthetic environment modeling is shown, then, the trajectory generation and environment randomization is discussed.

Dataset Modelling

Supervised-learning paradigms use a representative environment dataset in which the algorithms are deployed [155]. In this case, the dataset includes RGB images generated according to the on-board camera specification as in Section B.4, and labeled images that contain the boulders extracted from the images, i.e., binary images that show masked boulders up to image resolution.

The dataset is generated synthetically because of three main limitations:

1. The limited number of available real images from missions that featured vision-based naviga-

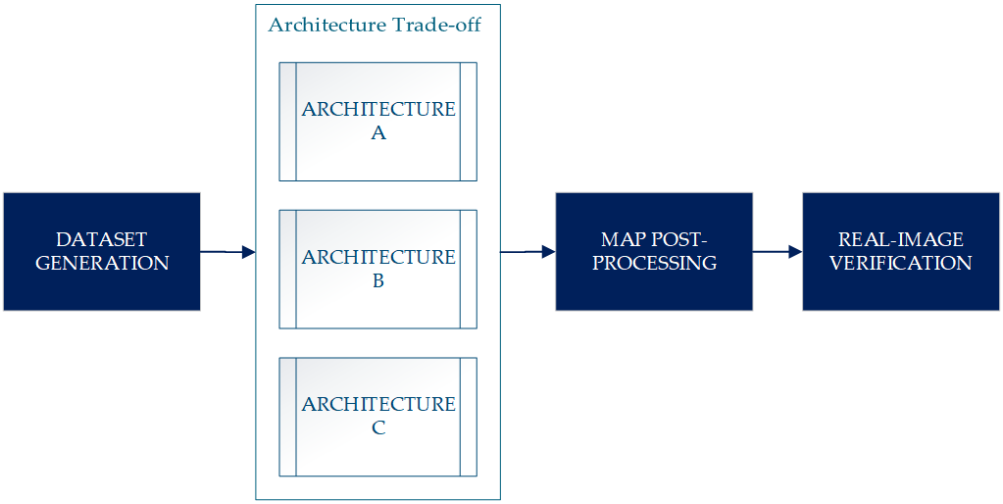

Figure 4.25: Process Summary from Dataset Generation to Verification

tion and camera specifications similar to those in the table.

2. The exact labeling process is usually done manually, it is very time-consuming, and the annotation is imprecise.

3. To the best of the authors' knowledge, there is no open source SSSBs landing dataset currently available.

To model Dimorphos, the available ESA/Jet Propulsion Laboratory (JPL) shape model is used, and the complete environment modeling description is presented in Section 3.3. This step allows increased base surface resolution to match Dimorphos mass properties (i.e., MoI); the rescaling factors are shown in Table 3.3. The PANGU software [112] also provides for each RGB image the corresponding masked boulder image, which is precisely the labeled data on which the neural networks are trained.

Trajectory Generation

The landing images are generated during a set of trajectories with different illumination scenarios and boulder distributions to avoid over-fitting the model to a specific test scenario.

The landing trajectories are generated using a quadratic open loop path from a set of initial conditions, landing sites, and time-to-go. The guidance acceleration is defined as:

$$\mathbf{a}(t) = \mathbf{C}_0 + \mathbf{C}_1 t + \mathbf{C}_2 t^2 \tag{4.5}$$

where $C_i \in \Re^3$ are coefficient determined once the boundary conditions are set. Assuming a constant gravity acceleration and integrating the acceleration, the trajectory is obtained as follows:

$$\mathbf{r}(t) = \mathbf{r}_0 + \mathbf{v}_0 t + \frac{1}{2}\left(\mathbf{C}_0 + \mathbf{g}\right) t^2 + \frac{1}{6}\mathbf{C}_1 t^3 + \frac{1}{12}\mathbf{C}_2 t^4 \tag{4.6}$$

The minimum height considered is 2 m because no hazard detection is expected to happen below that threshold. According to the mission concept of operation and assuming an average descent velocity of 6 cm/s, the descent duration is specified as 1800 s.

In addition to decreasing the possibility of over-fitting, the Sun azimuth and elevation are distributed from 0 to 60 degrees to consider diverse illumination conditions. Finally, the boulders are located according to different random seeds. The envelopes of the former environmental and dynamic conditions (i.e., lander positions) generate around 43000 RGB images and corresponding labels, i.e., binary mask, which precisely identifies all the added boulders.

The images are selected to represent samples every 5 s along the trajectory. In conclusion, the dataset is shuffled and randomly divided into training (81%), validation (9%), and test set (10%). The training set is used to fit the model's parameters (e.g., weight and biases of the networks), and the validation set allows us to evaluate the fit model and tune the network's hyper-parameters (e.g., architecture, layers type, etc.). Finally, the test set is used to assess the final performance of a network. After the training and the tuning, the model accuracy is assessed.

4.5.2 Neural Networks Architecture

The problem of boulders detection is identified as binary semantic segmentation; this formulation implies that the likelihood of being a hazard for each pixel is estimated. Thus, semantic segmentation consists of dense, i.e., pixel-wise predictions inferring labels for every pixel; in this case, the label is the boulder/not-boulder binary class. A set of convolutional neural networks (*Convolutional Neural Network (CNN)*) is selected for the task; their performance is compared according to accuracy metrics, complexity, and execution time.

4.5.3 Optimal Framework Selection

A collection of neural network architectures is trained on the present problem; the architectures are selected according to current state-of-the-art surveys for semantic segmentation [156]. They are presented and investigated according to increased network complexity. The simpler network architecture consists of a Fully Convolutional Network (*Fully Connected Network (FCN)*) [157]; the general architecture is composed of a few convolutional and pooling layers followed by fully connected layers at the output. The most common issue for *FCN* is that by propagating through several alternated convolutional and pooling layers, the resolution of the output feature maps is downsampled. The *FCN* is a base approach not addressed in the study.

Segnet [150] comprises an encoder network and a corresponding decoder network followed by a pixel-wise classification layer. The architecture of the encoder network is structurally identical to the most common *FCN* (VGG16). The role of the decoder network is to map the low-resolution encoder features maps to full input resolution feature maps for pixel-wise classification, i.e., input resolution is preserved in the output. The novelty of *Segnet* is the up-sampling of the lower-resolution input feature map in the decoder. Specifically, the decoder uses pooling indices computed in the max-pooling step of the corresponding encoder to perform non-linear up-sampling. The network does not learn to up-sample but derives the parameters from the encoder. Finally, the up-sampled maps are sparse and convoluted with trainable filters to produce dense feature maps.

Shortcut connections are the main contribution of the *U-net* [5] architecture. In FCN, the image is down-sampled as part of the encoder. Consequently, information is lost and cannot be quickly recovered in the decoder part. FCN addresses this by taking information from pooling layers before the final feature layer.

U-net proposes to send information to every up-sampling layer in the decoder from the corresponding down-sampling layer in the encoder, as shown in Figure 4.26. Capturing finer information also keeps the computation low. Since the layers at the beginning of the encoder would have more information, they would support the up-sampling operation of the decoder by providing small details corresponding to the input image, thus improving the accuracy.

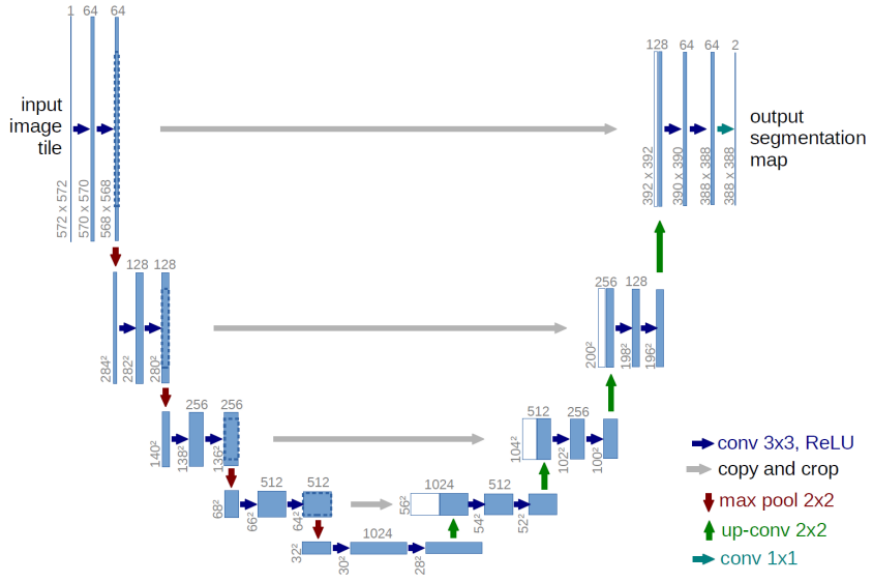

Figure 4.26: *U-net* architecture adapted from [5]

ResNet [158] uses a skip connection in which an original input is also added to the convolution block output, which is implemented via the residual block. This mitigates vanishing gradient problems by allowing a different path for the gradient to propagate. In traditional neural networks, each layer feeds into the next layer. But in a network with residual blocks, each layer feeds into the next layer and directly into the layers about some steps away, as shown in Figure 4.27.

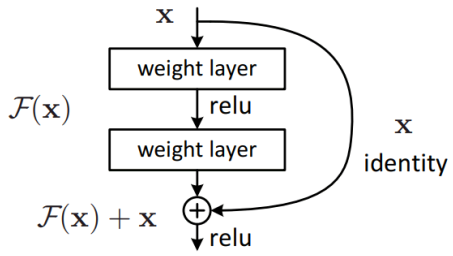

Figure 4.27: *ResNet* residual block architecture adapted from [6]

PSPNet [159] is one of the most well-recognized image segmentation algorithms. The model was introduced because FCN based pixel classifiers could not capture the overall context of the whole image. The *PSPNet* architecture considers the global context of the image to predict the local level predictions using a pyramid pooling module. The feature map from the backbone, i.e., the input *CNN*, is pooled at different sizes and then passed through a convolution layer, as presented in Figure 94. Then up-sampling takes place on the pooled features to make them the same size as the original feature map. Finally, the up-sampled maps are concatenated with the original feature map to be passed to the decoder. This technique fuses the different scales of the features, hence

aggregating the contextual meaning of the image.

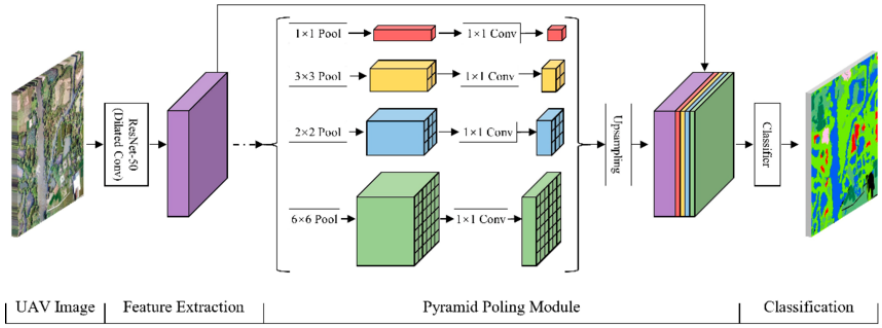

Figure 4.28: *PSPNet* architecture adapted from [7]

Lastly, a combination of U-net with Convolutional Long-Short-Term-Memory *(C-LSTM)* Block is used. The *C-LSTM* block allows incorporating spatial-temporal information by introducing a memory block in every scale of the encoder section [160]. Applying it to different scales allows for saving information on varying scales of the boulders. The ability to store temporal information could increase segmentation accuracy. The frame-to-frame difference could be used to track the same boulders and refine single-image hazard detection.

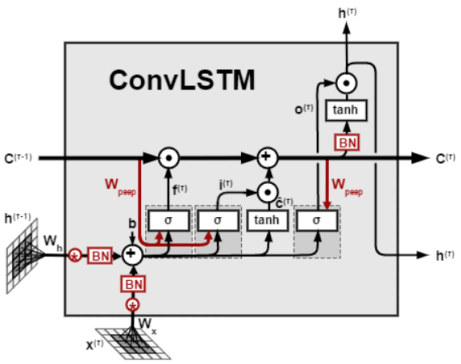

Figure 4.29: C-LSTM cell adapted from [8]

The same loss function is optimized in each training, which is the binary cross-entropy defined as:

$$Loss = -\frac{1}{output\ size} \sum_{i=1}^{output\ size} (y_i \cdot log(\hat{y}_i) + (1 - y_i) \cdot log(1 - \hat{y}_i)) \tag{4.7}$$

The previous equation represents the standard loss function for binary segmentation task, the hat variables represent the neural network prediction, while the y_i is the ground truth value. Finally, the architectures are trained on the dataset divided into training, validation, and test sets on a cloud platform with a 16 GB Tesla V100 GPU.

Results and Final Selection

To compare the different network's results, two main criteria are applied. Firstly, the quantitative metric is accuracy, defined as:

$$Accuracy = \frac{TP + FN}{TP + TN + FN + FP} \tag{4.8}$$

Here $TP, TN, FP, and FN$ are True Positive, True Negative, False Positive, and False Negative, respectively. The accuracy is a valid metric since the classification problem is well-balanced and not skewed. The second criterion for the architecture trade-off is the qualitative visual analysis of the neural network prediction. In particular, some test images are sampled, and the predicted hazard map is visually analyzed. The focus is on the prediction in well-lit conditions and very scarce illumination scenarios.

In Table 4.11, the results of the training are presented. Most architectures converge on similar values for the loss function, i.e., binary cross-entropy. Thus they can fit the ground truth. *Segnet* represents an exception; the loss function after ten epochs stays relatively high. The *U-net + C-LSTM* implementation by integrating three frames has the highest accuracy. However, the increase in complexity with reference to the classical *U-net* may not motivate the use of such architecture. It is also underlined that the *U-net + C-LSTM* with the four frames implementation is less accurate. The cause of such behavior could be linked to the temporal distance between frames being too large. In fact, given the sample time of 5 seconds, there is a temporal distance of 20 seconds from the first frame to the last. This represents an extensive modification of the images and results in issues in incorporating the changes in the memory block.

ResNet and *PSPNet* have a high accuracy. However, they are deeper and more complex than the *U-net*. Convergence is another index considered for the trade-off; the convergence number is the epoch when the loss function is not decreasing after three epochs. Consequently, the training process is stopped. It is noted that *ResNet*, *Segnet* and *U-net + C-LSTM* (4 frames) converge faster. Hence the training process is finished in fewer epochs than the other architectures.

Architecture	Accuracy [%]	Loss [%]	Convergence [Epoch]
U-net	97.08	6.53	20
ResNet	97.01	6.61	10
Segnet	90.48	21.32	10
PSPNet	97.00	6.90	16
U-net+C-LSTM (3 frames)	97.11	6.52	19
U-net+C-LSTM (4 frames)	95.96	8.91	10

Table 4.11: Neural network architecture training results

In Figure 4.30, some sample images are presented for the *U-net* architecture; it is underlined how the false positives and false negatives occur exclusively around the boulder contours. The shadows contain the most misclassified pixels. However, since they are confined to the contours, they can be easily avoided by targeting a landing point further from the boulders. The false negatives are the most critical error: no boulder is detected on the pixel when there is one. The power of the machine learning-based approach is highlighted in the low-illuminated image (Figure 4.31). In low

illumination, the neural network can correctly identify the boulders in the shaded area. It is noted that the prediction value for the *U-net* provides a value from 0 to 1, where 1 is 100% probability of finding a boulder, and 0 is no probability of boulders. The processing time on the hardware is between 3 and 40 *ms* for each frame.

In conclusion, the *U-net* architecture is selected to implement the hazard map estimator. It provides high accuracy and light implementation, which makes it suitable for onboard applications. A more extended convergence than other architectures is insignificant since the network is trained offline on the ground without time constraints.

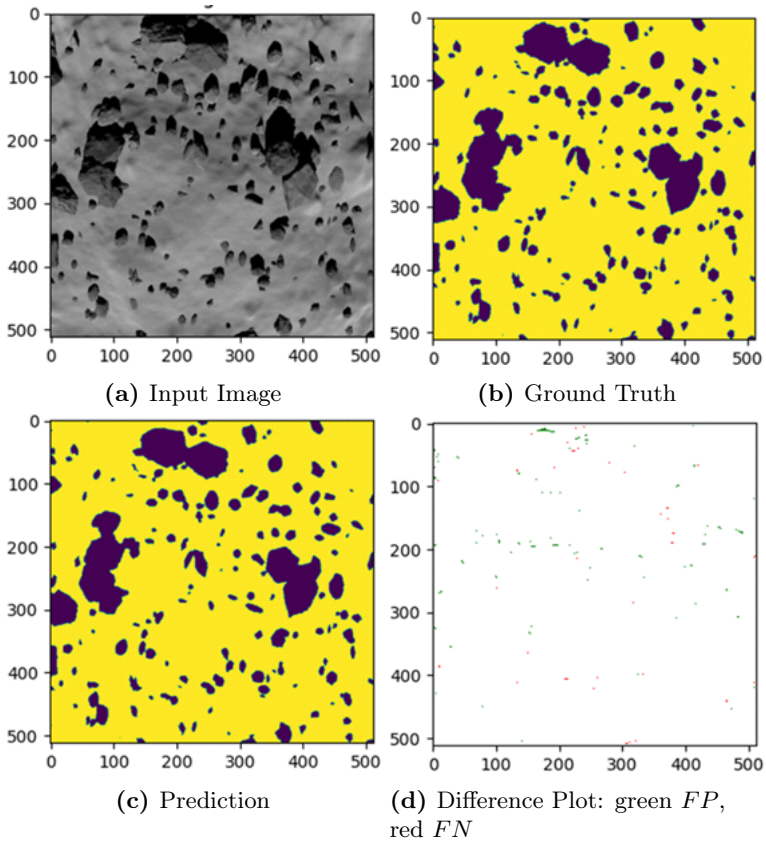

(a) Input Image **(b)** Ground Truth

(c) Prediction **(d)** Difference Plot: green FP, red FN

Figure 4.30: *U-net* Results

4.5.4 Map Fusion Example

In the present section, an example of simplified data fusion is presented. Different criteria are fused in the final safe landing map (e.g., slope, roughness, illumination, accessibility, etc.), as shown in Section 4.3. Here, the *riskMap* is fused with a simplified *illuMap* to highlight the contribution of the *hazMap* to the simplified *finalRiskMap*. The sample safe landing map only includes Risk Map and Illumination Map for explanation purposes; the other criteria are introduced in the previous section.

The simplified Illumination Map is generated by applying a threshold to the RGB image to detect all the pixels above a fixed intensity. After applying a threshold to the image, each pixel's local illumination density is evaluated, following the process used for the *riskMap* generation. The *riskMap* and the *illuMap* are fused according to the same safety parameter. Binary logic is used; the pixel is considered safe if the local rock density (i.e., the risk map pixel value) is smaller than

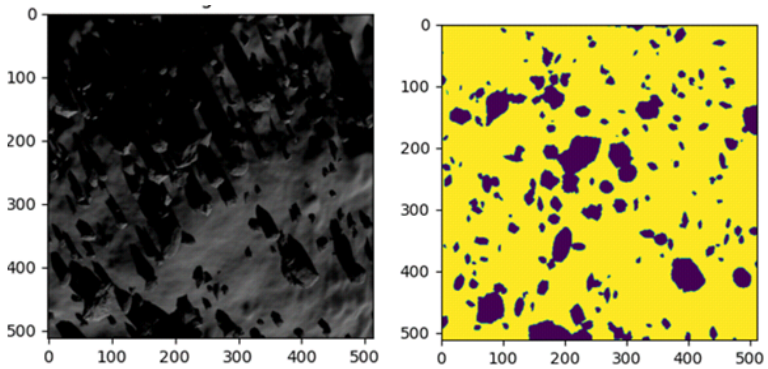

(a) Input Image

(b) Ground Truth

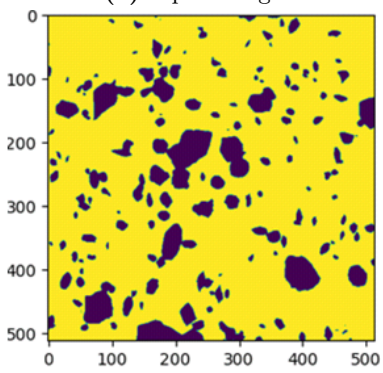

(c) Prediction

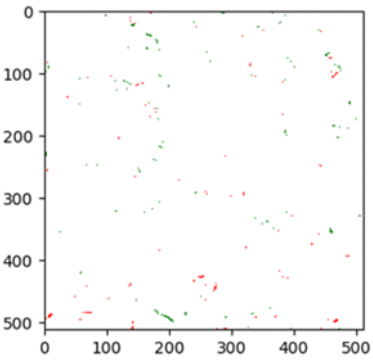

(d) Difference Plot: green FP, red FN

Figure 4.31: *U-net* Results Dark Scenario

the safety parameter. On the other hand, if the local illumination density (i.e., the illumination map pixel value) is greater than the safety parameter, the pixel is safe. If a pixel is considered safe for both the risk map and the illumination map, the fusion is a safe pixel; for any other case (e.g., unsafe and unsafe, unsafe and safe), the pixel is considered unsafe.

As expected, Figure 4.32 shows as safe landing site areas change according to the safety parameter value. Higher values imply more conservative criteria fusion and less safe landing site area; however, the safe landing site area increases with a lower value. From the image is also visible the added value of information, in terms of boulder detection accuracy provided by the network. The orange areas represent the neural network-detected boulders that are not detected in the illumination map; on the contrary, the light orange zone represents the shadow detected in the illumination map but not in the risk map. The latter proves that the hazard detection neural network can identify the boulders correctly and not the shadows. Then it is possible to classify the shadows and the boulders with high accuracy separately. Most current techniques for boulders detection are based on shadow analysis, and they are not based on the classification of the boulder semantic; in this example is underlined how the boulder information is extracted, and it is not confused with the shadow semantic.

If the safe landing site map is overlaid on the real image is possible to identify that some boulders are considered safe landing sites, as in Figure 4.33. In fact, due to the averaging operation according to the estimated landing footprint, it is possible to neglect boulders that are smaller than the footprint. In addition, the neighborhood of a big (with reference to the footprint) boulders cluster is considered unsafe because during the averaging operation, the local risk density spill over

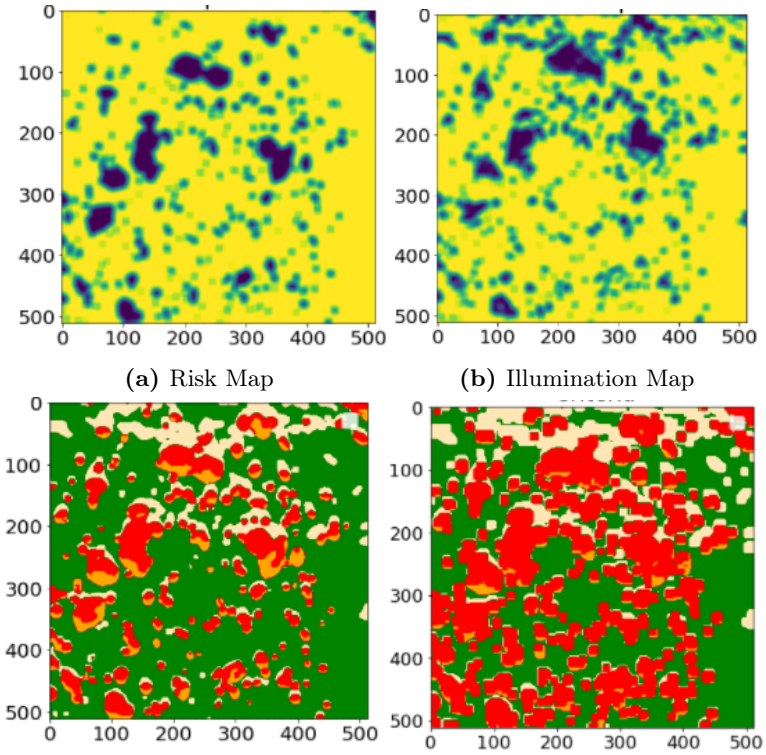

(a) Risk Map

(b) Illumination Map

(c) Safety Map fusion with 0.50 safety parameter

(d) Safety Map fusion with 0.99 safety parameter

Figure 4.32: Safety Map and Inputs for synthetic images

to the region; the latter increases the conservativeness of the approach.

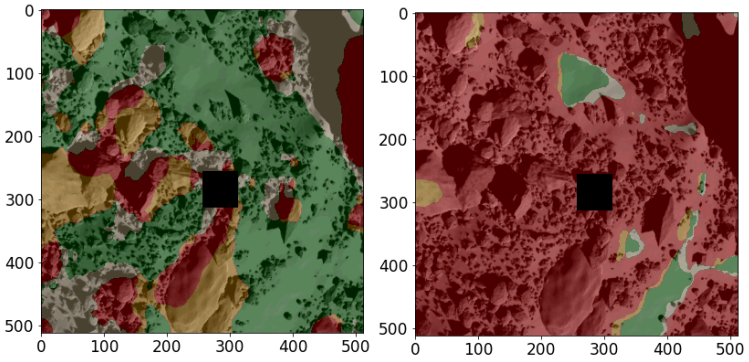

(a) Safety parameter 0.50

(b) Safety parameter 0.99

Figure 4.33: Safety Map and Original at 22.5 m from the surface: the black square is the estimated lander footprint

Finally, it is highlighted in Figure 4.33 how different safety parameters can have other resulting safe landing site areas; the final selection of the safety parameter can be executed by weighting the different safe landing criteria and the available landing site.

It is also possible to adapt dynamically the safety parameter for each subsequent safe landing site assessment. This would allow for finding the safest landing site rather than finding all landing sites. Other criteria are introduced in the final Safety Map, such as slope, roughness, and reachability. The latter is linked to fuel consumption; a fuel-optimal landing site is preferred. In conclusion, it is possible to select the best landing site by fusing all the criteria and by re-tuning the safety

parameter for each of them.

4.5.5 Real Mission Images Validation

The workflow presented in the previous section is applied to real mission images from the Rosetta mission. The mission represents the general SSSB environment and allows a comparison with classical image processing algorithms.

The Rosetta spacecraft carried a Navigation Camera (*NavCam*) for optical navigation in the vicinity of the comet [161]. Similar environmental and geometrical conditions to the dataset must be selected to validate the hazard detection workflow. Rosetta images have a resolution of 1024 px × 1024 px; as a consequence, cropping is needed to reduce by half the image size. Moreover, the crop operation does not alter the original image signal, but the equivalent distance from the surface is halved.

Equivalence is established to convert Rosetta acquisition conditions (i.e., surface distance, field of view, etc.) into the current scenario, given the fact that *NavCam* has 5° FOV and the chosen camera 30° FOV. The closest Rosetta images are taken at approximately 3 km from the surface; after cropping, the equivalent distance is about 1.5 km, with 5° FOV the resolution is $0.25m/pixel$. To obtain the exact resolution of the selected camera, the equivalent distance from the surface is approximately 240 m, which is within the current scenario condition, and it is the distance used for footprint estimation.

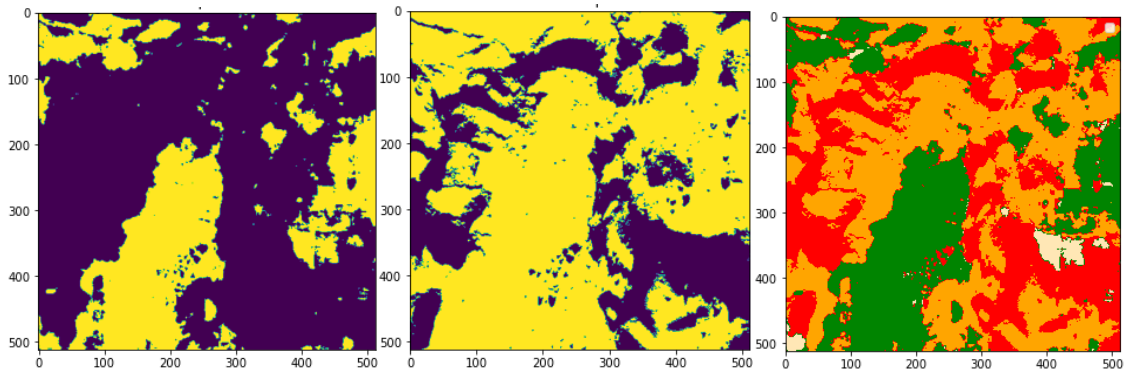

(a) Risk Map **(b)** Illumination Map **(c)** Safety Map fusion with 0.99 safety parameter

Figure 4.34: Safety Map and Inputs for Rosetta sequence

In Figure 4.34, the output of the Risk Map and Illumination Map is shown for a sample image of the selected Rosetta sequence (i.e., post-landing mission phase *MTP034*). It is highlighted that neural network prediction contributes to detecting unsafe landing regions close to the ridges and the cliffs. At the same time, the Illumination Map is able to detect only unsafe shaded areas. Both criteria provide complementary information.

The criteria are fused using a 0.99 safety parameter; it is possible to use extremely high safety parameters further from the surface, i.e., in the initial hazard detection routines, while being less conservative as the lander approaches because higher altitude values mitigate the risk. In Figure 4.35, the final Safety Map is overlaid on the real image, and the hazard detection workflow correctly identifies the central planar valley and some clearings above the cliffs as a safe area. Finally, by introducing other criteria (e.g., slope, roughness, and landing site reachability), it is possible to

refine the selected landing zones to further increase the landing site safety.

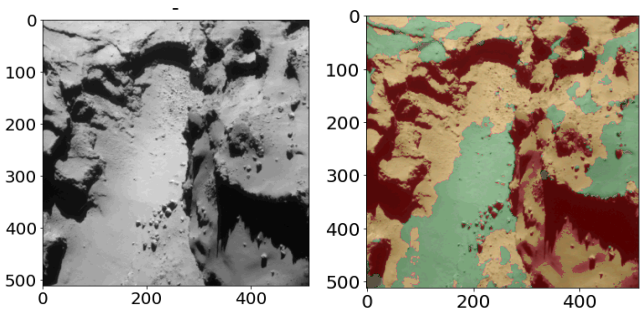

(a) Input Image **(b)** Safety Map Overlaid

Figure 4.35: Safety Map at 244 m (equivalent) from the surface with 0.99 safety parameter

Validation Outlook

In conclusion, landing on SSSB requires lander autonomy and robustness. To improve autonomous landing site selection, supervised learning strategies are introduced into the hazard detection functionality to improve autonomous landing site selection. *U-net* neural network architecture is selected between the state–of–the–art semantic segmentation neural networks as the optimal architecture for hazard detection in terms of accuracy, simplicity, and execution speed. The architecture accurately detects the boulders without tuning many parameters and long processing times. The Hazard Map obtained is post-processed to incorporate the prediction probability and the surface distance to increase the safety of the Risk Map. The network prediction is robust against various illumination conditions, and the algorithms are applied to real mission images to validate the results qualitatively. The approach presented here is part of the safe landing site assessment functionality, and it incorporates only the illumination and boulders detection criteria.

4.6 Analysis and Performances

4.6.1 Simulation Environment

The functionalities are implemented into *MATLAB/Simulink 2021b*. Most of the functions run into this environment; however, some of them run on *Python* compiler, and most of the map creation is done using *OpenCV* [152] and *Tensorflow* [162]. The SLSS is a triggered block with inputs: LRF measurement, RGB image, and nominal landing site coordinates in the camera reference frame. SLSS outputs are the safety of the target landing site coordinate and the target landing site position in the camera reference frame. The pose estimation derived from the navigation filter (LAPNAV) converts the camera reference frame to the landing frame.

Some functions are not native *MATLAB* code and use specific *Python* packages. In particular, most of the map creation is done using *OpenCV 4.6.0* and *Tensorflow 2.10.0*. In future development, non-native code should be implemented into Matlab or optimized into C-coding. Table 4.12 shows the different dependencies linked to each function.

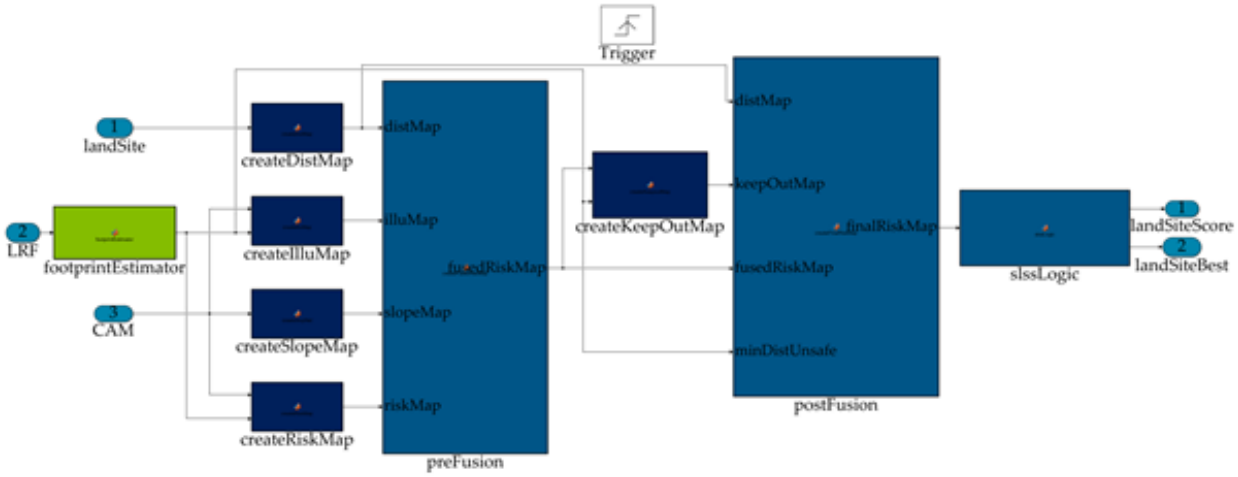

Figure 4.36: Safe Landing *Simulink* Block

Function	*MatLab* Native	Extrinsic	*Python*	*OpenCV*	*Tensorflow*
`fooprintEstimator`	✓				
`createDistMap`		✓	✓		
`createIlluMap`	✓	✓	✓	✓	
`createSlopeNet`		✓	✓	✓	✓
`createRiskMap`		✓	✓	✓	✓
`preFusion`	✓				
`createKeepOutMap`		✓	✓	✓	✓
`postFusion`	✓				
`slssLogic`	✓				

Table 4.12: Function Programming

4.6.2 Parametrization

The SLSS is designed to have the minimum number of parameters possible; moreover, the architecture is designed to link most of these parameters to the landing requirements set by the user. Each parameter is detailed in Table 4.13, and the corresponding requirement is presented.

Parameter	Symbol	Description	Unit	Note	Req.
`decisionThreshold`	ϵ	Minimum safety distance to decide for retargeting	-	Tunable	-
`minDistUnsafe`	β	Minimum distance from an unsafe landing site	Pixel	The conversion from metric to pixel is done in the pre-processing of block	✓
`maxDivert`	3α	Maximum retargeting distance from target landing site	Pixel	Conversion from metric to pixel is done in the pre-processing block.	✓
`maxRoughDens`	γ	Maximum local rock density	%	Fixed in the requirement	✓
`maxSlope`	δ	Maximum allowed slope	degree	Fixed in the requirement	✓
`shadowToll`	η	Binary thresholding parameter	-	Tunable	-

Table 4.13: SLSS Parameters

The `decisionThreshold` and `shadowToll` are tunable parameters that can be set after sensitivity analysis. In particular, the study should consider the available prior knowledge of the environment and the landing operations scenario.

4.6.3 Execution Time

In this section, the average execution time for the most critical functionalities is presented (Table 4.14). All the pre-fusion maps creation can run in parallel; the maps that take most of the time are the *slopeMap* and *riskMap*. Both of them have multiple function calls and run U-net-based neural networks. These modes can be improved, and the network can be optimized for onboard execution: the network evaluation can run in parallel on Field Programmable Gate Array (FPGA) for example [163].

Function	Time	Parallel
distMap	18 ms	✓
illuMap	14 ms	✓
slopeMap	1.5 s	✓

riskMap	1.2 s	✓
Pre-fusion	30 s (expected $<$ 2 s)	-
keepOutMap	10 ms	-
Post-fusion	6 s (expected $<$ 2 s)	-
Logic	35 ms	-

Table 4.14: Function Average Execution Time

Pre-fusion map is slow because it has not been optimized using a LUT; once the final parameter set has been decided, the fuzzy logic rules will be encoded into the LUT format, that is, the expected execution time in Table 49. For the post-fusion, the same consideration is valid; however, this map is faster because fewer points are evaluated. Overall a call requires approximately 40 s. However, the fusion functions are not optimized, and a total time of less than 10 s is expected. Given the slow environmental dynamics and the altitude at which it is run, this execution time is not critical for the specific mission scenario.

4.6.4 Monte Carlo Analysis Performances

A Monte Carlo test campaign is run to derive the complete system performance of the SLSS. SLSS is tested on 600 different images, which are generated by distributing environment and spacecraft states. In particular, the Sun azimuth, elevation, trajectory end condition, and boulder distribution are varied according to Table 4.15. The landing sites are 20 m above the surface, as no routine occurs below that altitude. The predicted *finalRiskMap* is compared with a ground truth; the latter uses the pipeline having as an input the actual *slopeMap* and *hazMap*.

	Sun Azimuth	Sun Elevation	Landing Site	Boulder Seed
Value	$[20, 45, 60]^\circ$	$[15, 30, 45]^\circ$	alpha, bravo , charlie	[1,2]

Table 4.15: Monte Carlo Parameters Distribution

The performance error is defined as:

$$\Delta F = F_{GT}(\mathbf{f}^*) - F(\mathbf{f}^*) \tag{4.9}$$

where F_{GT}, F is respectively the ground truth and predicted *finalRiskMap* value and $\mathbf{f}^*$ is the target landing site selected location. In Figure 4.37, a cumulated histogram is presented to show the error between predicted and ground truth *finalRiskMap*: it is shown that more than 90% of the samples have a negative error, which means that the predicted risk map is more conservative than the real ground truth (green area). In this case, the solution estimates a more significant risk than the actual one. However, these false negatives are not mission-critical.

False positives are the points for which the error is positive, and they represent less than 10% of the samples (red area). In some limits cases, the error may increase mainly due to the high sun

phase angle; this situation is avoided by mission analysis on the ground. The false positive amount represents an acceptable value for the NEO-MAPP mission, and it is believed that in a complete GNC closed-loop testing, this value can be further reduced because successive runs will observe previously selected safe landing sites.

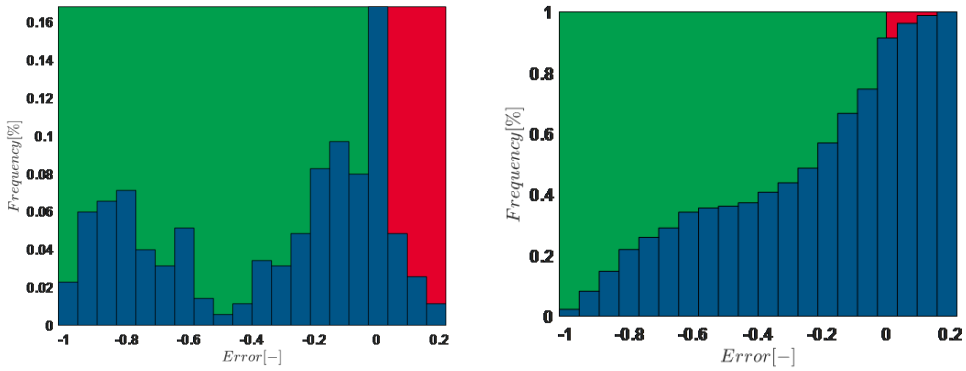

(a) Histogram **(b)** Cumulative histogram

Figure 4.37: *finalRiskMap* error predicted vs. ground truth: false positive (red) and false negative (green)

In Figure 4.38, the mean absolute error and standard deviation between final risk maps are shown: the mean error is always below 6 % for all the data points; these statistics consider a mean and a standard deviation over the entire maps on not only on the target landing site as shown previously as:

$$\bar{\Delta F} = E\{F_{GT}(\mathbf{f}^*) - F(\mathbf{f}^*)\} \tag{4.10}$$

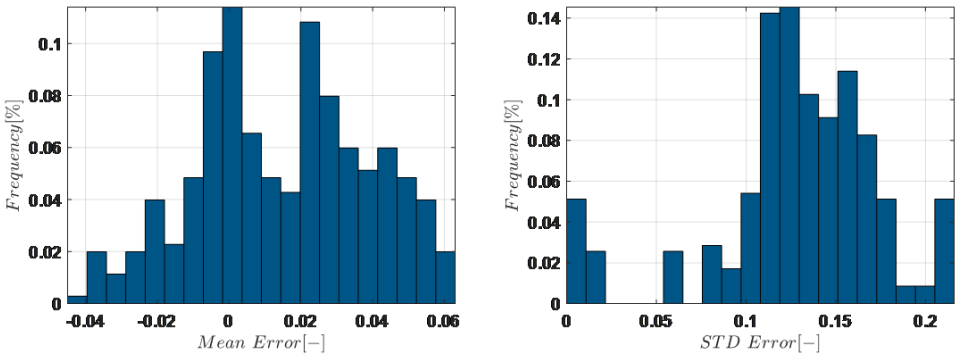

(a) Mean error **(b)** Standard deviation

Figure 4.38: Histogram on finalRiskMap predicted vs. ground truth

In conclusion, Figure 4.39 displays the cumulative histogram for the landing size distance. In more than 90% of the data points, the percentage difference between the target and the nominal landing sites is less than 30 %. The percentage represents the normalized pixel difference over the image resolution. This effect combines the reachability map constraint and the fusion, which sets the target landing site close to the nominal one. It is proved that the current solution tries to balance the proximity to the nominal landing site, which is of high scientific interest, with the overall safety of the lander.

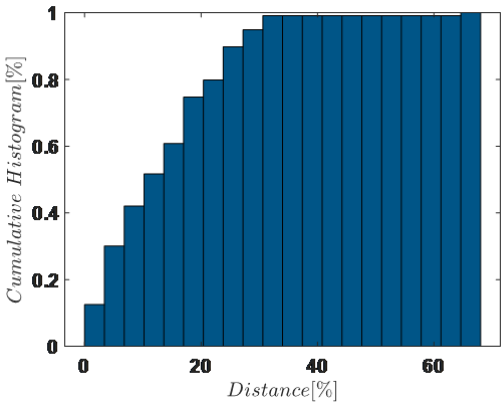

Figure 4.39: Cumulated histogram for landing site distance predicted vs. ground truth

4.7 Conclusion

This novel hazard detection and safe landing site selection framework provides a lightweight and robust solution for micro-lander autonomy. The hybrid machine learning and image processing pipeline extracts augmented information (e.g., hazards and slope) only from the camera and LRF. In this way, it completely fulfills the stringent landing requirements by limiting the mass budget (e.g., LiDAR-free). This innovative solution has few free design parameters, granting rapid tuning, and is highly parallelizable for efficient onboard implementation. Finally, its application is not limited to SSSBs surface and can also be employed on planetary landing.

Chapter 5

Conclusion

5.1 Outlook

This chapter culminates with a comprehensive summary of the substantive contributions advanced through this research, enriching our knowledge and application of autonomous technologies tailored for μLanders. Interrogating my central research questions (see Section 1.1.2), significant advancements across distinct thematic topics are found:

- LiDAR-Free Autonomous Safe Landing Site Selection Technology: the research has yielded the conceptualization, realization, and robust validation of a novel LiDAR-free autonomous safe landing site selection technology. Distinctively fusing image processing and machine learning paradigms, this innovative solution has engendered a diminution in human-in-the-loop. Remarkably, this technology integrates landing prerequisites into its operations, a feature proven by empirical validation employing authentic mission imagery [29].

- Autonomous Vision-Based Absolute Navigation System: an autonomous vision-based absolute navigation system, with a commercial off-the-shelf (COTS) camera and a laser range finder, has been implemented. This navigation system asserts its effectiveness in navigating binary asteroid environments with limited prior environmental knowledge, leveraging a rough ellipsoid shape model [1, 9, 68].

- Autonomous Vision-Based Relative Navigation System: precision navigation through an autonomous vision-based relative navigation system has been proven. Using an innovative monocular SLAM-based filter aided by altimeter measurements, this system allows precision pinpoints landings. [69, 70].

- μLander Asteroid Mission Concept: a μLander asteroid mission paradigm within the ambit of NEO-MAPP has been outlined, designed and its requirements defined. This includes problem domain definition, derivation of GNC requirements, and elaboration of a concept of operations.

The research introduces an autonomous navigation paradigm for small spacecraft within binary asteroid environments, thus extending the prior research into the efficacy of LRFs and cameras for navigation in such dynamic settings. Central to my approach is employing an extended Kalman filter featuring a 9-parameter state vector, estimating spacecraft state in an inertial reference frame. The

fusion between relative measurements and the inertial frame necessitates using asteroid ephemeris and ellipsoidal shape modeling.

The performance of the current navigation solution is tested with several influential factors, including high sun phase angles and the irregular topography of the asteroid. My findings verify the system's robustness, demonstrating successful state estimation even for irregular asteroid shapes and under high sun phase angles. Furthermore, the system's robustness is evident in its capacity to navigate under uncertainty regarding the initial state estimate effectively. The navigation solution's independence from LRF is also highlighted if optimal visibility of both asteroids is present. The filter's robustness remains solid even when subjected to distorted and noisy camera images. This success makes this navigation solution valid for medium to close-range navigation in binary asteroid environments.

For close-range navigation, a novel EKF grounded in SLAM with enhanced LOS observability is defined. A LRF substantially amplifies the system's capacity to estimate spacecraft position even when measuring scarce parallax features. These improvements grant high-precision accuracy during landing.

The EKF balances between computational efficiency and efficacy through reduced feature selection in the state. This mitigates the algorithmic computational burden, rendering it possible for onboard implementation and augments processing speed. Moreover, the robustness of the novel EKF is established through a Monte Carlo analysis for boundary conditions.

The design of a hazard detection and safe landing site selection framework to increase lander autonomy has been presented. The hybridization of machine learning and image processing provides a robust and lightweight solution that adheres to landing requirements without the constraints of LiDAR-dependency. This innovative framework presents a scarcity of free design parameters, facilitating calibration and parallelizable onboard implementation. A salient aspect is the framework's compliance with stringent mass budgets, marking a difference from traditional LiDAR-dependent approaches.

Taken together, the findings from this research present highly promising prospects for future space exploration missions. The developed autonomous navigation solutions and hazard detection framework hold considerable potential and can be effectively utilized to enhance the efficiency and reliability of space exploration missions. Their successful application extends beyond SSSBs and can also e readily adapted for planetary landing missions. This research significantly advances autonomous navigation and safe landing systems in space exploration by addressing critical challenges and providing innovative solutions.

5.1.1 Standard for Autonomy

One of the primary objective of this research can be precisely formalized as advancing the autonomy level from E2 to E3 for SSSBs lander spacecraft, aligning with the standards established by the European Cooperation for Space Standardization (ECSS) [10]. This targeted enhancement in autonomy levels reflects a significant stride towards optimizing the operational efficiency and reliability of lander spacecraft in the exploration of Small Solar System Bodies. The necessity for heightened autonomy has been previously expounded upon in Section 4.3, underscoring the critical role that autonomous capabilities play in overcoming operational challenges and ensuring the success of future space missions. In the Table 5.1 a brief description of the standard's level is presented.

Level	Description	Function
E1	Mission execution under ground control; limited on-board capability for safety issues	Real-time control from ground for nominal operations Execution of time-tagged commands for safety issues
E2	Execution of pre-planned, ground-defined, mission operations on-board	Capability to store time-based commands in an on-board scheduler
E3	Execution of adaptive mission operations on-board	Event-based autonomous operations Execution of on-board operations control procedures
E4	Execution of goal-oriented mission operations on-board	Goal-oriented mission re-planning

Table 5.1: Mission execution autonomy levels as imported from [10]

5.2 Future Work

Important questions remain unanswered by this research, which should be investigated in future studies. Here are some recommendations based on the research presented in this thesis:

- Provides processor-in-the-loop simulations to prove the applicability of the algorithms for on-board implementation
- Hardware-in-the-loop to switch simulated sensors (especially camera and LRF) for real units and demonstrate the capability on real hardware.
- Prototype a full end-to-end GNC simulation, testing the transition between different landing phases and GNC modes.
- Improve the centroid detection: The issue of overlapping asteroids needs to be solved to increase the deployability of the navigation system. The current image processing requires permanently separating the two asteroids in the frame.
- Improve the features selection: some criteria can be added to increase the quality of selected features for better tracking or longer tracks. A feature management system can be implemented.
- Study the attitude determination problem and its coupling with translation estimation. The full six DoF can lead to different performances for the developed algorithms.

Bibliography

[1] E. Caroselli, F. Belien, A. Falke, R. Förstner, and F. Curti, "NEO-MAPP µLander GN&C for Safe Autonomous Landing on Small Solar System Bodies," in *45th Rocky Mountain AAS GN&C Conference 2022*, 2022.

[2] F. Capolupo and A. Rinalducci, "Descent & Landing Trajectory and Guidance Algorithms with Divert Capabilities for Moon Landing," *arXiv preprint arXiv:2305.13846*, 2023.

[3] T. Brady, E. Robertson, C. Epp, S. Paschall, and D. Zimpfer, "Hazard detection methods for lunar landing," in *IEEE Aerospace Conference Proceedings*, 2009.

[4] A. E. Johnson, A. Huertas, R. A. Werner, and J. F. Montgomery, "Analysis of on-board hazard detection and avoidance for safe lunar landing," in *IEEE Aerospace Conference Proceedings*, 2008.

[5] O. Ronneberger, P. Fischer, and T. Brox, "U-net: Convolutional networks for biomedical image segmentation," in *Lecture Notes in Computer Science (including subseries Lecture Notes in Artificial Intelligence and Lecture Notes in Bioinformatics)*, vol. 9351, 2015.

[6] Kaiming He and Xiangyu Zhang and Shaoqing Ren and Jian Sun, "Deep Residual Learning for Image Recognition," *arXiv 1512.03385*, 2015.

[7] Y. Li, T. Deng, B. Fu, Z. Lao, W. Yang, H. He, F. Donglin, W. He, and Y. Yao, "Evaluation of Decision Fusions for Classifying Karst Wetland Vegetation Using One-Class and Multi-Class CNN Models with High-Resolution UAV Images," *Remote Sensing*, vol. 14, 2022.

[8] H. Hachemi, L. Hamdad, and O. Douba, "Precipitation Nowcasting using CNN-RNN - Use case: North of Algeria," *Research Square*, 2023.

[9] P. Elffers, E. Caroselli, E. J. van Kampen, and E. Mooij, "Autonomous Navigation for Binary Asteroid Landing," in *2024 AIAA SciTech Forum*. AIAA, 2024.

[10] European Space Agency, *ECSS-E-ST-70-11C Space Engineering Space Segment Operability*. ESA Requirements and Standards Division, 2008. [Online]. Available: https://ecss.nl/standard/ecss-e-st-70-11c-space-segment-operability/

[11] A. Morbidelli, W. F. Bottke, C. Froeschlé, and P. Michel, "Origin and Evolution of Near-Earth Objects," in *Asteroids III*. Cambridge University Press, 2021.

[12] C. A. Goodrich, W. K. Hartmann, D. P. O'Brien, S. J. Weidenschilling, L. Wilson, P. Michel, and M. Jutzi, "Origin and history of ureilitic material in the solar system: The view from

asteroid 2008 TC3 and the Almahata Sitta meteorite," *Meteoritics and Planetary Science*, vol. 50, no. 4, 2015.

[13] C. M. Alexander, A. P. Boss, and R. W. Carlson, "The early evolution of the inner solar system: A meteoritic perspective," *Science*, vol. 293, no. 5527, 2001.

[14] M. Jutzi, E. Asphaug, P. Gillet, J. A. Barrat, and W. Benz, "The structure of the asteroid 4 Vesta as revealed by models of planet-scale collisions," *Nature*, vol. 494, no. 7436, 2013.

[15] C. F. Chyba, P. J. Thomas, L. Brookshaw, and C. Sagan, "Cometary delivery of organic molecules to the early earth," *Science*, vol. 249, no. 4967, 1990.

[16] A. Izidoro, S. N. Raymond, A. Pierens, A. Morbidelli, O. C. Winter, and D. Nesvorny‘, "The asteroid belt as a relic from a chaotic early solar system," *The Astrophysical Journal*, vol. 833, no. 1, 2016.

[17] N. Anthony and M. R. Emami, "Asteroid engineering: The state-of-the-art of Near-Earth Asteroids science and technology," *Progress in Aerospace Sciences*, vol. 100, 2018.

[18] A. Probst, G. González Peytaví, B. Eissfeller, and R. Förstner, "Mission concept selection for an asteroid mining mission," *Aircraft Engineering and Aerospace Technology*, vol. 88, no. 3, 2016.

[19] C. R. Chapman, "The hazard of near-Earth asteroid impacts on earth," *Earth and Planetary Science Letters*, vol. 222, no. 1, 2004.

[20] A. F. Cheng, H. F. Agrusa, B. W. Barbee, A. J. Meyer, T. L. Farnham, S. D. Raducan, D. C. Richardson, E. Dotto, A. Zinzi, V. Della Corte, T. S. Statler, S. Chesley, S. P. Naidu, M. Hirabayashi, J. Y. Li, S. Eggl, O. S. Barnouin, N. L. Chabot, S. Chocron, G. S. Collins, R. T. Daly, T. M. Davison, M. E. DeCoster, C. M. Ernst, F. Ferrari, D. M. Graninger, S. A. Jacobson, M. Jutzi, K. M. Kumamoto, R. Luther, J. R. Lyzhoft, P. Michel, N. Murdoch, R. Nakano, E. Palmer, A. S. Rivkin, D. J. Scheeres, A. M. Stickle, J. M. Sunshine, J. M. Trigo-Rodriguez, J. B. Vincent, J. D. Walker, K. Wünnemann, Y. Zhang, M. Amoroso, I. Bertini, J. R. Brucato, A. Capannolo, G. Cremonese, M. Dall'Ora, P. J. Deshapriya, I. Gai, P. H. Hasselmann, S. Ieva, G. Impresario, S. L. Ivanovski, M. Lavagna, A. Lucchetti, E. M. Epifani, D. Modenini, M. Pajola, P. Palumbo, D. Perna, S. Pirrotta, G. Poggiali, A. Rossi, P. Tortora, M. Zannoni, and G. Zanotti, "Momentum transfer from the DART mission kinetic impact on asteroid Dimorphos," *Nature*, vol. 616, no. 7957, 2023.

[21] A. F. Cheng, A. S. Rivkin, P. Michel, J. Atchison, O. Barnouin, L. Benner, N. L. Chabot, C. Ernst, E. G. Fahnestock, M. Kueppers, P. Pravec, E. Rainey, D. C. Richardson, A. M. Stickle, and C. Thomas, "AIDA DART asteroid deflection test: Planetary defense and science objectives," *Planetary and Space Science*, vol. 157, 2018.

[22] M. J. Belton, J. Veverka, P. Thomas, P. Helfenstein, D. Simonelli, C. Chapman, M. E. Davies, R. Greeley, R. Greenberg, J. Head, S. Murchie, K. Klaasen, T. V. Johnson, A. McEwen, D. Morrison, G. Neukum, F. Fanale, C. Anger, M. Carr, and C. Pilcher, "Galileo encounter with 951 Gaspra: First pictures of an asteroid," *Science*, vol. 257, no. 5077, 1992.

[23] C. M. Hartzell and D. J. Scheeres, "Dynamics of levitating dust particles near asteroids and the Moon," *Journal of Geophysical Research: Planets*, vol. 118, no. 1, 2013.

[24] K. Berry, B. Sutter, A. May, K. Williams, B. W. Barbee, M. Beckman, B. Williams, N. . Gsfc, and L. Martin, "OSIRIS-REx Touch-And-Go (TAG) Mission Design and Analysis," in *36th Annual AAS Guidance and Control Conference*, 2013.

[25] T. M. Ho, V. Baturkin, C. Grimm, J. T. Grundmann, C. Hobbie, E. Ksenik, C. Lange, K. Sasaki, M. Schlotterer, M. Talapina, N. Termtanasombat, E. Wejmo, L. Witte, M. Wrasmann, G. Wübbels, J. Rößler, C. Ziach, R. Findlay, J. Biele, C. Krause, S. Ulamec, M. Lange, O. Mierheim, R. Lichtenheldt, M. Maier, J. Reill, H. J. Sedlmayr, P. Bousquet, A. Bellion, O. Bompis, C. Cenac-Morthe, M. Deleuze, S. Fredon, E. Jurado, E. Canalias, R. Jaumann, J. P. Bibring, K. H. Glassmeier, D. Hercik, M. Grott, L. Celotti, F. Cordero, J. Hendrikse, and T. Okada, "MASCOT—The Mobile Asteroid Surface Scout Onboard the Hayabusa2 Mission," *Space Science Reviews*, vol. 208, no. 1-4, 2017.

[26] C. Rouff, "Autonomy in Future Space Missions," *AAAI*, vol. 03, 2002.

[27] M. Bajracharya, M. W. Maimone, and D. Helmick, "Autonomy for Mars Rovers: Past, present, and future," *Computer*, vol. 41, no. 12, 2008.

[28] V. Da Poian, E. Lyness, R. Danell, X. Li, B. Theiling, M. Trainer, D. Kaplan, and W. Brinckerhoff, "Science Autonomy and Space Science: Application to the ExoMars Mission," *Frontiers in Astronomy and Space Sciences*, vol. 9, 2022.

[29] M. Martin, E. Caroselli, J. Olucak, S. Busi, W. Fichter, B. Liu, A. Liesch, P. Suwinski, V. Chernykh, and K. Janschek, "Pioneering the small bodies frontiers: the key enabling technologies for autonomous precise mobility," in *European Space Agency GNC Conference 2023*, 2023.

[30] W. F. Truszkowski, M. G. Hinchey, J. L. Rash, and C. A. Rouff, "Autonomous and autonomic systems: A paradigm for future space exploration missions," *IEEE Transactions on Systems, Man and Cybernetics Part C: Applications and Reviews*, vol. 36, no. 3, 2006.

[31] M. Tipaldi and L. Glielmo, "A Survey on Model-Based Mission Planning and Execution for Autonomous Spacecraft," *IEEE Systems Journal*, vol. 12, no. 4, 2018.

[32] T. D. Swindle, I. A. Nesnas, and J. C. Castillo-Rogez, "Design Reference Missions (DRMs) for Advancing Autonomy in Exploration of Small Bodies," in *AGU Fall Meeting Abstracts*, 2019.

[33] I. De Pater and J. J. Lissauer, *Planetary sciences*. Cambridge University Press, 2015.

[34] D. J. Scheeres, *Orbital motion in strongly perturbed environments: applications to asteroid, comet and planetary satellite orbiters*, 1st ed. Springer, 2016.

[35] F. Câmara, P. Rogata, and A. Caramagno, "Hazard avoidance techniques for vision based landing," *Guidance, Navigation and Control Systems*, vol. 606, 2006. [Online]. Available: https://www.researchgate.net/publication/229013448

[36] R. Moghe and R. Zanetti, "A Deep Learning Approach to Hazard Detection for Autonomous Lunar Landing," *Journal of the Astronautical Sciences*, vol. 67, no. 4, pp. 1811–1830, 12 2020.

[37] C. L. Thornton and J. S. Border, *Radiometric Tracking Techniques for Deep Space Navigation.* John Wiley & Sons, 2003, vol. 1.

[38] P. V. Simplicio, "Guidance and control elements for improved access to space: from planetary landers to reusable launchers," Ph.D. dissertation, University of Bristol, 2019.

[39] G. Ono, F. Terui, N. Ogawa, S. Kikuchi, Y. Mimasu, K. Yoshikawa, H. Ikeda, Y. Takei, S. Yasuda, K. Matsushima, T. Masuda, T. Saiki, and Y. Tsuda, "GNC strategies and flight results of Hayabusa2 first touchdown operation," *Acta Astronautica*, vol. 174, pp. 131–147, 9 2020.

[40] P. G. Antreasian, C. D. Adam, J. Geeraert, J. M. Leonard, E. Lessac-Chenen, A. Levine, J. McAdams, L. K. McCarthy, D. Nelson, B. Page, J. Y. Pelgrift, E. Sahr, D. Wibben, B. Williams, K. Williams, K. Berry, K. Getzandanner, M. Moreau, S. Rieger, B. W. Ashman, D. E. Highsmith, and D. Lauretta, "OSIRIS-REx Proximity Operations and Navigation Performance at (101955) Bennu," in *AIAA Science and Technology Forum and Exposition, AIAA SciTech Forum 2022*, 2022.

[41] C. Sánchez-Sánchez, D. Izzo, and D. Hennes, "Optimal real-time landing using deep networks," in *Proceedings of the Sixth International Conference on Astrodynamics Tools and Techniques, ICATT*, vol. 12, 2016.

[42] D. Izzo, M. Märtens, and B. Pan, "A Survey on Artificial Intelligence Trends in Spacecraft Guidance Dynamics and Control," *Astrodynamics 3*, pp. 287–299, 12 2019. [Online]. Available: http://arxiv.org/abs/1812.02948

[43] D. J. Scheeres and D. J. Scheeres, *Close proximity operations at small bodies: orbiting, hovering, and hopping*, 1st ed. Cambridge University Press, 2004. [Online]. Available: https://www.researchgate.net/publication/253052066

[44] P. G. Antreasian, S. R. Chesley, J. K. Miller, J. J. Bordi, and B. G. Williams, "The design and navigation of the near Shoemaker landing on Eros," in *Advances in the Astronautical Sciences*, vol. 109 II, 2002, pp. 989–1015.

[45] J. Kawaguchi, "Hayabusa, summary of guidance, navigation and control achievement in its proximity phase," in *Collection of Technical Papers - AIAA/AAS Astrodynamics Specialist Conference, 2006*, vol. 2. American Institute of Aeronautics and Astronautics Inc., 2006, pp. 1334–1341.

[46] i. Bexco, T. Kubota, T. Hashimoto, i. Kawaguchi, M. Uo, and i. Shirakawa, "SICE-ICASE International Joint Conference Guidance and Navigation of Hayabusa Spacecraft for Asteroid Exploration and Sample Return Mission," in *SICE-ICASE International Joint Conference. IEEE*, 2006.

[47] T. Kominato, M. Matsuoka, M. Uo, T. Hashlmoto, T. Kubota, and J. Kawaguchi, "HAYABUSA's Optical Hybrid Navigation for Approaching to and Stationkeeping around Asteroid ITOKAWA," *The Journal of Space Technology and Science*, vol. 22, no. 1, pp. 11–1, 2006.

[48] H. Morita, K. Shirakawa, M. Uo, T. Hashimoto, T. Kubota, and J. Kawaguchi, "Hayabusa descent navigation based on accurate landmark tracking scheme," *the journal of space technology and science*, vol. 22, no. 1, pp. 21–1, 2006.

[49] A. Accomazzo, P. Ferri, S. Lodiot, J. L. Pellon-Bailon, A. Hubault, R. Porta, J. Urbanek, R. Kay, M. Eiblmaier, and T. Francisco, "Rosetta operations at the comet," *Acta Astronautica*, vol. 115, 2015.

[50] R. P. de Santayana and M. Lauer, "Optical measurements for rosetta navigation near the comet," in *Proceedings of the 25th International Symposium on Space Flight Dynamics*, 2015.

[51] L. Witte, R. Roll, J. Biele, S. Ulamec, and E. Jurado, "Rosetta lander Philae – Landing performance and touchdown safety assessment," *Acta Astronautica*, vol. 125, pp. 149–160, 8 2016.

[52] S. Ulamec, J. Biele, P. W. Bousquet, P. Gaudon, K. Geurts, T. M. Ho, C. Krause, C. Lange, R. Willnecker, and L. Witte, "Landing on small bodies: From the rosetta lander to MASCOT and beyond," *Acta Astronautica*, vol. 93, 2014.

[53] N. Mastrodemos, B. Rush, A. Vaughan, and W. Owen, "Optical Navigation For The Dawn Mission At Vesta," *Advances in the Astronautical Sciences*, vol. 140, 2011.

[54] S. Kikuchi, F. Terui, N. Ogawa, T. Saiki, G. Ono, K. Yoshikawa, Y. Takei, Y. Mimasu, H. Ikeda, H. Sawada, S. V. Wal, S. Sugita, S.-i. Watanabe, and Y. Tsuda, "Design and Reconstruction of the Hayabusa2 Precision Landing on Ryugu," *Journal of Spacecraft and Rockets*, vol. 57, no. 5, pp. 1033–1060, 9 2020.

[55] T. Mizuno, T. Kase, T. Shiina, M. Mita, N. Namiki, H. Senshu, R. Yamada, H. Noda, H. Kunimori, N. Hirata, F. Terui, and Y. Mimasu, "Development of the Laser Altimeter (LIDAR) for Hayabusa2," pp. 33–47, 7 2017.

[56] Y. Tsuda, M. Yoshikawa, M. Abe, H. Minamino, and S. Nakazawa, "System design of the hayabusa 2-asteroid sample return mission to 1999 JU3," *Acta Astronautica*, vol. 91, pp. 356–362, 2013.

[57] B. Williams, P. Antreasian, E. Carranza, C. Jackman, J. Leonard, D. Nelson, B. Page, D. Stanbridge, D. Wibben, K. Williams, M. Moreau, K. Berry, K. Getzandanner, A. Liounis, A. Mashiku, D. Highsmith, B. Sutter, and D. S. Lauretta, "OSIRIS-REx Flight Dynamics and Navigation Design," 6 2018.

[58] D. A. Lorenz, R. Olds, A. May, C. Mario, M. E. Perry, E. E. Palmer, and M. Daly, "Lessons learned from OSIRIS-REx autonomous navigation using natural feature tracking," in *IEEE Aerospace Conference Proceedings*. IEEE Computer Society, 6 2017.

[59] P. Tortora and V. Di Tana, "LICIACube, the Italian witness of DART impact on didymos," in *2019 IEEE International Workshop on Metrology for AeroSpace, MetroAeroSpace 2019 - Proceedings*, 2019.

[60] J. A. Atchison, M. Abrahamson, M. T. Ozimek, B. L. Kantsiper, E. Y. Adams, A. F. Cheng, A. S. Rivkin, C. L. Reed, S. Bhaskaran, Z. Tarzi, D. Velez, J. Bellerose, F. Laipert, and D. Grebow, "Double asteroid redirection test (DART) mission design and navigation for low energy escape," in *Proceedings of the International Astronautical Congress, IAC*, vol. 2018-October, 2018.

[61] L. T. Elkins-Tanton, E. Asphaug, J. F. Bell, H. Bercovici, B. Bills, R. Binzel, W. F. Bottke, S. Dibb, D. J. Lawrence, S. Marchi, T. J. McCoy, R. Oran, R. S. Park, P. N. Peplowski, C. A. Polanskey, T. H. Prettyman, C. T. Russell, L. Schaefer, B. P. Weiss, M. A. Wieczorek, D. A. Williams, and M. T. Zuber, "Observations, Meteorites, and Models: A Preflight Assessment of the Composition and Formation of (16) Psyche," *Journal of Geophysical Research: Planets*, vol. 125, no. 3, 2020.

[62] J. P. Shoer, J. Wood, and C. Nie, "Lockheed Martin Deep Space SmallSats for Solar System Exploration," in *Proceedings of the International Astronautical Congress, IAC*, vol. B4, 2021.

[63] J. Gil-Fernandez, M. Casasco, I. Carnelli, P. Martino, and M. Küppers, "HERA autonomous Guidance, Navigation and Control experiments: enabling better asteroid science & future missions," in *8th European Conference for Aeronautics and Space Sciences (EUCASS)*, 2019.

[64] J.-E. Wahlund, D. Andrews, and A. Pentila, "Asteroid Prospection Explorer (APEX) Cubesat For the ESA Hera Mission," *EPSC-DPS Joint Meeting, Vol. 13*, vol. 2019, no. 2132, 2019.

[65] H. R. Goldberg, O. Karatekin, B. Ritter, A. Herique, P. Tortora, C. Prioroc, B. G. Gutierrez, P. Martino, and I. Carnelli, "The juventas cubesat in support of ESA's hera mission to the asteroid didymos," in *Small Satellite Conference*, 2019.

[66] K. Kuramoto, Y. Kawakatsu, M. Fujimoto, A. Araya, M. A. Barucci, H. Genda, N. Hirata, H. Ikeda, T. Imamura, J. Helbert, S. Kameda, M. Kobayashi, H. Kusano, D. J. Lawrence, K. Matsumoto, P. Michel, H. Miyamoto, T. Morota, H. Nakagawa, T. Nakamura, K. Ogawa, H. Otake, M. Ozaki, S. Russell, S. Sasaki, H. Sawada, H. Senshu, S. Tachibana, N. Terada, S. Ulamec, T. Usui, K. Wada, S. i. Watanabe, and S. Yokota, "Martian moons exploration MMX: sample return mission to Phobos elucidating formation processes of habitable planets," 2022.

[67] P. Michel, A. Falke, and S. Ulamec, "The European Commission funded NEO-MAPP project in support of the ESA Hera mission: Near-Earth Object Modelling And Payload for Protection," in *43rd COSPAR Scientific Assembly*, 2020.

[68] P. Elffers, E. van Kampen, E. Mooij, and E. Caroselli, "Autonomous Navigation for Binary Asteroid Landing: A vision-based and altimeter-aided navigation filter for small spacecraft," Ph.D. dissertation, TU Delft, 2023.

[69] E. Caroselli, F. Belien, A. Falke, F. Curti, and R. Förstner, "Deep Learning-Based Passive Hazard Detection for Asteroid Landing in Unexplored Environment," in *45th Rocky Mountain AAS GN&C Conference 2022*, 2022.

[70] E. Caroselli, M. Martin, K. R. Atkinson, F. Curti, and R. Förstner, "Autonomous Lidar-Free Hazard Detection and Landing Site Selection for Small Bodies Descent," in *33rd AAS/AIAA Space Flight Mechanics Meeting*, 2023.

[71] E. Gramigna, J. G. Johansen, R. L. Manghi, J. Magalhaes, M. Zannoni, P. Tortora, E. L. Bras, and A. Togni, "Hera Inter-Satellite link Doppler characterization for Didymos Gravity Science experiments," in *2022 IEEE 9th International Workshop on Metrology for AeroSpace, MetroAeroSpace 2022 - Proceedings*, 2022.

[72] J. Bellerose, S. Bhaskaran, and S. Chesley, "AIDA: measuring asteroid binary system parameters and DART-imparted deflection using the AIM spacecraft," *Pasadena, CA: Jet Propulsion Laboratory, National Aeronautics and Space*, 2017.

[73] A. Pellacani, P. Kicman, F. Cabral, C. Prioroc, P. Bodin, R. Larsson, J. Gil, M. Casasco, and I. Carnelli, "HERA GNC Subsystem for deep space and asteroids proximity operations," in *Proceedings of the International Astronautical Congress, IAC*, vol. 2019-October, 2019.

[74] A. Pellacani, M. Graziano, M. Fittock, J. Gil, and I. Carnelli, "HERA vision based GNC and autonomy," *European Conference for AeroSpace Sciences*, 2019.

[75] P. Michel, M. Küppers, A. C. Bagatin, B. Carry, S. Charnoz, J. de Leon, A. Fitzsimmons, P. Gordo, S. F. Green, A. Hérique, M. Juzi, O. Karatekin, T. Kohout, M. Lazzarin, N. Murdoch, T. Okada, E. Palomba, P. Pravec, C. Snodgrass, P. Tortora, K. Tsiganis, S. Ulamec, J. B. Vincent, K. Wünnemann, Y. Zhang, S. D. Raducan, E. Dotto, N. Chabot, A. F. Cheng, A. Rivkin, O. Barnouin, C. Ernst, A. Stickle, D. C. Richardson, C. Thomas, M. Arakawa, H. Miyamoto, A. Nakamura, S. Sugita, M. Yoshikawa, P. Abell, E. Asphaug, R. L. Ballouz, W. F. Bottke, D. S. Lauretta, K. J. Walsh, P. Martino, and I. Carnelli, "The ESA Hera Mission: Detailed Characterization of the DART Impact Outcome and of the Binary Asteroid (65803) Didymos," *Planetary Science Journal*, vol. 3, no. 7, 2022.

[76] A. Accomazzo, S. Lodiot, and V. Companys, "Rosetta mission operations for landing," *Acta Astronautica*, vol. 125, pp. 30–40, 8 2016.

[77] P. Rogata, E. Di Sotto, F. Câmara, A. Caramagno, J. M. Rebordão, B. Correia, P. Duarte, and S. Mancuso, "Design and performance assessment of hazard avoidance techniques for vision-based landing," *Acta Astronautica*, vol. 61, no. 1-6, pp. 63–77, 6 2007.

[78] M. S. Haynes, I. Fenni, Y. Gim, W. Kofman, and A. Herique, "Angular and radial sampling criteria for monostatic and bistatic radar tomography of solar system small bodies," *Advances in Space Research*, vol. 68, no. 9, 2021.

[79] B. Ritter, O. Karatekin, M. Van Ruymbeke, M. Noeker, E. Ümit, R. Laguerre, S. Berkenbosch, S. Bonnewijn, V. Ransbeeck, . E. Neefs, F. Wielant, E. Tasev, and H. Goldberg, "GRASS: a Gravimeter for the Investigation of Small Solar System Bodies," in *EPSC-DPS Joint Meeting*, 2019.

[80] N. Murdoch, R. Garcia, A. Sournac, M. Bassas-Portus, A. Cadu, A. Wilhelm, M. Drilleau, A. Stott, and D. Mimoun, "a Compact Seismometer for the Geophysical Exploration of Small Bodies," in *7th IAA Planetary Defense Conference*, 2021.

[81] N. G. Dias, B. Nadal Arribas, P. Gordo, T. Sousa, J. Marinho, R. Melicio, A. Amorim, and P. Michel, "LIDAR altimeter conception for HERA spacecraft," *Aircraft Engineering and Aerospace Technology*, vol. 93, no. 6, 2021.

[82] I. Poberezhskiy, A. Johnson, D. Chang, E. Ek, D. Natzic, G. Spiers, S. Penniman, and B. Short, "Flash lidar performance testing: configuration and results," in *Laser Radar Technology and Applications XVII*, vol. 8379, 2012.

[83] N. G. Kottke, M. Vaupel, M. Tajmar, W. Konrad, N. Saks, and F. G. Hey, "Comparison of the thermionic emission properties of LaB6 and C12A7," *The 36th International Electric Propulsion Conference, University of Vienna, Austria*, 2019.

[84] AST GmbH, "Cold Gas Thruster (CGT)," 2016. [Online]. Available: https://satsearch.co/products/advanced-space-technologies-cold-gas-thruster-cgt

[85] Aerojet Rocketdyne, "In-Space Propulsion Data Sheets," 2020. [Online]. Available: https://www.satcatalog.com/component/mr-401-009n/

[86] GOMSpace Sweden, "NanoProp CGP3 Datasheet," 2021. [Online]. Available: https://gomspace.com/UserFiles/Subsystems/flyer/gomspace_nanoprop_cgp3.pdf

[87] VACCO, "Micro Propulsion System VACCO," 2021. [Online]. Available: vacco.com

[88] B. Yost, "State of the Art of Small Spacecraft Technology," *Nasa*, 2019.

[89] H. PIEN, "Autonomous Hazard Detection and avoidance for Mars exploration," in *8th Computing in Aerospace Conference*, 1991.

[90] Y. Cheng, A. Johnson, and L. Matthies, "MER-DIMES: A planetary landing application of computer vision," in *Proceedings - 2005 IEEE Computer Society Conference on Computer Vision and Pattern Recognition, CVPR 2005*, vol. I, 2005.

[91] C. D. Epp, E. A. Robertson, and T. Brady, "Autonomous landing and hazard avoidance technology (ALHAT)," in *IEEE Aerospace Conference Proceedings*, 2008.

[92] C. D. Norman, C. J. Miller, R. D. Olds, C. E. Mario, E. E. Palmer, O. S. Barnouin, M. G. Daly, J. R. Weirich, J. A. Seabrook, C. A. Bennett, B. Rizk, B. J. Bos, and D. S. Lauretta, "Autonomous Navigation Performance Using Natural Feature Tracking during the OSIRIS-REx Touch-and-Go Sample Collection Event," *Planetary Science Journal*, vol. 3, no. 5, 2022.

[93] J. Balaram, M. M. Aung, and M. P. Golombek, "The Ingenuity Helicopter on the Perseverance Rover," *Space Science Reviews*, vol. 217, no. 4, 2021.

[94] D. Fox, "Flying a helicopter on Mars: NASA's Ingenuity," *Nature*, 2021.

[95] A. E. Johnson and J. F. Montgomery, "Overview of Terrain Relative Navigation approaches for precise lunar landing," in *IEEE Aerospace Conference Proceedings*, 2008.

[96] P. Mancini, M. Cannici, and M. Matteucci, "Deep learning for asteroids autonomous terrain relative navigation," *Advances in Space Research*, vol. 71, no. 9, 2023.

[97] D. S. Bayard and P. B. Brugarolas, "An estimation algorithm for vision-based exploration of small bodies in space," in *Proceedings of the American Control Conference*, vol. 7, 2005.

[98] C. Yang and A. Ansar, "Landmark based position estimation for pinpoint landing on Mars," in *Proceedings - IEEE International Conference on Robotics and Automation*, vol. 2005, 2005.

[99] N. Trawny, A. I. Mourikis, S. I. Roumeliotis, A. E. Johnson, and J. F. Montgomery, "Vision-aided inertial navigation for pin-point landing using observations of mapped landmarks," *Journal of Field Robotics*, vol. 24, no. 5, 2007.

[100] Y. Tian and M. Yu, "A novel crater recognition based visual navigation approach for asteroid precise pin-point landing," *Aerospace Science and Technology*, vol. 70, 2017.

[101] A. E. Johnson, A. Ansar, L. H. Matthies, N. Trawny, A. I. Mourikis, and S. I. Roumeliotis, "A general approach to terrain relative navigation for planetary landing," in *Collection of Technical Papers - 2007 AIAA InfoTech at Aerospace Conference*, vol. 2, 2007.

[102] A. Miguel San Martin, D. S. Bayard, D. T. Conway, M. Mandic, and E. S. Bailey, "A minimal state augmentation algorithm for vision-based navigation without using mapped landmarks," in *10th International ESA Conference on Guidance, Navigation & Control Systems, GNC 2017, Salzburg, Austria, May 29 - 2 June 2,2017.*, 2017.

[103] C. Cocaud and T. Kubota, "Autonomous navigation near asteroids based on visual SLAM," in *Proceedings of the 23rd International Symposium on Space Flight Dynamics, Pasadena, California*, 2012.

[104] J. Song, D. Rondao, and N. Aouf, "Deep learning-based spacecraft relative navigation methods: A survey," *Acta Astronautica*, vol. 191, 2022.

[105] M. Delpech, V. Bissonnette, and L. Rastel, "Vision-based navigation for proximity operations around asteroid 99942 Apophis," in *Proceedings of 25th International Symposium on Space Flight Dynamics*, 2015, pp. 19–25.

[106] D. Nakath, J. Clemens, and C. Rachuy, "Active Asteroid-SLAM: Active Graph SLAM with Landing Site Discovery in a Deep Space Proximity Operations Scenario," *Journal of Intelligent and Robotic Systems: Theory and Applications*, vol. 99, no. 2, pp. 303–333, 8 2020.

[107] P. Zarchan and H. Musoff, *Fundamentals of Kalman Filtering: A practical approach*, 3rd ed. American Institute of Aeronautics and Astronautics, 2015.

[108] A. J. Davison, I. D. Reid, N. D. Molton, and O. Stasse, "MonoSLAM: Real-time single camera SLAM," *IEEE Transactions on Pattern Analysis and Machine Intelligence*, vol. 29, no. 6, 2007.

[109] M. Dor, K. A. Skinner, P. Tsiotras, and T. Driver, "Visual SLAM for asteroid relative navigation," in *IEEE Computer Society Conference on Computer Vision and Pattern Recognition Workshops*, 2021.

[110] P. Pravec, C. A. Thomas, A. S. Rivkin, P. Scheirich, N. Moskovitz, M. M. Knight, C. Snodgrass, J. de León, J. Licandro, M. Popescu, A. Thirouin, D. Föhring, C. O. Chandler, W. J. Oldroyd, C. A. Trujillo, E. S. Howell, S. F. Green, J. Thomas-Osip, S. S. Sheppard, T. L. Farnham, E. Mazzotta Epifani, E. Dotto, S. Ieva, M. Dall'Ora, R. Kokotanekova, B. Carry, and D. Souami, "Photometric Observations of the Binary Near-Earth Asteroid (65803) Didymos in 2015-2021 Prior to DART Impact," *Planetary Science Journal*, vol. 3, no. 7, 2022.

[111] R. Gaskell, J. Saito, M. Ishiguro, T. Kubota, T. Hashimoto, N. Hirata, S. Abe, O. Barnouin-Jha, and D. Scheeres, "Gaskell Itokawa Shape Model V1.0. HAY-A-AMICA-5-ITOKAWASHAPE-V1.0," *NASA Planetary Data System*, vol. 92, 2008.

[112] S. M. Parkes, I. Martin, M. Dunstan, and D. Matthews, "Planet Surface Simulation with PANGU," in *Space ops 2004 conference*, 2004.

[113] S.-M. Oh and E. Johnson, "Relative motion estimation for vision-based formation flight using unscented Kalman filter," in *AIAA guidance, navigation and control conference and exhibit*, 2007.

[114] P. F. Alcantarilla, A. Bartoli, and A. J. Davison, "KAZE features," in *Computer Vision–ECCV 2012: 12th European Conference on Computer Vision, Florence, Italy, October 7-13, 2012, Proceedings, Part VI 12*. Springer, 2012, pp. 214–227.

[115] B. Lucas and T. Kanade, "Iterative Technique of Image Registration and Its Application to Stereo," in *Proceedings of the International Joint Conference on Neural Networks*, 1981.

[116] B. J. Morrell, "Autonomous Feature Tracking for Autonomous Approach to a Small Body," in *ASCEND 2020*, 2020.

[117] D. G. Lowe, "Distinctive image features from scale-invariant keypoints," *International Journal of Computer Vision*, vol. 60, no. 2, 2004.

[118] J. Villa, J. McMahon, B. Hockman, and I. Nesnas, "Autonomous navigation and dense shape reconstruction using stereophotogrammetry at small celestial bodies," in *AAS Guidance Navigation and Control Conference 2022*, 2022.

[119] K. Mikolajczyk and C. Schmid, "A performance evaluation of local descriptors," *IEEE Transactions on Pattern Analysis and Machine Intelligence*, vol. 27, no. 10, 2005.

[120] C. Tomasi, "Detection and Tracking of Point Features," *School of Computer Science, Carnegie Mellon Univ.*, vol. 91, no. April, 1991.

[121] N. Ammann and F. Andert, "Visual navigation for autonomous, precise and safe landing on celestial bodies using Unscented Kalman filtering," in *IEEE Aerospace Conference Proceedings*, 2017.

[122] D. Simon, *Optimal State Estimation*. John Wiley \& Sons, 2006.

[123] J. Solà, "Consistency of the monocular EKF-SLAM algorithm for three different landmark parametrizations," in *Proceedings - IEEE International Conference on Robotics and Automation*, 2010.

[124] H. Morita, K. Shirakawa, T. Kubota, T. Hashimoto, and J. Kawaguchi, "Hayabusa's real-time landmark tracking navigation for descents and touching-downs," in *Collection of Technical Papers - AIAA/AAS Astrodynamics Specialist Conference, 2006*, vol. 2, 2006.

[125] T. Vidal-Calleja, M. Bryson, S. Sukkaden, A. Sanfeliu, and J. Andrade-Cetto, "On the observability of bearing-only SLAM," in *Proceedings - IEEE International Conference on Robotics and Automation*, 2007.

[126] ESSB-HB-E-003 Working Group, "ESA pointing error engineering handbook," *Ecss*, vol. ESSB-HB-E-, no. 1, 2011. [Online]. Available: http://peet.estec.esa.int/files/ESSB-HB-E-003-Issue1(19July2011).pdf

[127] V. Lloyd, A. Johnson, K. Hambleton, and S. Potter, "NASA Identifies Candidate Regions for Landing Next Americans on Moon," *NASA Press Releases*, vol. 22-089, 2022.

[128] P. Peñarroya, M. Pugliatti, F. Ferrari, S. Centuori, F. Topputo, M. Vetrisano, and M. Sanjurjo-Rivo, "CubeSat landing simulations on small bodies using blender," *Advances in Space Research*, vol. 72, no. 7, 2023.

[129] R. Biesbroek, "Ways to the Moon ?" *Moon*, 2000.

[130] E. R. Jawin, S. N. Valencia, R. N. Watkins, J. M. Crowell, C. R. Neal, and G. Schmidt, "Lunar Science for Landed Missions Workshop Findings Report," *Earth and Space Science*, vol. 6, no. 1, 2019.

[131] Q. Wang and J. Liu, "A Chang'e-4 mission concept and vision of future Chinese lunar exploration activities," *Acta Astronautica*, vol. 127, 2016.

[132] P. Guardabasso, S. Paternostro, P. Bedialauneta, and R. Fonteyne, "Lunar landing necessary building blocks and good practices for a sustainable development of human lunar activities," *Acta Astronautica*, vol. 202, 2023.

[133] M. Smith, D. Craig, N. Herrmann, E. Mahoney, J. Krezel, N. McIntyre, and K. Goodliff, "The Artemis Program: An Overview of NASA's Activities to Return Humans to the Moon," in *IEEE Aerospace Conference Proceedings*, 2020.

[134] D. Kaschubek, M. Killian, and L. Grill, "System analysis of a Moon base at the south pole: Considering landing sites, ECLSS and ISRU," *Acta Astronautica*, vol. 186, 2021.

[135] W. Wollenhaupt, "Apollo orbit determination and navigation," in *8th Aerospace Sciences Meeting*, 1970.

[136] J. YU, H. Zhang, M. Cheng, J. Liang, Y. Zhao, J. Li, P. Wang, L. Wang, Y. Guan, L. Yuan, and X. Huang, "Autonomous hazard avoidance control for Chang'E-3 soft landing," *SCIENTIA SINICA Technologica*, vol. 44, no. 6, 2014.

[137] A. E. Johnson, Y. Cheng, N. Trawny, J. F. Montgomery, S. Schroeder, J. Chang, D. Clouse, S. Aaron, and S. Mohan, "Implementation of a Map Relative Localization System for Planetary Landing," *Journal of Guidance, Control, and Dynamics*, vol. 46, no. 4, 2023.

[138] M. Guo, X. Huang, M. Li, J. Hu, and C. Xu, "Adaptive entry guidance for the Tianwen-1 mission," *Astrodynamics*, vol. 6, no. 1, 2022.

[139] J. Delaune, D. S. Bayard, and R. Brockers, "Range-Visual-Inertial Odometry: Scale Observability without Excitation," *IEEE Robotics and Automation Letters*, vol. 6, no. 2, 2021.

[140] K. Berry, P. Antreasian, M. C. Moreau, A. May, and B. Sutter, "OSIRIS-REx Touch-And-Go (TAG) Navigation Performance," in *38th Annual AAS Guidance and Control Conference*, 2015, pp. 15–125. [Online]. Available: https://ntrs.nasa.gov/search.jsp?R=20160000219

[141] Y. Tsuda, S. Nakazawa, K. Kushiki, M. Yoshikawa, H. Kuninaka, and S. Watanabe, "Flight status of robotic asteroid sample return mission Hayabusa2," *Acta Astronautica*, vol. 127, 2016.

[142] Z. Zhang, W. Wang, and P. Cui, "A reliable algorithm of rock detection and avoidance for safe spacecraft landing," in *ISSCAA2010 - 3rd International Symposium on Systems and Control in Aeronautics and Astronautics*, 2010.

[143] X. Jiang, S. Li, and T. Tao, "Innovative hazard detection and avoidance strategy for autonomous safe planetary landing," *Acta Astronautica*, vol. 126, 2016.

[144] B. Parreira, J. Vasconcelos, R. Oliveira, A. Caramagno, P. Motrena, J. Dinis, and J. Rebordão, "Performance Assessment of Vision Based Hazard Avoidance During Lunar and Martian Landing," *Proceedings of 7th International Planetary Probe WorNshop. Barcelona, Spai*, 2010.

[145] J. de Lafontaine, D. Neveu, and K. Lebel, "Autonomous planetary landing using a lidar sensor: the closed-loop syste," in *Guidance, Navigation and Control Systems*, 2006.

[146] D. S. Lauretta, H. L. Enos, A. T. Polit, H. L. Roper, and C. W. Wolner, "OSIRIS-REx at Bennu: Overcoming challenges to collect a sample of the early Solar System," in *Sample Return Missions: The Last Frontier of Solar System Exploration.* Elsevier, 2021, pp. 163–194.

[147] D. Neveu, G. Mercier, J. F. Hamel, V. Simard Bilodeau, S. Woicke, M. Alger, and D. Beaudette, "Passive versus active hazard detection and avoidance systems," *CEAS Space Journal*, vol. 7, no. 2, 2015.

[148] I. Laina, C. Rupprecht, V. Belagiannis, F. Tombari, and N. Navab, "Deeper depth prediction with fully convolutional residual networks," in *2016 Fourth international conference on 3D vision (3DV)*, 2016, pp. 239–248.

[149] A. Howard, "A novel information fusion methodology for intelligent terrain analysis," in *IEEE International Conference on Fuzzy Systems*, vol. 2, 2002.

[150] V. Badrinarayanan, A. Kendall, and R. Cipolla, "SegNet: A Deep Convolutional Encoder-Decoder Architecture for Image Segmentation," *IEEE Transactions on Pattern Analysis and Machine Intelligence*, vol. 39, no. 12, 2017.

[151] N. Otsu, "Threshold selection method from gray-level histograms." *IEEE Trans Syst Man Cybern*, vol. SMC-9, no. 1, 1979.

[152] G. Bradski, "The OpenCV Library," *Dr. Dobb's Journal of Software Tools*, 2000.

[153] K. Konstantinidis and R. Förstner, "Guidance, Navigation, and Control System for Landing near Plume Source on Enceladus," *Journal of Guidance, Control, and Dynamics*, pp. 1–20, 9 2020.

[154] T. Strutz, "The distance transform and its computation," *arXiv preprint arXiv:2106.03503*, 2021.

[155] P. Cunningham, M. Cord, and S. J. Delany, "Supervised learning, machine learning techniques for multimedia," *Springer-Verlag Berlin, Heidelberg*, 2008.

[156] F. Lateef and Y. Ruichek, "Survey on semantic segmentation using deep learning techniques," *Neurocomputing*, vol. 338, 2019.

[157] E. Shelhamer, J. Long, and T. Darrell, "Fully Convolutional Networks for Semantic Segmentation," *IEEE Transactions on Pattern Analysis and Machine Intelligence*, vol. 39, no. 4, 2017.

[158] M. Shafiq and Z. Gu, "Deep Residual Learning for Image Recognition: A Survey," *Applied Sciences (Switzerland)*, vol. 12, no. 18, 2022.

[159] H. Zhao, J. Shi, X. Qi, X. Wang, and J. Jia, "Pyramid scene parsing network," in *Proceedings - 30th IEEE Conference on Computer Vision and Pattern Recognition, CVPR 2017*, vol. 2017-January, 2017.

[160] A. Arbelle and T. R. Raviv, "Microscopy cell segmentation via convolutional LSTM networks," in *Proceedings - International Symposium on Biomedical Imaging*, vol. 2019-April, 2019.

[161] A. Reuilh, C. Bonneau, O. Bonnamy, and P. Ferri, "Rosetta AOCS behaviour in the first years of operations," *IFAC Proceedings Volumes*, vol. 40, no. 7, pp. 383–388, 2007.

[162] B. Pang, E. Nijkamp, and Y. N. Wu, "Deep Learning With TensorFlow: A Review," *Journal of Educational and Behavioral Statistics*, vol. 45, no. 2, 2020.

[163] A. Rahman, S. Oh, J. Lee, and K. Choi, "Design space exploration of FPGA accelerators for convolutional neural networks," in *Proceedings of the 2017 Design, Automation and Test in Europe*, 2017.

[164] AAC Clyde Space, "ST400 Star Tracker," 2021. [Online]. Available: https://www.aac-clyde.space/wp-content/uploads/2021/11/ST400.pdf

[165] R. F. Garcia, N. Murdoch, A. Cadu, F. Bernauer, V. Dehant, C. Schmelzbach, H. Igel, F. Guattari, D. Mimoun, G. Lecamp *et al.*, "Vibrations and rotations of asteroids: internal structure imaging with 6 degrees of freedom instruments," in *7th IAA Planetary Defense Conference*, 2021.

[166] Aerospace Honeywell, "Howeywell Accelerometer Datasheet INS," 2015. [Online]. Available: aerospace.honeywell.com

[167] AAC Clyde Space, "IM200 Optical Imager," 2021. [Online]. Available: https://www.aac-clyde.space/wp-content/uploads/2021/11/IM200.pdf

[168] Jenoptik, "Diode Laser Range Finder," 2021. [Online]. Available: https://www.jenoptik.com/products/lidar-sensors-technologies/laser-rangefinders/oem-modules-system-integration/dlem

[169] L. Shuang and C. Pingyuan, "Landmark tracking based autonomous navigation schemes for landing spacecraft on asteroids," *Acta Astronautica*, vol. 62, no. 6-7, pp. 391–403, 3 2008.

[170] M. C. Nolan, C. Magri, E. S. Howell, L. A. Benner, J. D. Giorgini, C. W. Hergenrother, R. S. Hudson, D. S. Lauretta, J. L. Margot, S. J. Ostro, and D. J. Scheeres, "Shape model and surface properties of the OSIRIS-REx target Asteroid (101955) Bennu from radar and lightcurve observations," *Icarus*, vol. 226, no. 1, 2013.

[171] P. Simplício, A. Marcos, E. Joffre, M. Zamaro, and N. Silva, "Review of guidance techniques for landing on small bodies," *Progress in Aerospace Sciences*, vol. 103, pp. 69–83, 11 2018.

Appendices

Appendix A

Reference Frames

In this section, the reference frames used in the study are described, and their related mutual inter-relationships are defined and shown in Table A.1; they are chosen to derive in mathematical terms the landing scenario equations easily, their relations are sketched in Figure A.2.

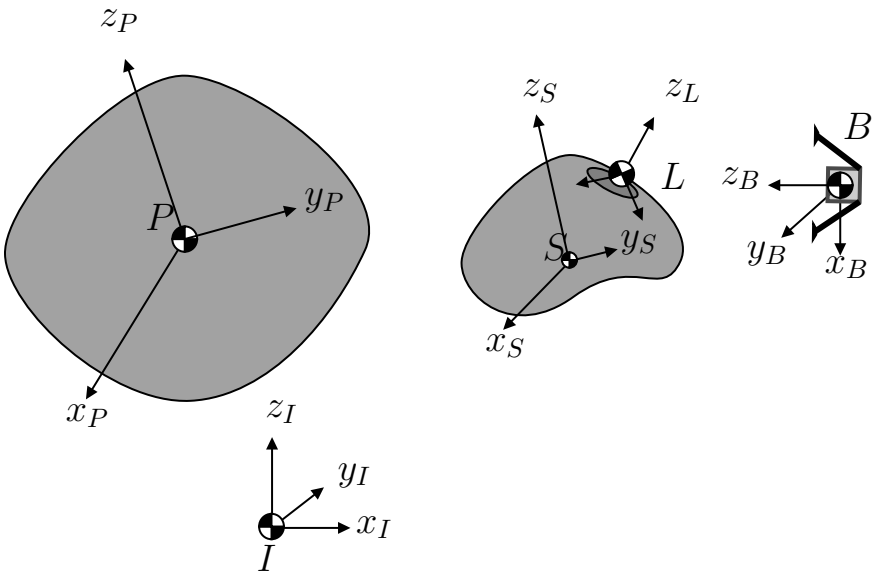

Figure A.1: Reference frames sketch as defined in the document

Name	Origin	Axis	Scope
J2000 (J)	Solar System's barycentre	X: vernal equinox at 1 January 2000 12:00:00 Terrestrial Time Z: normal to the equator at reference time Y: right-hand rule completion According to J2000	Used for ephemerides of the binary system and the Sun's position. Reference for all other coordinate systems.

Binary system Quasi-inertial (I)	Binary system CoM	Aligned with J	It describes the solution for the primary and secondary motion and the landing trajectory in the HAP. More readable distances compared to J coordinate frame. Note: I is quasi-inertial because it is orbiting around the Sun. However, the simulation time allows to neglect the non-inertial effects, justifying the assumption.
Primary Body Centred Primary Body Fixed (P)	Primary CoM	X: Axis with minimum MOI Z: rotation axis, assuming the maximum MOI Y: right-hand rule completion	It is fixed to the primary and rotates with it. It is used to describe the rotation of the primary
Secondary Body Centred Secondary Body Fixed (S)	Secondary CoM	X: axis with minimum MOI Z: rotation axis, assuming the maximum MOI Y: right-hand rule completion	Used for proximity operation and terminal landing phases. To describe location on the target. Note: At time 0 is aligned with CoM of the primary along the minimum inertia axis

Landing Site Reference Frame (L)	Landing site location (centroid)	Z: anti-parallel to the effective gravity vector X: pointing rotation axis, assuming the maximum MOI Y: right-hand rule completion	Used for features processing and relative navigation during LAP and surface operations Note: The effective gravity vector is defined by gravity and centrifugal acceleration. The Coriolis acceleration is assumed to be zero because L does not move with respect to the S coordinate system. Additionally, the Euler acceleration is supposed to be zero because the target body's angular acceleration is considered negligible. Thus, the effective gravity vector is defined by the following. $g_{S,eff} = g_S - \tilde{\omega}_S^{SI}(\omega_S^{SI} r_S^{SL})$ The symbols $g, \omega_S^S I, r_S^{SL}$ denote the gravity vector, angular rate of the target body w.r.t. the inertial frame, and the origin of the local-level-frame w.r.t. the target body frame respectively. This frame is fixed for a landing maneuver. The estimated/modeled effective gravity vector at the start of the landing is used.
Mechanical Frame	Connection point between landing legs joint and bottom panel of NEO-MAPP core	Z: downward directed, perpendicular to the horizontal bottom panel X: perpendicular to the z-axis in the direction of one landing leg Y: right-hand rule completion	Physically measurable coordinate system

Lander Body Fixed (B)	Lander CoM	Z: downward directed, perpendicular to the horizontal bottom panel X: perpendicular to the z-axis in the direction of one landing leg Y: right-hand rule completion	Used for attitude determination and control.
Lander Body reference frame (R)	Lander CoM	Z: pointing the CoM of the secondary. X: points towards the rotation axis of the secondary Y: right-hand rule completion	It is the reference frame that relates the attitude to inertial. It is useful to define the reference pointing.

Table A.1: Reference Frames Definition

A.1 From J- to I-frame

The reference frames from Figure A.1 define the coordinate systems in this section. The transformation between J- and I-frame is only a translation. The transformation of a vector from A to B from the J- to I-system is given by:

$$\mathbf{r}_I^{AB} = \mathbf{r}_J^{AB} - \mathbf{r}_J^{JI} \tag{A.1}$$

The position vector of the CoM of the system w.r.t. the Solar System's barycentre r_J^{JI} is given by the corresponding ephemeris information.

A.2 From I- to P-frame

The transformation between the I- and P-system is both a rotation and a translation. The translation between the P- and I-system is defined by r_P^{PI} the surface position of the system CoM w.r.t. the CoM of the primary body CoM. The z-axis of the P-system is defined by the pole direction, which is specified by the right ascension λ and declination ϕ. In addition to the initial attitude, the body rotates around its spin axis (z-axis of the P-frame) with the rotational speed ω.

$$R_{PI} = R_3\left(\omega t\right) R_1\left(\frac{\pi}{2} - \phi\right) R_3\left(\frac{\pi}{2} + \lambda\right) \tag{A.2}$$

Here t is the simulation time. The transformation of a position vector can be described with:

$$\mathbf{r}_P^{AB} = \mathbf{r}_P^{PI} + R_{PI}\mathbf{r}_I^{AB} \tag{A.3}$$

This assumes that the z-axis of the P-frame is the spin axis of the body, e.g., no nutation or precision exists.

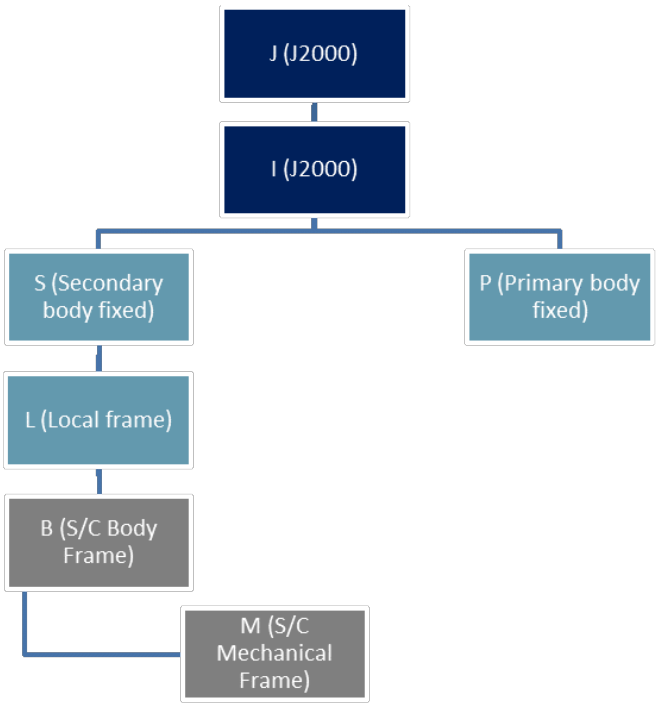

Figure A.2: Reference frames diagram

A.3 Body-fixed Frame Definition

The body-fixed coordinate system of the primary body rescaled Bennu is visualized in Figure A.3. The red, green, and blue axes indicate the body-fixed frame's x-, y- and z-axis.

The body-fixed coordinate system of the secondary body rescaled Itokawa is visualized in Figure A.4. The red, green, and blue axes indicate the x-, y- and z-axis of the body-fixed frame, respectively.

A.4 From I- to S-frame

The transformation between the I- and S-system is both a rotation and a translation. The translation between the S- and I-system is defined by r_S^{SI} the surface position of the system CoM w.r.t. the CoM of the secondary body CoM. The z-axis of the S-system is defined by the pole direction, which is specified by the right ascension λ and declination ϕ. In addition to the initial attitude, the body rotates around its spin axis (z-axis of the S-frame) with the rotational speed ω.

$$R_{SI} = R_3(\omega t)\, R_1\left(\frac{\pi}{2} - \phi\right) R_3\left(\frac{\pi}{2} + \lambda\right) \tag{A.4}$$

Here t is the simulation time. The transformation of a position vector can be described with:

$$\mathbf{r}_S^{AB} = \mathbf{r}_S^{SI} + R_{SI}\mathbf{r}_I^{AB} \tag{A.5}$$

This assumes that the z-axis of the P-frame is the spin axis of the body, e.g., no nutation or precision exists.

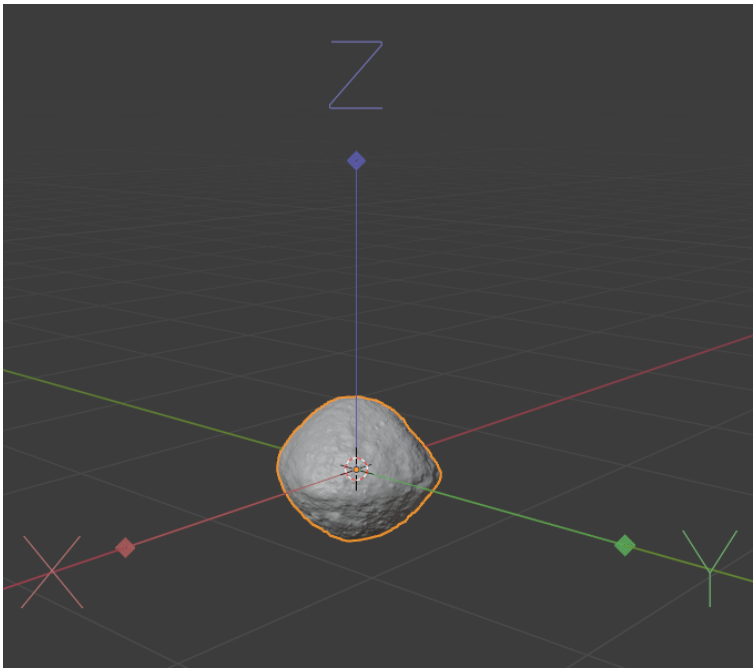

Figure A.3: Bennu Rescaled body shape with its body-fixed coordinate system (x-, y- and z-axes in red, green, and blue).

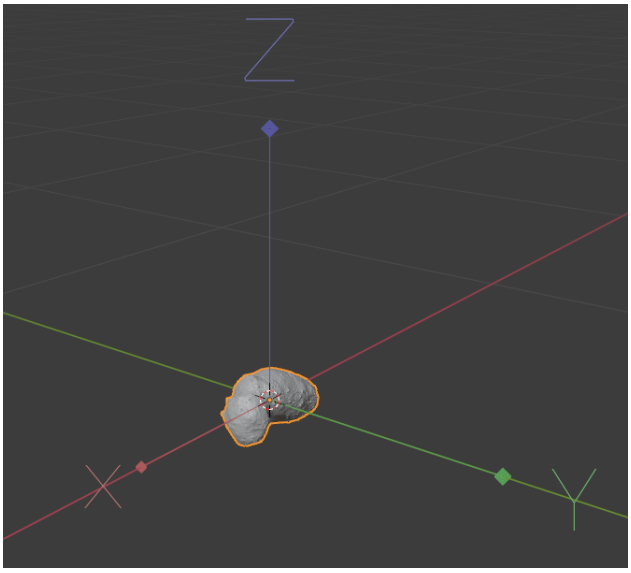

Figure A.4: Itokawa Rescaled body shape with its body-fixed coordinate system (x-, y- and z-axes in red, green, and blue).

A.5 From S- to L-frame

The transformation between the S- and L-system is a translation and rotation. The S- and L-system translation is defined by r_S^{SL}, the surface position of the desired local plane w.r.t. the CoM of the secondary body. This is the selected landing position of NEO-MAPP after the retargeting maneuver. The rotation between the S- and L-system is defined by the effective gravity vector g_{eff} at the chosen position r_S^{SL}. The position from the CoM of the secondary body and the surface position of the desired local plane is given by the vector r_S^{SL}. The unit vector of the effective gravity vector defines the normal vector of the $x_L - y_L$ plane. The axis x_L is defined as the projection of the vector $\mathbf{r}_S^{LS_z}$ onto the plane spanned by z_L. This ensures that x_L and z_L are perpendicular to each other. The superscript S_z denotes the location of the end of the z_S axis. Note that z_S is simply the unit vector in the z-direction in the S-frame. The axis y_L is defined by the cross product between the z_L- and x_L-axis. Mathematically, this transformation is defined in the following way.

$$\mathbf{z}_L = \frac{\mathbf{g}_{S,eff}}{|\mathbf{g}_{S,eff}|} \tag{A.6}$$

$$\mathbf{x}_L = \frac{\mathbf{r}_S^{LS_z} - \left(\mathbf{r}_S^{LS_z} \cdot \mathbf{z}_l\right) \mathbf{z}_L}{|\mathbf{r}_S^{LS_z} - \left(\mathbf{r}_S^{LS_z} \cdot \mathbf{z}_l\right) \mathbf{z}_L|} \tag{A.7}$$

$$\mathbf{y}_L = \frac{\mathbf{z}_L \times \mathbf{x}_L}{|\mathbf{z}_L \times \mathbf{x}_L|} \tag{A.8}$$

where $r_S^{LS_Z} = z_L - r_S^{SL}$

The direct cosine matrix can be derived from the base vectors.

$$R_{SL} = \begin{pmatrix} \mathbf{x}_L & \mathbf{y}_L & \mathbf{z}_L \end{pmatrix} \tag{A.9}$$

The transformation of a position vector can be described with:

$$r_L^{AB} = R_{LS} \left(\mathbf{r}_S^{AB} - \mathbf{r}_S^{SL}\right) \tag{A.10}$$

Appendix B

Avionics and Design Trade-off

This appendix presents technical information and analyses related to the avionics system and design considerations. The section comprises three key subsections, starting with an Avionics Datasheet detailing system specifications and capabilities.

B.1 Avionics Datasheet

B.1.1 Star Tracker Model

The STR model is based on an ST400 unit by AAC Clyde Space [164].

Parameter	Unit	Value
dt_{str}	s	0.02
Accuracy (cross axis)	arcsec	10
Accuracy (boresight)	arcsec	120
Max tracking rate	°/sec	>1
Radiation	krad	9 (Si)
Size	mm	53.8x53.8x90.55
Mass	g	280

Table B.1: STR properties

B.1.2 Gyroscope

The baseline model is based on the high-performance optical fiber IMU instrument, specifically designed for small body missions at ISAE SUPAERO as part of the PIONEERS H2020 project [165].

Parameter	Unit	Value
dt_{rmu}	s	0.01
N – Angle random walk	rad/$\sqrt{s}$	1e-4
K – rate random walk	rad/$\sqrt{s^3}$	1e-4
B – Bias instability	rad/s	5e-4/3600

eps – Accuracy of flicker instability	[-]	1e-4
Number of required flicker rate system states	[-]	20
Range	rad/s	+/- 50
Noise	$\mu rad/s/\sqrt{Hz}$	< 5
BW max	Hz	DC-800
Digital resolution	nrad/s/LSB	50

Table B.2: Gyroscope Properties

B.1.3 Accelerometer

The accelerometer performance is described with the same model as the IMU, see Section B.1.2, but with linear accelerations instead of rotational rates. Based on the assessment of the IMU units, the Pioneer IMU [165] emerges as the optimal choice for the mission. It has lower noise compared to the Honeywell alternative in the 1-200 Hz frequency range, while both IMUs exhibit similar performance overall. Additionally, the lower dynamic range of the Pioneer IMU [166] is not an issue for this mission, as the asteroid environment does not entail high acceleration. Therefore, the Pioneer IMU satisfies the requirements for the mission and is the preferred option.

Parameter	Unit	Value
dt_{rmu}	s	0.01
N – Velocity random walk	$rad/\sqrt{s}$	3e-5
K – linear acceleration random walk	$rad/\sqrt{s^3}$	1e-5
B – Bias instability	rad/s	1e-5
eps – Accuracy of flicker instability	[-]	1e-5
Range	g	+/-30
Noise	$\mu m/s^2/\sqrt{Hz}$	< 100
BW max	Hz	DC-800
Digital resolution	$\mu m/s^2$/LSB	1
Power	W	<15
Mass	kg	< 1.5
Size	mm	97x97x150
Temperature	$°C$	-40/+85
Radiations	krad(Si)	10

Table B.3: Accelerometer Properties

B.1.4 Camera

The baseline camera model is based on a pinhole model; however, for more detailed specifications, IM200 by AAC Clyde Space is used as a reference [167]. The camera is simulated in ESA PANGU software (as explained in Section 3.3).

Parameter	Unit	Value
Volume	mm^3	29x29x70
Mass	g	59
Resolution	Pixel	512x512
Field of View	°	30
Frame Rate	Hz	5
F-number	-	1.2

Table B.4: Camera Properties

B.1.5 Laser Range Finder

The baseline Laser Range Finder sensor is based on DLEM 20 by Jenoptik [168]. Based on the analysis, the DLEM 20 laser range finder sensor appears to be the optimal choice for the mission. It offers a range that covers most mission operations and has a high level of accuracy with 1σ of 0.5 meters.

Additionally, the DLEM 20 is the lightest sensor in its class, which is particularly important given the stringent mass requirements of the mission. The DLEM 20's high frame rate of 25 Hz is a significant advantage that will provide critical data for the mission's success. The LRF is included in the ESA PANGU scene generator.

Parameter	Unit	Value
Volume	mm^3	50x22x34
Mass	g	33
Sample frequency	Hz	1-25
Range	m	10-5000
Accuracy	m	$<$ 0.5 m
Resolution	m	0.1

Table B.5: Laser Range Finder Properties

B.1.6 RCS

The baseline of the propulsion system is a generic cold gas thruster system (RCS). The detailed characteristics are based on JPL MarCO - Micro CubeSat Propulsion System by VACCO [87]. Key factors are summarized in Table B.6.

Parameter	Unit	Value
Thrust range	mN	10-50

Isp	s	60
Mass	kg	0.3
Minimum impulse Bit	mN-s	0.5
Thruster valve response time	ms	<20

Table B.6: Performance characteristics of the RCS.

Appendix C

GNC Model-in-the-Loop Simulator

C.1 Simulator Assumptions

Rotational State Assumptions

It is assumed that the z-axis of the P-frame and S-frame coincides with the direction of highest MOI. Nominally, this coincides with the spin axis. To describe the initial attitude of the target body frame P w.r.t., the inertial frame J, the right ascension, and declination from [110] are used. These angles describe the direction vector in the Earth Centred Inertial (ECI) frame. In this case, the J2000 Ecliptic frame is used as the ECI-frame. The unit direction vector is given by:

$$\mathbf{r}_J = \begin{bmatrix} \cos\phi\cos\lambda \\ \cos\phi\sin\lambda \\ \sin\phi \end{bmatrix} \tag{C.1}$$

where λ and ϕ are the right ascension and declination, respectively.

Note that these angles only define the pole (z-axis) of the target body. The x- and y-axis are not fixed. For simplicity, the East, North, and Up frame is used. The “Up” direction is the pole vector r_J, and the “East” and “North" direction define the x- and y-axis, respectively, as shown in Figure C.1. The rotation from the inertial frame J to the body fixed frame P is given:

$$R_{P_0 EclipJ} = R_1\left(\frac{\pi}{2} - \phi\right) R_3\left(\frac{\pi}{2} + \lambda\right) \tag{C.2}$$

$$R_{P_0 J} = R_{P_0 EclipJ} R_{EclipJ-J} \tag{C.3}$$

Alternatively, it is also possible to implement the dynamics of the target body with rigid-body dynamics. Hence, it is possible to include a deviation between the spin axis and the direction of highest MOI. As a result, tumbling can be represented. It is assumed nutation is not relevant due to the short flight duration. The same equations are valid for the secondary by substituting P with S and considering that the retrograde solution is selected in [110].

The initial condition is set in such a way that the x-axis (minimum MOI) is aligned with the centre of mass of the system:

$$R_{P_0 EclipJ} = R_3\left(\frac{\pi}{2}\right) R_1\left(\frac{\pi}{2} - \phi\right) R_3\left(\frac{\pi}{2} + \lambda\right) \tag{C.4}$$

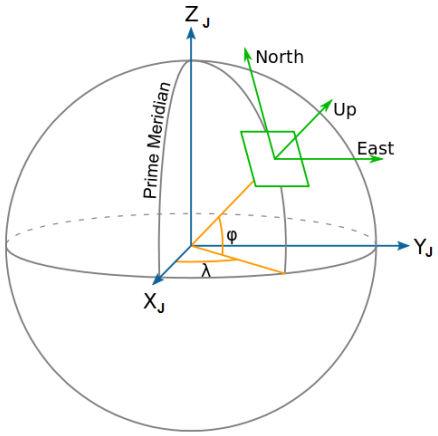

Figure C.1: Visualization of the Up, East, Down coordinate system.

$$R_{S_0 J} = R_{P_0 EclipJ}{}^{"}{}_{EclipJ-J} \tag{C.5}$$

$R_3\left(\frac{\pi}{2}\right)$ term is to align the x-axis and CoM of the primary, as shown in the previous equation according to [110]. The rotation matrix from J2000 (J-frame) to Ecliptic J2000 is provided at the initial condition from the spice kernel, and it is assumed fixed for the mission duration.

$$R_{EclipJ-J} = \begin{bmatrix} 1 & 0 & 0 \\ 0 & 0.91748206 & 0.39777716 \\ 0 & -0.39777716 & 0.91748206 \end{bmatrix} \tag{C.6}$$

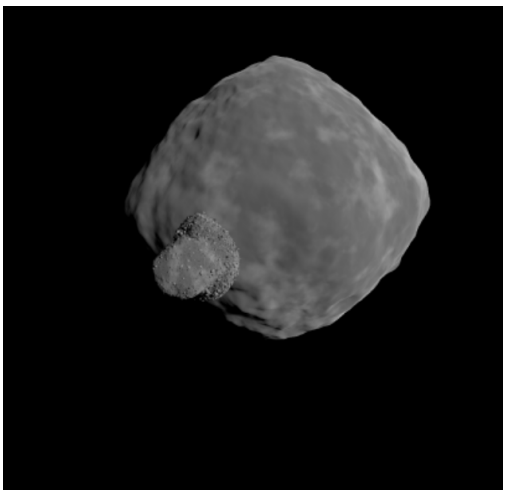

Figure C.2: Hera's Didymos system (secondary on the x-axis of I-frame)

C.1.1 Reference Orbit

As mentioned in Section 3.3.1, the orbit of Didymos system is chosen as the target system orbit. The Hera SPICE Kernel gives the orbit: STUDY – Hera – Study Earth-Mars-Didymos launch 2024 kernel set. The motion of the CoMs of the two bodies can be described using the available SPICE ESA kernels in particular: `didymos_gmv_270101_330623_v01.bsp` The previous kernel provides the motion of primary and secondary w.r.t. the system barycentre (I-frame): r_I^P, r_I^S. The

motion of the system barycentre w.r.t. to the Solar System barycentre (J-frame) r_J^{COM} is given by: `didymos_hor_200101_400101_v01.bsp`

The main assumption that can be made throughout the whole analysis is to neglect the change of position w.r.t the Sun for the main bodies. In the case of Didymos' system, given the mean motion n and an approximate landing operation time t=5 h, the angular position change can be evaluated as:

$$\alpha = nt = 0.09^\circ \tag{C.7}$$

C.1.2 Gravity Model and Disturbances

Comparison of Gravity Models

Numerous external influences come into play when a spacecraft operates in a binary asteroid setting. In addition to the gravitational pull of both the primary and secondary bodies, there are additional celestial bodies, such as the Sun, Earth, and Moon, that exert their gravitational forces on the spacecraft. Furthermore, the photons emitted by the Sun interact with the spacecraft's surface, generating a disruptive force known as solar radiation pressure. This section offers a basic examination of these forces to determine which elements will be integrated into the final simulator. A specific threshold for the magnitude of disturbance acceleration is defined, below which all impacts will be disregarded. The threshold has been established at a value of 10^{-8} m/s^2. If this acceleration is considered affecting the spacecraft following a 4 hours duration of flight from a stationary position, the resultant accumulated displacement would be approximately 1 m.

In this analysis, several assumptions are established:

- Point mass gravity model
- Circular orbit.
- Sun and Earth are the only external bodies analyzed.
- External bodies are aligned in order to maximize their influence on the asteroid system. See Figure C.3.
- Lander attitude is kept constant.

The primary and secondary bodies contribute the predominant accelerations during the landing phase. The gravitational pull of the primary body exerts its influence until approximately 150 m above the secondary body's surface. To determine the gravitational acceleration, denoted as a_B, experienced by the spacecraft at a distance r from the center of mass of the secondary body:

$$a_B(r) = GM(1/(r^2)) \tag{C.8}$$

Third Body Perturbations

Third body perturbations act on both NEO-MAPP and the target system. Since the dynamics of NEO-MAPP are described in the target body frame, the third body perturbations are limited to the difference between the gravitational attraction on NEO-MAPP and the target body. This difference is most likely very small. Care must be taken for close-by planets, especially large ones. To calculate

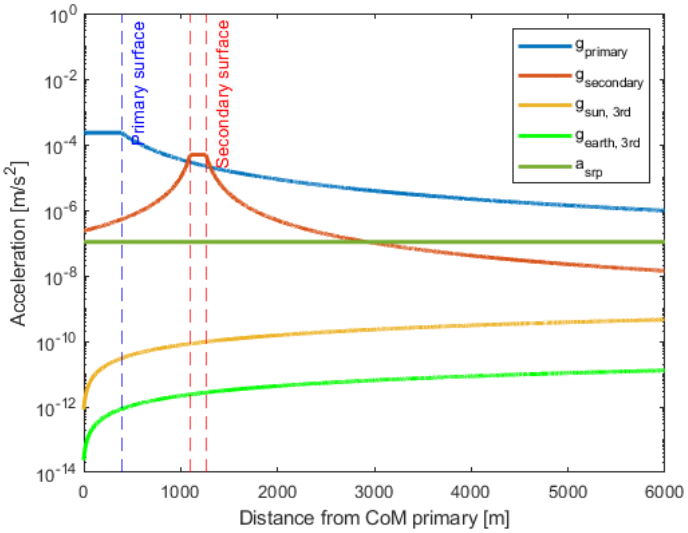

Figure C.3: Disturbance accelerations on the spacecraft as a function of the distance to the CoM of the secondary asteroid.

the influence, one can compute the third body acceleration caused by the Sun at perihelion distance (1.02 AU), with a difference in distance of 2 km. The gravitational attraction can be calculated by:

$$g = -\frac{GM}{r^2} \tag{C.9}$$

$$\nabla g = -GM\left(\frac{1}{(1.02AU)^2} - \frac{1}{(1.02AU + 2e6)^2}\right) \tag{C.10}$$

The resulting acceleration is 1.50e-7 m/s. The other third bodies are either far away or have a smaller mass.

Other solar system bodies pull on the binary asteroid system and the spacecraft. The effect of this so-called third-body perturbation a_p is calculated as follows. It is assumed that the perturbing body, the spacecraft, and the binary system are on a single line.

C.1.3 Solar Radiation Pressure

The calculation of solar radiation pressure on the lander depends on its location and alignment in relation to the Sun, as well as the optical characteristics of the surface material of the probe. To compute the solar radiation pressure, one can utilize the following formula:

$$F = C_R \frac{WS^*}{c} \tag{C.11}$$

In this formula, C_R denotes the reflectivity of the satellite, while W represents the power density of solar radiation, c symbolizes the speed of light, and S^* signifies the effective cross-sectional area.

To analyze the effect of solar radiation pressure, a geometric representation of the spacecraft is employed. The spacecraft consists of basic surfaces. When a surface is oriented toward the Sun, Equation C.11 is employed to compute the resultant force due to solar radiation pressure. The resulting torque is determined by the distance between the center of mass and the geometric center of the surface.

C.2 GNC Simulator

C.2.1 Low Altitude Phase Simulator

High-Level Overview of the Simulator

In the pursuit of developing and validating the navigation solution, a simulated environment will be employed. This simulator shall furnish the navigation filter with input data and facilitate the subsequent assessment of the navigation filter's estimated state against the ground truth. Figure C.4 presents an illustrative sketch of the simulator's constituent elements, each of which will be subject to detailed examination in the following sections.

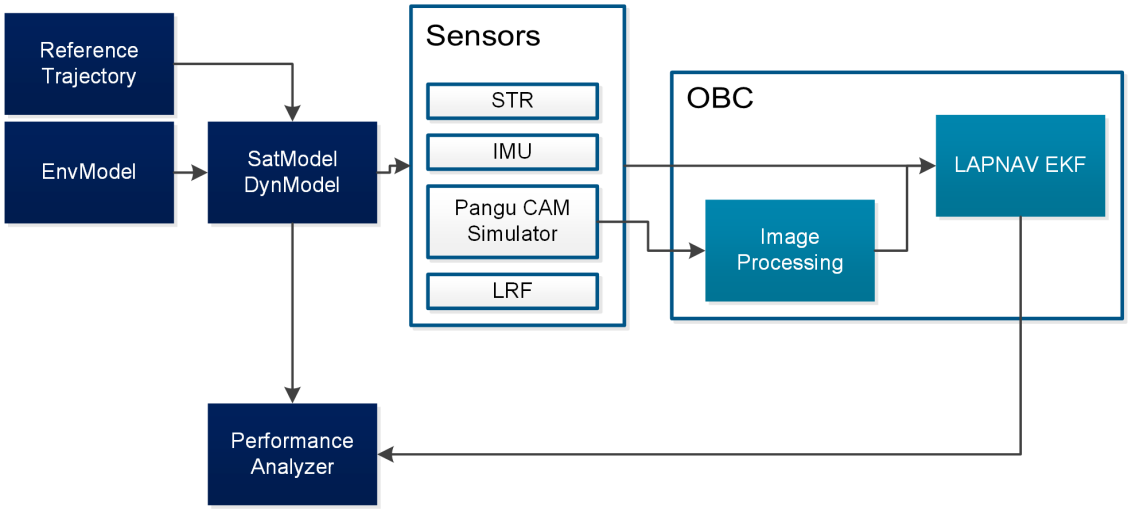

Figure C.4: Schematic diagram of the different components of the LAPNAV simulator

Environment Model

Within the simulator, there exists an environment model for LAP. This environment encompasses the gravitational fields of two asteroids, the influence of gravitational forces from other celestial bodies within the solar system, and the effects of solar radiation pressure (SRP). Precise computations are made regarding the positions and velocities of the two asteroid bodies and perturbing planets in the J2000 reference frame, which is anchored to the solar system's barycenter. Additionally, angular positions and rates are factored into the calculations. Transformation matrices and attitude quaternions in various relevant reference frames are also computed. All these computations are based on NASA's JPL *SPICE* kernels, which contain the most current data on the ephemeris of solar system bodies.

Trajectory Generator Model

The satellite requires a predetermined trajectory to adhere to. The spacecraft possesses full control authority, enabling movement in any direction, even counteracting the forces exerted by the environment. Consequently, a logical approach for guidance involves imposing a specific acceleration profile from an initial condition, effectively isolating the control aspect of the problem. This approach simplifies dynamics modeling by eliminating interactions between thrusters and the control system.

Sensors Model

The *Sensor* block encompasses models representing the noise and bias characteristics of the onboard sensors deployed on the spacecraft. Of particular importance is the Pangu camera simulator, as it generates the images utilized by image processing algorithms. These algorithms are responsible for extracting crucial data, such as extract and track features of the asteroid surface within the frame. These measurements subsequently feed into the navigation filter. Ultimately, the camera simulator must produce images, and image processing must extract data, as this mirrors the high fidelity system's operation.

Navigation Model

The navigation filters are presented in Appendix D for HAPNAV and Chapter 3 for LAPNAV.

C.2.2 Image Processing Front-End

The *Image Processing* block is part of the OBC functionalities and it is developed to extract, track and manage the features from the camera observable. In addition, it serves to initialized the filter state (i.e. landmark position) with the initial camera measurement.

C.3 Simulator Verification and Validation

All experiments within this study are conducted within a simulated setting. It is important to grasp the constraints and assumptions underlying the creation of this simulated environment in order to properly contextualize the outcomes. This section initially provides an overview of the procedures employed to confirm the accurate execution of the simulator's components.

C.3.1 *SPICE* Kernel

The *SPICE* kernel is incorporated into the simulator as a functional block responsible for providing asteroid and sun position, velocity, and orientation information at a specified moment in time, formatted in the Modified Julian Date style. By selecting a sufficiently extensive simulation duration, it becomes possible to derive the rotation period of both the primary and secondary bodies, as well as the orbit radius of the secondary, and these values are systematically validated.

The alignment of the primary's spin pole with that of the secondary's orbital spin pole is confirmed through the calculation of a vector perpendicular to the orbital plane of the secondary in relation to the primary. This verification process involves three specific points along the secondary's orbital path, each situated at one-third intervals of an orbital period from the previous point. The determination is made that the primary's rotational axis is indeed parallel to the vector normal to the orbital plane of the secondary around the primary, thereby establishing the correctness of the primary's rotational behavior. Additionally, it is ascertained that the secondary asteroid successfully completes a full revolution around the primary within the specified period, and its spin pole is also verified to align parallel with that of the primary body.

C.3.2 Solar radiation pressure

A verification process involves performing a manual examination to ascertain the orientation of the solar radiation pressure force relative to its source, the sun. Initially, the computation of the unit vector originating from the spacecraft to the sun is carried out. Subsequently, the solar radiation force is normalized. The determination of the dot product between these two vectors results in a value of -1, conclusively demonstrating that the solar radiation pressure operates in a direction counter to the incoming sunlight.

C.3.3 Gravity fields

During the configuration of the scripts responsible for computing the lookup tables for the polyhedron gravity model, intermediate outcomes have been consistently graphed to confirm their conformity to expected solutions. One vital validation procedure involves ensuring that, at significant distances, the polyhedron gravity model approximates the point mass gravity model.

Indeed, the polyhedron gravity model effectively approximates the point mass gravity model when the distance exceeds a few hundred meters from the asteroid's surface. The polyhedron gravity model is computed across a mesh grid containing points that encompass the area within the simulation's reach by the spacecraft. Linear interpolation is applied to determine gravitational values at all points lying between the grid nodes. It's important to note that the polyhedron gravity model is not inherently defined within the 3D polyhedron model itself. To address this, a function has been integrated into the script responsible for computing the gravity model lookup tables. This function verifies, for each grid point, whether it resides inside the 3D polyhedron model.

To validate the accuracy of the polyhedron gravity model's orientation, the 3D model employed for constructing the polyhedron model is imported into MATLAB using the patched polygon drawing function. Subsequently, all points identified as being within the hull of the 3D polyhedron model during the gravity lookup table computation are depicted as a point cloud graph. This graph is then compared to the original 3D model. The point cloud graph is found to be an exact match to the 3D model, confirming that the orientation of the 3D model used in the polyhedron gravity model is identical to that employed in the 3D model itself. The same data is also employed in the PANGU system, thus ensuring alignment between the primary and secondary asteroid gravity models and the visual representation in the PANGU system.

C.3.4 Camera Simulator

In order to assess the configuration of the virtual environment within the context of PANGU, a specific evaluation procedure has been devised. This evaluation involves the casting of a shadow by the secondary asteroid onto the primary asteroid. The primary objective of this evaluation is to confirm the accuracy of the 3D models implemented in PANGU, as well as to validate the fidelity of the shadows generated by the system. The resulting outcome is illustrated in Figure C.5. These outcomes align with the anticipated results, thus substantiating this particular aspect of PANGU. Many other facets pertaining to a camera simulator like PANGU remain unaddressed in this context.

Factors that are exclusive to the camera, such as the lens model and the incorporation of effects like chromatic aberration, vignetting, and radiation noise, are notable examples of aspects not examined in this assessment. Additionally, the camera's light metering settings have not been

taken into account. These intricate details necessitate thorough examination in forthcoming research endeavors to ensure that the PANGU environment accurately mirrors the actual conditions of the asteroid environment. For the purposes of this research, the extent of validation achieved is deemed sufficient for the development of the navigation system and the demonstration of the operational principles of the navigation concept.

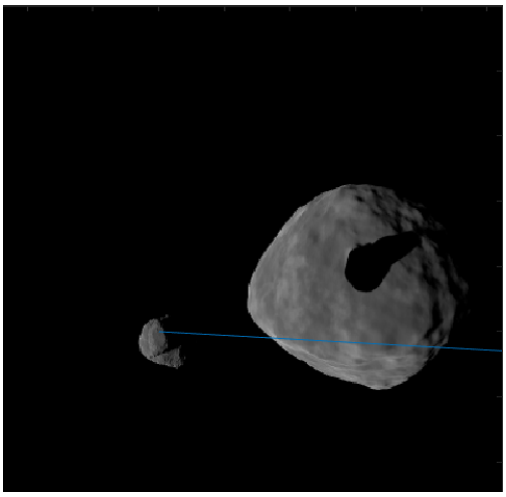

Figure C.5: Image taken during the PANGU test, showing the shadow cast by the secondary onto the primary.

Appendix D

Centroid-based Altimeter-aided Navigation for Far Range

In the context of this PhD research and as part of the preparation for a MSc thesis conducted in collaboration with TU Delft University [68], this appendix introduces a novel centroid-based altimeter-aided navigation filter designed for far range applications. This research effort has also led to the production of [9]. Within this collaboration, the presented appendix summarizes the challenges associated with long-distance navigation by proposing an innovative method that integrates centroid-based techniques and altimeter measurements. The content is organized into four main sections.

The first section covers absolute state estimation, breaking down translation dynamics, gravitational acceleration, external accelerations, and attitude dynamics.

The second section delves into sensors and measurement models, offering insights into accelerometers, cameras, image rendering, and laser range finders.

The third section focuses on image processing, discussing centroid extraction, reference landing trajectory considerations, and presenting results.

The structure of this appendix serves as a concise repository, offering a straightforward presentation of the main findings from the centroid-based altimeter-aided navigation filter designed for far-range applications. Finally, the conclusion summarizes the key outcomes, contributing to a clear understanding of the research findings.

D.1 Introduction

In this appendix, a new approach to navigation in a binary asteroid system is explored, as presented in [9]. It utilizes measurements from both asteroids captured in the camera's frame, along with a single measurement from the LRF, which employs ellipsoid models for the asteroids. The navigation camera's measurements, adjusted for changing lighting conditions, will offer LOS data. This navigation method is intended for use at medium to far distances, as determining LOS at very close range, when an asteroid occupies the entire camera's field of view, is not feasible. The key contribution of this section lies in the development of a navigation filter that is based on the binary nature of the asteroid system, coupled with the LRF. This filter shows potential resilience against errors during state initialization, thanks to the comprehensive observability when both asteroids

are visible. Unlike landmark-based approaches [102, 169], this method only necessitates an ellipsoid shape model for establishing relative position with respect to the asteroid.

D.2 Absolute State Estimation

This section aims to briefly define absolute state estimation, explicitly focusing on the dynamics equations involved in the estimation process.

D.2.1 Translation Dynamics

The translational dynamics are described in the I-frame. The equations of motion are written as follows:

$$\dot{\mathbf{r}}_I^{IB} = \mathbf{v}_I^{IB} \tag{D.1}$$

$$\dot{\mathbf{v}}_I^{IB} = \mathbf{g}_I + \mathbf{a}_{ext} \tag{D.2}$$

where $\mathbf{r}$ is the position vector, $\mathbf{v}$ the velocity vector, $\mathbf{g}$ the gravity vector, and $\mathbf{a}_{ext}$ the external acceleration vector from sources other than gravity. The gravitational and external acceleration are detailed in the next sections.

Gravitational Acceleration

The 3D polyhedron models utilized for the primary and secondary bodies in this context are derived from modified representations of the asteroids Bennu and Itokawa, respectively, as documented in the references [111, 170]. These shape models were established during the OSIRIS-REx and Hayabusa-1 missions, as outlined in greater detail in Section 3.3. This choice is underpinned by the aspiration to create a simulated environment within the camera simulator, offering the significant advantage of assessing the efficacy of the developed algorithms against realistic shape models.

Furthermore, it is noteworthy that third-body perturbations have been deliberately disregarded in this analysis. This decision stems from the observation that, at altitudes below 5 km, the influence of these perturbations is neglectful when compared to the other prevailing accelerations, such as those resulting from SRP, control acceleration, and gravitational forces (as depicted in Figure C.3).

External Accelerations

The simulated external accelerations encompass both the influence of the SRP and the guidance acceleration. It's important to note that the SRP arising from the asteroids' albedo is omitted from consideration. Within this context, the constrained terminal velocity guidance algorithm computes the desired guidance acceleration, as in [171]. It's noteworthy that the dynamics of the propulsion system are not used into this calculation; consequently, the computed guidance acceleration is directly applied to a simplified point mass model of the spacecraft.

D.2.2 Attitude Dynamics

The spacecraft's attitude dynamics are not explicitly represented in the model. It is assumed that the spacecraft's pointing information is provided by the GNC subsystem, utilizing a traditional

gyro-stellar estimator. This model does not consider any inaccuracies in the pointing information. For a more comprehensive description of the asteroid system modeling, please refer to Section 3.3.

D.3 Sensors and Measurement Models

The spacecraft is equipped with various sensors that are essential for its operation. This section provides a more detailed description of the characteristics of these sensors and how they are modeled. It should be noted that the star trackers and gyroscopes will not be considered at this point. Instead, attention will be directed towards the remaining sensors, which include the accelerometer, LRF, and the camera.

D.3.1 Accelerometer

The accelerometers measure the acceleration of the lander. The accelerometers are assumed to be located on the lander CoM, aligned with the three axes of the B-frame. The accelerometer measurements $\tilde{\mathbf{a}}_B$ are modelled with white noise and velocity random walk:

$$\tilde{\mathbf{a}}_B = \mathbf{a}_B(t) + \mathbf{b}_a(t) + \boldsymbol{\eta}_a(t) \tag{D.3}$$

where $\mathbf{b}_a$ is the velocity random walk in B-frame modelled as:

$$\dot{\mathbf{b}}_a(t) = \boldsymbol{\eta}_{ba}(t) \tag{D.4}$$

$\boldsymbol{\eta}_a(t)$ and $\boldsymbol{\eta}_{ba}(t)$ are zero-mean white noise vectors with standard deviations presented in Table 3.7.

D.3.2 Camera

The navigation camera employs image processing techniques to precisely determine the position of the asteroid's centroid within the image. By leveraging this centroid's coordinates in conjunction with a camera model, a unit vector pointing towards the asteroid within the B-frame reference is derived. This procedure is thoughtfully presented in Figure D.1, wherein a point denoted as P on the asteroid is projected onto the camera's sensor, yielding the pixel coordinates, namely (u_P, v_P). Subsequently, a unit vector originating from P and expressed within the B-frame is computed employing the camera model. This resulting unit vector carries information about the asteroid's relative direction with respect to the lander, and it represents the measurement in the navigation filter.

Image Rendering

Table 4.1 shows the camera's specifications. A scene containing two asteroids has been rendered within the Planet and Asteroid Natural Scene Generation Utility (PANGU). The 3D models utilized for the asteroids are modified versions of Bennu and Itokawa, as elaborated in Section 3.3.1. The operation of *PANGU* takes place within the *MATLAB/Simulink* simulator. *PANGU* receives inputs consisting of the sun's position, the positions and orientations of the asteroids, and the spacecraft's

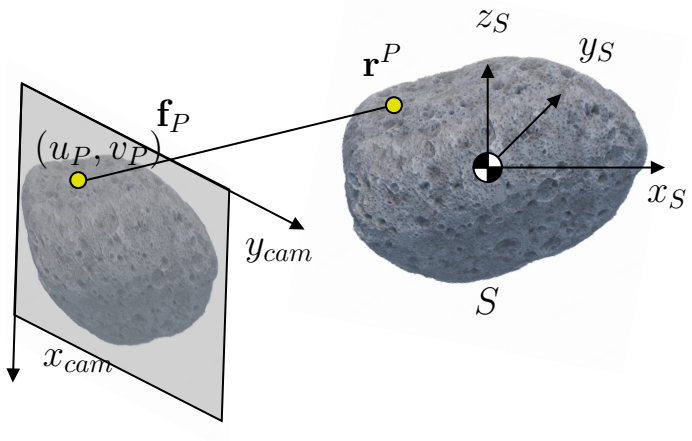

Figure D.1: Projection of a landmark P defined in S-frame onto the camera sensor frame as feature

position and orientation. Figure D.2a and Figure D.2b illustrate two sample images rendered in *PANGU*.

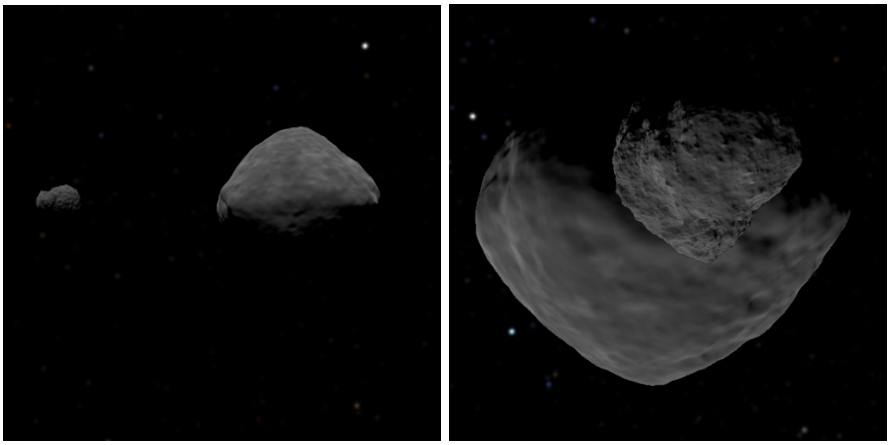

(a) Navigation camera output at 8500 m distance from the surface of the secondary

(b) Navigation camera output at 550 m distance from the surface of the secondary

Figure D.2: Navigation camera output.

D.3.3 Laser Range Finder

The LRF is aligned with the camera LOS direction, the Z-axis of B-frame, and provides a distance measurement to a point on the asteroid's surface. The distance $\tilde{r}_B^{Bj}$ measured by the LRF between the lander and a point j on the surface of the asteroid is sketched in Figure D.3 and is modelled as:

$$\tilde{r}_{LRF} = \tilde{r}_B^{Bj} = |\mathbf{r}_P^{Pj} - \mathbf{r}_P^{PB}| \tag{D.5}$$

The measurement is obtained using PANGU and uses the reshaped 3D models of Bennu and Itokawa. The measurement is obtained using the accurate distance from the sensor center to the 3D object hit point. If there is a pointing error, this is directly reflected in the measurement from PANGU.

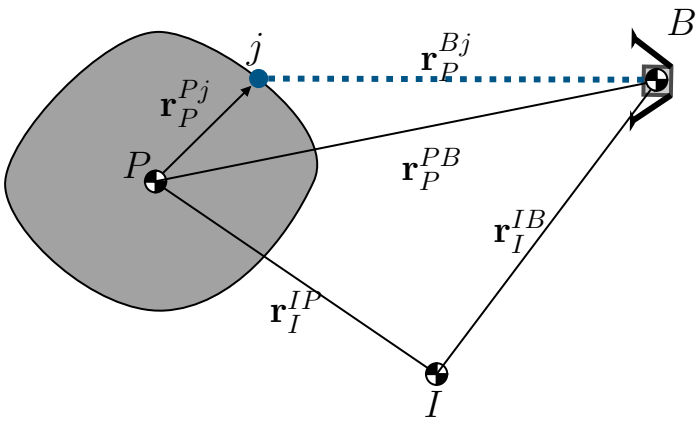

Figure D.3: Sketch of the LRF beam r_P^{Bj} intersecting the surface of asteroid P in the point j. Also shown is the position of P and B in the I-frame

D.4 Image Processing

The processing of camera images involves the extraction of centroid locations of asteroids in pixel coordinates. These centroids are subsequently employed as measurements within the navigation filter. The procedure for centroid extraction presents challenges owing to changing illumination conditions, overlapping asteroids, asteroids that may be partially outside the image, and irregular shapes. Additionally, the correct labeling of centroids as either *primary* or *secondary* is fundamental. In the current research, the following definitions are given:

1. Center of figure (CoF): the projection of the CoM of the asteroid onto the camera sensor, in pixel coordinates.
2. Center of brightness (CoB): the centroid of a region of pixels detected in the image, in pixel coordinates.

D.4.1 Centroid Extraction

The motion of the center of mass of asteroids is detailed in the SPICE kernels. Consequently, the preferred approach involves measuring the center of the figure, as it provides orientation towards a known point in inertial space. Nevertheless, this proves unattainable due to the variable lighting conditions causing shadows on the asteroid's surface and the irregular shapes of asteroids.

Figure D.4, the larger asteroid exhibits a shadowed region on its right side, leading to a displacement of the center of brightness location towards the left relative to the center of the figure. In order to address this disparity between the center of figure and center of brightness, the work by [103] introduces a corrective factor denoted as $\boldsymbol{\epsilon}_{cob}$. This factor compensates for the fluctuations in illumination conditions by shifting the center of brightness in the direction opposite to the sun's position within the camera frame. The definition of this correction factor, as well as the subsequent adjustments to obtain an estimation for the center of the figure [9]:

$$\boldsymbol{\epsilon}_{cob} = \arctan\left(\frac{8\pi R}{3r} sin\left(\frac{\phi}{2}\right)^2\right) \frac{\mathbf{u}_{det}}{h_{cam}} \tag{D.6}$$

$$\hat{\mathbf{p}}_{cob} = \boldsymbol{\epsilon}_{cob} + \mathbf{p}_{cob} \tag{D.7}$$

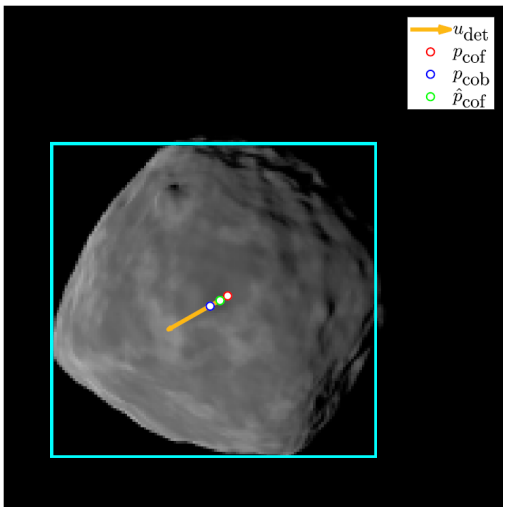

Figure D.4: Key concepts from the image processing. Note how p_{cob} is shifted in the direction opposite of u_{det} to obtain $\hat{\mathbf{p}}_{cof}$ [9]

The process of making correction can be seen in Figure D.4. However, it's worth noting a limitation with $\boldsymbol{\epsilon}_{cob}$: it assumes a spherical shape during its derivation. Consequently, when dealing with non-spherical asteroids, this correction may have limited effectiveness and could potentially even negatively impact the accuracy of estimating $\hat{\mathbf{p}}_{cof}$. As a result, this correction is exclusively implemented for the primary asteroid and not for the secondary one.

D.5 Reference Landing Trajectory

A reference landing scenario is being defined now that the EKF has been completed. The nominal flight time, in this case, is 4 hours, and the starting position is approximately 6770 m above the surface of the secondary asteroid. This initial position lies within the plane of rotation of the secondary asteroid around the primary. After the 4-hour duration, the spacecraft will have reached a target position approximately 300 m above the outward-facing pole of the secondary asteroid. Consequently, it can be inferred that at some point along the trajectory, the primary asteroid will come into view behind the secondary asteroid (as depicted in Figure C.5), prompting a simulation shutdown. The selection of the reference trajectory is based on ensuring this overlapping of the two celestial bodies in the image only occurs during the very final stages of the simulation, when the spacecraft is situated at an altitude of around 550 m above the surface. By default, the camera and LRF maintain their orientation towards the secondary asteroid at all times. The reference trajectory of the spacecraft, along with the movements of the asteroids and the direction of the sun, are illustrated in Figure D.5.

D.6 Results

The results obtained from my experiments and analyses, specifically concentrating on assessing the performance and sensitivity of the EKF setup across various scenarios, can be found in [9, 68]. The content delves into the filter's behavior during initial setup and tuning, its reaction to changes in the initial position, sensitivity to filter initialization errors, and its performance in the presence of image imperfections. The main findings are resumed in [9].

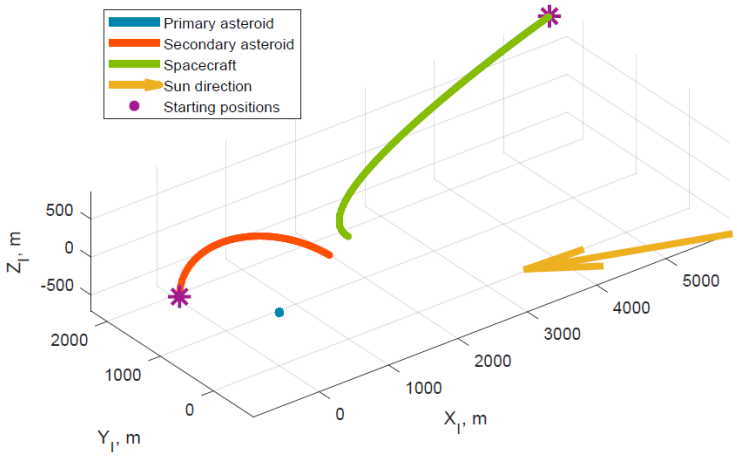

Figure D.5: Trajectory of the primary, secondary, and spacecraft in the reference landing scenario. Note that the illumination conditions are favorable due to the low sun phase angles

Acknowledgements

It is difficult to find the words to thank all the people who have been by my side these past years. These have been intense years, sometimes difficult, carefree, and busy with learning and growth; it is thanks to you who have been by my side that I have fully lived through them.

Thank you to Prof. Foerstner for guiding me these years and to Prof. Curti for being my mentor long before this project began, and for motivating me when needed.

Thank you to Matteo B. for believing in me from the beginning, and to Jens L. for introducing me to Lake Constance for the first time. Thank you to Frederik B. for the first grocery run during Covid, and for all the other more important things. Thank you to Maurice M. for the conversations about the future of space. Thank you to the whole Konstanz group and to Ciro and Benedetta, you were close to me when I needed it most. Thank you to Albert F. and Karl A., you taught me to work with balance and organization. Thank you to Stefan W. for his experience and always valuable advice. Thank you to Thomas O., Michael S., and Filippo A. for seeing my potential and giving me a new opportunity.

Thank you to Mario V. for the long discussions in the depths of our Science and for sharing part of this journey with me.

Thank you from the bottom of my heart to the Bad Ragaz, to Andrea and his Carbonara, to Gigi and his cold cuts, to Marco and his good humor, and to Luca and his bikes (even the ones he sold), thank you for the endless laughter.

This work is dedicated to my family and Giulia, who endures and enjoys with me.

Finally, Emanuela S. and Pietro S., you have been with me all this time when I was searching for meaning, thank you.

In closing, I extend my gratitude to each of you, not just for your roles in my academic pursuits, but for the support and memories of this *Bodensee* time.

Grazie.

Edoardo Caroselli, Rome, July 2024